USING SATURATED ABSORPTION SPECTROSCOPY ON ACETYLENE-FILLED HOLLOW-CORE FIBERS FOR ABSOLUTE FREQUENCY MEASUREMENTS

by

KEVIN KNABE

B.S., Kansas State University, 2003

AN ABSTRACT OF A DISSERTATION

submitted in partial fulfillment of the requirements for the degree

DOCTOR OF PHILOSOPHY

Department Of Physics
College of Arts & Sciences

KANSAS STATE UNIVERSITY
Manhattan, Kansas

2010

Abstract

Current portable near-infrared optical frequency references offer modest accuracy and instability compared to laboratory references. Low pressure reference cells are necessary to realize features narrower than the Doppler broadened overtone transitions, and most setups to date have occurred in free-space. Hollow-core photonic crystal fibers offer a potential alternative to free-space setups through their small cores (~10's of μm) and low-loss guidance. Furthermore, HC-PCF can be made into fiber cells that could be directly integrated into existing telecommunications networks. Efforts were made to fabricate these fiber cells with a low pressure of molecules trapped inside, but this has proven to be quite challenging. Therefore, investigation of these fibers is conducted by placing the ends of the fiber inside vacuum chambers loaded with acetylene ($^{12}C_2H_2$). The linewidths of several P branch $\nu_1 + \nu_3$ transitions (near 1.5 μm) are investigated as a function of acetylene pressure and optical pump power in three different HC-PCFs. Frequency modulation spectroscopy is then implemented on the acetylene-filled HC-PCF to generate sub-Doppler dispersion features that are useful for frequency stabilization using standard servo electronics. Instability and accuracy of this near-IR optical reference were then determined by analysis of heterodyne experiments conducted with frequency combs referenced to a GPS-disciplined rubidium oscillator. The instability and accuracy of this HC-PCF reference are within an order of magnitude of free-space experiments, as expected based on the ratio of linewidths observed in the two experiments. Therefore, HC-PCF has been shown to be suitable for potential frequency references. Further work is necessary to fabricate gas fiber cells with high optical transmission and low molecular contamination.

USING SATURATED ABSORPTION SPECTROSCOPY ON ACETYLENE-FILLED HOLLOW-CORE FIBERS FOR ABSOLUTE FREQUENCY MEASUREMENTS

by

KEVIN KNABE

B.S., Kansas State University, 2003

A DISSERTATION

submitted in partial fulfillment of the requirements for the degree

DOCTOR OF PHILOSOPHY

Department Of Physics
College of Arts & Sciences

KANSAS STATE UNIVERSITY
Manhattan, Kansas

2010

Approved by:

Major Professor
Dr. Kristan Corwin

Abstract

Current portable near-infrared optical frequency references offer modest accuracy and instability compared to laboratory references. Low pressure reference cells are necessary to realize features narrower than the Doppler broadened overtone transitions, and most setups to date have occurred in free-space. Hollow-core photonic crystal fibers offer a potential alternative to free-space setups through their small cores (~10's of μm) and low-loss guidance. Furthermore, HC-PCF can be made into fiber cells that could be directly integrated into existing telecommunications networks. Efforts were made to fabricate these fiber cells with a low pressure of molecules trapped inside, but this has proven to be quite challenging. Therefore, investigation of these fibers is conducted by placing the ends of the fiber inside vacuum chambers loaded with acetylene ($^{12}C_2H_2$). The linewidths of several P branch $\nu_1 + \nu_3$ transitions (near 1.5 μm) are investigated as a function of acetylene pressure and optical pump power in three different HC-PCFs. Frequency modulation spectroscopy is then implemented on the acetylene-filled HC-PCF to generate sub-Doppler dispersion features that are useful for frequency stabilization using standard servo electronics. Instability and accuracy of this near-IR optical reference were then determined by analysis of heterodyne experiments conducted with frequency combs referenced to a GPS-disciplined rubidium oscillator. The instability and accuracy of this HC-PCF reference are within an order of magnitude of free-space experiments, as expected based on the ratio of linewidths observed in the two experiments. Therefore, HC-PCF has been shown to be suitable for potential frequency references. Further work is necessary to fabricate gas fiber cells with high optical transmission and low molecular contamination.

Table of Contents

List of Figures

List of Tables

Acknowledgements

I would like to acknowledge the graduate students and post-docs in my research group as well as the technical staff at Kansas State University for their help with various experiments. Mike Wells was immensely helpful with the construction of vacuum chambers and general vacuum assembly. Rajesh Thapa taught me how to run the saturated absorption spectroscopy setup, and we coordinated together to make initial accuracy and stability measurements. Karl Tillman helped out extensively with the absolute frequency measurements, as well as with a considerable portion of the stability measurements. Shun Wu and Chenchen Wang were instrumental in the collection of the slow molecule linewidth reduction data in Chapter 4, and were very helpful with taking stability measurements presented in this work. Andrew Jones was very helpful with assembly of vacuum chambers and linewidth measurements in the kagome fiber while I was away visiting the University of Bath. Finally, I would like to thank Jinkang Lim for all of his hard work stabilizing the fiber frequency combs for the stability experiments.

I would also like to thank Dr. Fetah Benabid at the University of Bath (U.K.) for letting me use the facilities at his laboratory in the Centre for Photonics and Photonic Materials to work on creating low pressure gas-filled fiber cells. His group, consisting of Francois Couny, Philip Light, and Natalie Wheeler, were also extremely helpful in not only experimental procedure but ideas as well. Their combined research in the field of nonlinear experiments involving molecular gases in PCF made their laboratory the ideal place to conduct an important part of my research. This is in part due to the fact that the CPPM has a fiber drawing tower which allows them to fabricate PCF on site. PCF is typically on the order of hundreds of dollars per meter, but at this facility these costs are subsidized through grants and university funding. This allows for a practically infinite amount of fiber that is available for splicing and fiber cell production. Also, Dr. Benabid's acquisition of a polarization maintaining filament fusion splicer was vital for making angle splices.

This work was funded by the National Science Foundation and the Air Force Office of Scientific Research.

Dedication

This dissertation is dedicated to my parents, Otis and Cathy Knabe, as well as my grandparents, Paul and Izora Knabe and Fred and Betty Maricle. Without their support, none of my achievements in the academic world would have been possible.

I would also like to thank the long list of excellent teachers that I have encountered throughout my academic career. I apologize for any omissions, and hope that this can be forgiven.

In high school, Mrs. Vicki Glaser and Mr. John Kennedy provided me with both a love for mathematics as well as an excellent background this field of study.

In my undergraduate career, Dr. Andrew Rys, Dr. Bill Kuhn, Dr. Steve Warren, and Dr. Medhat Morcos were exemplary professors that imparted the basics of electrical engineering while increasing my thirst for knowledge. Dr. Andrew Bennett in mathematics was also one of the most energetic, intelligent, and personable professors that I have ever encountered.

Graduate school would not have been a reality for me without the excellent examples in teaching from Dr. Chris Sorensen, Dr. Amit Chakrabarti, Dr. Sanjay Rebello, and Dr. Larry Weaver. There is no question in my mind that I will perpetually benefit both in the classroom and the laboratory from the mentoring experienced under these individuals. Dr. Brett Esry and Dr. Uwe Thumm were also key to my graduate education (specifically quantum mechanics), as well as showing me how graduate courses should be taught.

Of course, I would be wrong to forget thanking my advisors, Dr. Kristan Corwin and Dr. Brian Washburn, for taking me into their group (as a refugee, no less). I was simply looking for a research position to finish graduate school so that I could eventually teach. What I got in return were mentors who taught me how to approach problems with confidence and the utmost ability.

CHAPTER 1 - Introduction to frequency references

Advances in precision measurements of fundamental quantities have had great effects on many aspects of society including commerce, transportation, and the transfer of information. Time is probably the most important fundamental quantity considering the number of applications that have depended on the precision and accuracy of its definition. One aspect of time that has significant importance to electronic and telecommunication systems is frequency (which is defined as the inverse of time). Due to both the speed and amount of information required to receive information over the internet, most signals today transmitted around the world are in the form of different frequencies of light. While great strides have been made with both optical clocks and frequency combs to increase the precision of measurements made in the frequency domain, these experiments are largely confined to the laboratory. The work of this thesis aims to increase the precision of frequency measurements away from the laboratory for practical purposes. Because optical fibers are used as transmission lines for these optical signals, investigation of several hollow core fibers is conducted in Chapter 2 to determine their suitability for portable frequency references. This is achieved by filling the fibers with low pressures (10^{-4} atm) of acetylene (the international molecular standard in this frequency region of the near infrared (IR)) and then performing a type of nonlinear spectroscopy to realize narrow absorption transitions. Chapter 3 then details a very convenient method called frequency modulation (FM) spectroscopy to stabilize a continuous wave (cw) laser to these absorption transitions. Characterization of this near-IR optical reference's frequency is then presented in Chapter 4 along with limitations imposed by the hollow-core fiber and efforts for further improvement. The work in these three chapters is done with the hollow-core fiber inserted in vacuum chambers to determine the optimal operating conditions of such a reference. This setup was driven by the fact that low pressure fiber cells (where solid core fibers are fused to both ends of the hollow-core fiber) are rather difficult to fabricate. Chapter 5 details efforts to make such a cell that would be ideal for the type of nonlinear experiments presented in Chapter 2 and 3. A summary of this work is included in Chapter 6, with references, publications, and appendices following after this.

Overview of how to characterize frequency references

A clock has two characteristics which determine how useful it is. The first is its ability to give the correct time after the clock has been started. The second is its repeatability to provide a "tick" of the same length in time. An example of these two quantities is as follows. If one were worried about attending an important meeting and did not want to be late, having a clock that could be counted on to give an absolute time would be critical while the individual "ticks" of the second hand could have large variations from one second to the next, and would not matter. Conversely, if one was making a repeated experimental measurement which depended on time, a clock that precisely "ticked" every second would be most useful and the absolute time would not matter much. Even if this clock's "ticks" were fast or slow, the data could be corrected once this clock was compared to a better one. A clock that is both accurate and precise would be ideal. However, clocks that are less than ideal with respect to their precision or accuracy can still be useful depending on the circumstances.

When considering optical clocks and references with accuracy and precision in mind, it is not possible to directly measure these quantities in the time domain. This is due to the fact that the frequency of optical light ($\sim 10^{14}$ Hz) is many orders faster than the detection capability of electronic detectors ($\sim 10^{10}$ Hz). Because of this fundamental limitation imposed by electronics, analysis of optical clocks is done in the frequency domain by means of heterodyne experiments. Heterodyne experiments involve two optical sources that are overlapped in space and time so that they interfere. This interference signal contains both the difference and the sum of the frequencies of the optical sources used, and the difference frequency product is generally in the RF and can be counted with standard electronics. This is directly analogous to tuning two musical instruments to the same audible frequency (on the order of 100's of Hz), and hearing a low frequency beat between the two (on the order of Hz).

Similar to the case above in the time domain, measuring the characteristics of a frequency reference requires access to a more accurate and stable reference. One choice for a frequency reference that is capable of being both highly stable and accurate is a frequency comb. A frequency comb is a mode-locked laser which has all of its modes of oscillation stabilized in the frequency domain. The spacing of the frequency comb's teeth is the repetition frequency (typically 100's of MHz), and is determined by the length of the laser cavity. Due to the stabilization technique employed for most combs (discussed in more detail in Chapter 4), broad

spectral coverage is achieved and effectively creates a large series of related optical references. , using a comb in a heterodyne experiment with an optical reference assures that the beat note between the two sources is always less than half the repetition rate. This frequency range is easy to detect and mix with standard electronic equipment that has been available for decades.

A brief history of timekeeping

The science of timekeeping involves accurately and precisely realizing the fundamental unit of time, the second. Time and length are fundamental quantities that are related by the definition of the speed of light. Up until the 20^{th} century, time has been defined using clocks (any device composed of a frequency oscillator and a counter) which depend on either celestial or mechanical oscillations. The oldest clocks use the rotation of the Earth to determine time, and include sun dials, Stonehenge, and the Mayan calendar. This method of timekeeping relies on direct sunlight, and therefore inclement weather renders this sort of clock useless. Clocks were later invented that use gravity and the displacement of a known mass (hourglasses or water clocks). These clocks had two main advantages over the solar clocks; they would work anytime, regardless of weather conditions or time of day, and their measurement periods were reduced by an order of magnitude (from days down to hours). These displacement clocks did suffer from a major drawback; they would only run for 1 cycle (allowing only a single measurement) before they would need to be "rewound" for another measurement, meaning that someone would have to monitor the clock. The next discovery in the history of clocks was Galileo's analysis of the pendulum, whose period was on the order of a second. This finally allowed for technology that could measure the time to within a minute over the course of a day without needing to be reset.

During this time period when pendulums were incorporated into existing clocks, maritime trade had become the main method of international commerce. Large sums of money were invested not only in the actual shipping boats, but into navies as well to protect these investments from pirates and other rival nations. Inaccuracies of timekeeping at sea lead to large miscalculations in position, increasingly the likelihood of getting lost at sea, running into land in bad weather, or wandering into pirated waters. Expeditions were set up by different nations to chart courses through dangerous territory, as the most significant financial losses were incurred by vessels that were lost at sea. Measuring one's latitude (the distance in the North-South direction from the equator) can be done by observing the angle the sun makes with the horizon

(90 degrees corresponds to the equator) and knowing the day of the year (many tables containing this information were made by astronomers). However, knowing one's longitude was impossible by this method. Using a clock and a compass to record the speed and direction of the ship was the only reliable method for charting one's course. Pendulum clocks have an additional drawback that limits their usefulness: external forces, pressure changes, and humidity changes caused the changes in the period of these clocks, essentially rendering them useless on rocking boats that often encounter devastating storms. Several academic minds of the day were convinced that observing the relative position of the moon to the stars was the most viable way to navigate at sea, despite the complexity necessary to calculate one's position from tables of star charts. The British government offered a large reward for a sea worthy clock, and John Harrison's chronometer was the answer to this dilemma after a lifetime of work [1, 2]. His invention stood as at the forefront of timekeeping for over 100 years. To this day military and economic enterprises fund experiments working towards better clocks with respect to accuracy and portability.

Albert Michelson, most famous for the first precise measurement of the speed of light and his key role in the creation of interferometry, made the remarkable speculation in 1892 that the green Hg emission line could be used (in conjunction with the speed of light) to define length [3]. This proposition of atomic systems as frequency references is quite remarkable in that it predates quantum theory, and could not be tested for at least another 70 years for a variety of technical reasons. However, advances in timekeeping were not stagnant during this time. The next advance in timekeeping came during World War I when crystal oscillators were used for sonar. These oscillators resonate at microwave frequencies ($\sim 10^7$ Hz) and allowed for major advances in communications due to both their high frequency and small size. These crystal oscillators, however, were found to degrade with time due to changes in their crystal structure.

The advent of the laser in the 1960's ushered in a new era for time-keeping. These coherent radiation sources allowed tests of Michelson's proposed atomic references. Atomic references have turned out to be the most precise clocks available due in part to their large oscillation frequency. The base unit of time, the second, is now defined as 9,192,631,770 periods of the cesium 133 hyperfine ground state radiation, and further advances will be based on more precise optical references. Frequency references' usefulness, however, is not limited solely

to timekeeping. Advances in telecommunications has made it necessary to search for better frequency references as the demand for larger amounts of bandwidth continually increases.

Telecommunication applications

The ability to communicate information over long distances has been a challenge throughout the ages. Setting fires in a sequence to serve as beacons dates back to ancient Greece, and were still in use up through the middle ages when the British used this communication system along the southern coast of England to warn London of the oncoming Spanish Armada [4]. Each beacon had to be attended by an operator, and only transmitted one piece of information. More sophisticated systems depending on visual signals were later developed in the 1800's, but relied on highly trained operators and were limited by atmospheric visibility. Also, these visual signals had no way of keeping messages private.

Modern telecommunication systems essentially started with the invention of the telegraph. Many individuals worked on developing this technology (including Carl Gauss among many others) as it became apparent that sending messages using electricity was much quicker and more secure than previous methods. In 1837, roughly 30 years from its inception, the telegraph was independently patented and implemented in both the U.K. by Sir William Fothergill Cooke and Charles Wheatstone and the U.S. by Samuel F. B. Morse and his assistant Alfred Vail. Over the next 20 years, the major metropolitan areas of the United States were connected by telegraph lines, and in 1866 the first successful transatlantic lines were implemented between Britain and the U.S. The world was essentially connected by 1872 when submarine cables were laid to connect Australia to Asia. Submarine lines were connected across the Pacific in 1902, completely circling the globe with high speed communication.

At this time when the world was first connected with near instantaneous communication, transmission of encoded telegraph information was limited to a single direction. Thomas Edison and Elisha Gray were paid by Western Union (the first major telecommunications company) in 1872 to find a way to send multiple signals simultaneously over a single line, and did so in about 2 years, with many improvements coming in the following decade. Another invention during this time period that would revolutionize communications was as telegraph that could transmit and receive audible tones, and was independently invented by both Alexander Graham Bell and Elisha Gray (among many others in years to come). Bell ultimately received the patent for the

first telephone, although this fact was disputed in courts for the next 20 years. Bell's laboratory notes and letters to his family ultimately provided evidence that his work had been independent, as well as admissions from other inventors of knowledge of Bell's scientific achievements. On a separate note, Bell initially offered to sell his patent to Western Union for the sum of $100,000. The head of Western Union laughed away this offer, as he considered nothing but a mere toy. In less than two years time, it is reported that Western Union sought to buy the technology for $25,000,000 but Bell was no longer willing to sell the patent. In the meantime, Bell created his own company, and matured the technology into being able to transmit voices (after buying Edison's patent on the microphone). Ultimately, the short-sightedness of Western Union became apparent, as over 150,000 individuals were using telephones by 1887.

Electronic theory and practical implementation matured throughout the early 20th century, resulting in advanced communication networks that improved both the speed and quantity of data that could be transferred between locations. One of the main advances that helped achieve these benefits was the advent of digital communications in the 1960's. Prior to this, signals were transmitted and received in an analog fashion, and long distance signals were very susceptible to degradation by means of noise. Digital signals alleviate this problem as they can replicate the original transmission through a series of properly implemented decoders and amplifiers.

Bell briefly experimented with light to encode voice transmissions with his invention of the photophone in 1880 [5]. This ingenious invention relied on using a speaker to vibrate a mirror which would reflect light towards a target with a similar setup to decode the signal. Due to the signal degradation experienced by changing atmospheric conditions, work on this technology would not continue for many years.

At the turn of the 20th century in what seemed to be an unrelated field, light waves were sent through bent glass rods as lamps for medical purposes [6]. This idea of sending light over small glass rods was later patented in the 1920's by John Logie Baird and Clarence W. Hansell for sending television signals and reproducing images. In 1930, a medical student named Heinrich Lamm was the first person to bundle together several small glass rods, or fibers, with the idea of imaging interior parts of the body without major surgery. The idea was to send light along some of the fibers and collect the image with the remaining fibers. For the purposes at the time, loss along these fibers was not an issue for the short distances required in the medical field.

The development of lasers in the 1960's offered a new source of coherent radiation that could, among other things, be used for communication purposes. There still remained the issue of transmitting this signal over significant distances, as the fibers that were available exhibited loss on the order of 1 dB/m (or 20% of the light was attenuated every meter). In 1965, Dr. Charles K. Cao and George A. Hockham proposed that impurities were degrading optical transmission in fibers, and losses of 10 to 20 dB per km (0.2% optical attenuation per meter) could be realized. Dr. Cao was later recognized for his excellent work in this field, and in 2009 was awarded the Nobel Prize in physics. In 1970 researchers for Corning Glass Works achieved this critical threshold for loss with titanium doped silica fibers, laying the experimental groundwork for today's standard telecommunication connections. Advances in optical fibers eventually produced losses that were well below that of electrical lines.

Following in Edison and Gray's footsteps to send multiple sets of information over a single transmission line, wavelength division multiplexing (WDM) was proposed in 1970 [7] and realized experimentally later that decade [8, 9]. This technique makes it possible to mix multiple colors of light, send them simultaneously over an optical fiber, and later extract the individual frequencies at the receiving end. Initial experiments were conducted with just a few different optical frequencies, but current systems allow for over 160 frequencies to be transmitted simultaneously [10]. This achievement is quite significant in the fact that large bandwidths of the optical spectrum have been utilized (10's of THz) as compared to the bandwidth of electronics in the RF domain (10's of GHz). Current telecomm channel spacing (equivalent to channel spacing on FM radios) is set at 100 GHz, and while this spacing could be reduced, portable optical references in this wavelength region would limit the channel spacing instead of the fundamental molecular resonance. The following section gives an overview of the current portable references as well as the best laboratory references to date to put the work of this thesis in perspective.

Current near-IR frequency references based on acetylene

Acetylene has a series of overtone transitions that conveniently occur in the 1500 – 1600 nm range and has been chosen as the international molecular standard [11]. These transitions are well spaced and have been studied extensively for both the carbon 12 and 13 variants. Portable optical references based on acetylene offer accuracies on the order of 100

MHz [12], while the optimal laboratory experiments boast accuracies near 1 kHz that are limited by the fundamental absorption transitions [13-15].

The highest accuracy measurements of acetylene overtone transitions use a type of nonlinear spectroscopy (called saturated absorption spectroscopy and described in detail in Chapter 2) to observe absorption linewidths below the Doppler broadened profile. One condition necessary to observe narrow sub-Doppler resonances of acetylene overtone transitions is low enough pressures so that intermolecular collisions do not considerably broaden the linewidth. This, however, imposes the necessity of long interaction lengths due to the weak strength of the overtone transitions and the low gas pressures. Therefore, the first observations of sub-Doppler features in acetylene used a power buildup cavity (PBC) absorption cell (which is essentially a high finesse Fabry-Perot cavity built around an enclosed molecular vapor) and is shown in Figure 1.1a [16, 17].

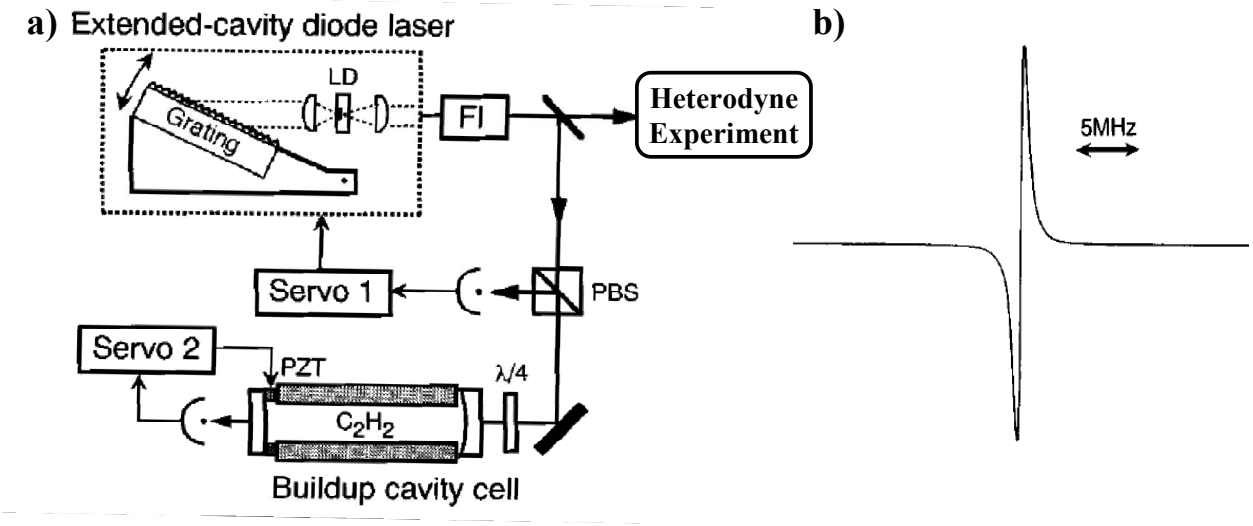

Figure 1.1 High-accuracy acetylene reference based on a PBC absorption cell with locking error signal taken from Ref. [17]. a) Schematic for frequency stabilization of a diode laser using frequency modulation spectroscopy and a PBC absorption cell. Listed are a Faraday optical isolator (FI) and a polarization beam splitter (PBS). b) Derivative of the sub-Doppler absorption feature created by frequency modulation spectroscopy, and used as the error signal to Servo 1 in a).

To achieve frequency stabilization, the diode laser was first locked to the Fabry-Perot cavity using frequency modulation spectroscopy (the theory of this technique is explained in detail in Chapter 3, while the experimental considerations for locking to an optical cavity are listed in Ref. [18]). A low frequency modulation was then applied to the cavity so that a

derivative of the absorption feature (shown in Figure 1.1b) could be observed and used to stabilize the cavity to the absorption transition. Once the diode laser was stabilized, a portion of the light was then sent to be heterodyned with an optical frequency comb. The particular type of comb used for this experiment was different in implementation than those listed in this work, and had detriments that limited the measurement accuracy to 100 kHz [19]. However, this setup has been repeated and improved upon by many groups that have achieved accuracies on the kHz level [13-15, 20, 21].

The current portable frequency standard in the near-IR is based on the work of Sarah Gilbert and Bill Swann [12], and uses a series of gas cells at various pressures to determine the linewidth broadening and line center shift of acetylene transitions as a function of pressure. An experimental schematic is shown in Figure 1.2a, and the Doppler broadened spectra used to calculate the shifts and broadening are included in Figure 1.2b. Their work, combined with a precise knowledge of the absorption transitions from previous work, has allowed the development of portable gas cells that can give accuracies on the order of 100 MHz. The accuracy of this system is limited by the fact that Doppler broadened absorption features with widths on the order of 1 GHz or greater are used to make these measurements.

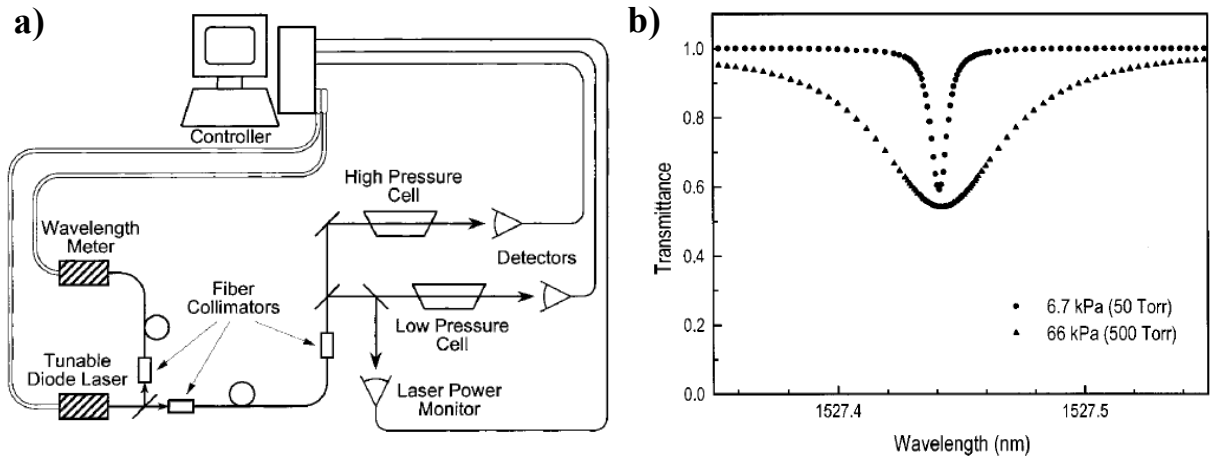

Figure 1.2 a) Pressure shift measurement apparatus. A tunable diode laser is passed through two gas cells as well as a wavelength meter while its frequency is swept to obtain absorption spectra versus wavelength, shown in b). For reference, a span of 0.02 nm at 1550 nm approximately equals a span of 2.6 GHz. Both a) and b) were taken from Ref. [12].

Another recent development in the realm of acetylene-based frequency references is the work at the Czech Metrology Institute which involves a 50 mW distributed feedback fiber laser,

a 50 cm gas cell, and a simple arrangement of polarization optics shown in Figure 1.3 [22]. The setup in this work is simpler than that of PBCs, and uses a nonlinear technique called polarization spectroscopy that is on the order of 10^3 times more sensitive [23] than saturated absorption spectroscopy. The significance of this work is that a cavity is not required, and yet stabilities and accuracies rivaling that of PBC setups are achieved. It is not difficult to imagine enclosing this setup in a rack-mountable box (with possibly a slightly shorter cell) so that this could be packaged as a portable unit.

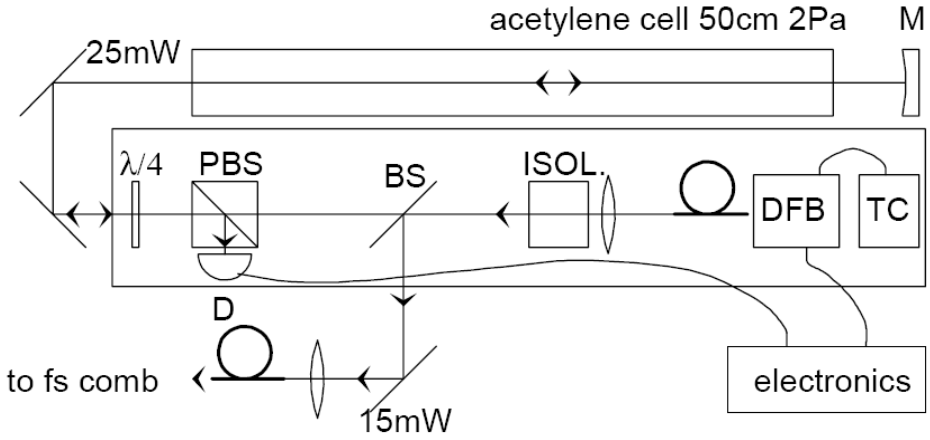

Figure 1.3 Polarization spectroscopy schematic taken from Ref. [22]. Listed are a mirror (M), polarization beam splitter (PBS), beam splitter (BS), optical isolator (ISOL.), distributed feedback laser (DFB), temperature controller (TC), and a femtosecond (fs) comb.

The work of this thesis aims to bridge this gap between the accuracy of current portable technology and the accuracy of ideal laboratory experiments by performing sub-Doppler spectroscopy techniques inside of hollow-core fiber than can be easily integrated into existing fiber telecommunication networks. Even though the aforementioned experiments could be made more compact and then packaged as portable references, problems could still arise with misalignment of free-space optics. A fiber-based version of a portable frequency reference would automatically alleviate this alignment issue by directly fusing the reference directly to the fiber network. This work has the potential to improve the accuracy of portable optical frequency references by a factor of 10^5, and limitations imposed by optical fiber are investigated.

An overview of hollow-core optical fiber

It has been described previously how the production of fused silica fiber allowed for optical communication networks to be widely implemented. Single mode fiber (SMF) has been one of the main fibers used in these networks due to optical transmission losses of 2×10^{-4} dB/m [24] and is shown in Figure 1.4a. This fiber experiences guidance by means of total internal reflection due to the core having a slightly higher index of refraction than the surrounding silica cladding.

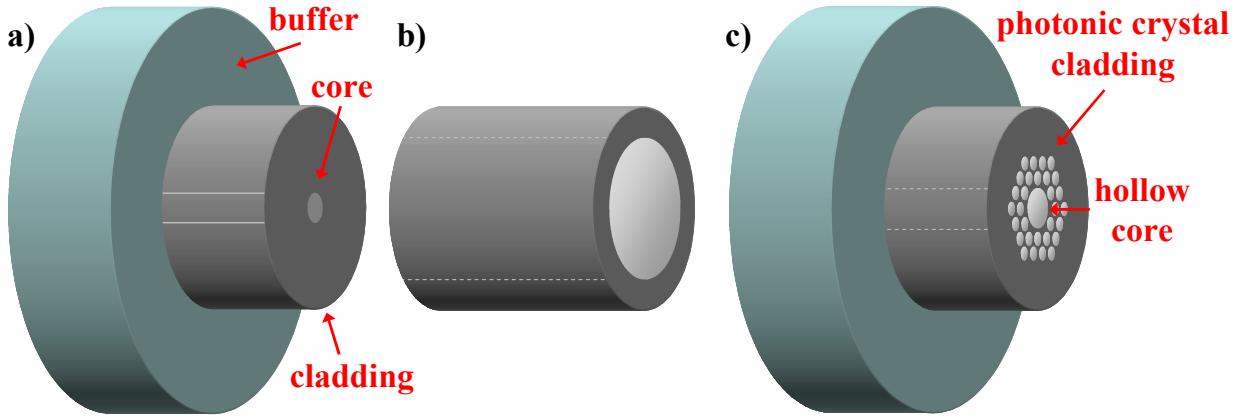

Figure 1.4 Cross-sections of a selection of fused silica fibers with cores indicated with solid and dashed lines for solid and hollow cores, respectively. a) SMF. The core (8 µm), shown with solid lines, is doped so that the refractive index is slightly higher than the surrounding cladding (125 µm), causing guidance through total internal reflection. A larger buffer coating (250 µm) exists to help protect the fiber from aging. Multimode fiber has the same structure, only with a larger core. b) Capillary fiber. Guidance occurs through simple reflection, and is therefore quite lossy. These fibers are made in a variety of sizes, typically on the order of 100's of µm. c) Hollow-core photonic crystal fiber (HC-PCF). Guidance occurs in the hollow core (10-20 µm) through interference effects of the photonic crystal cladding (also known as a two dimensional dielectric mirror). The core is actually a defect in the photonic crystal lattice, and is created by removing the inner unit cells prior to fabrication. A buffer coating is included similar to that of SMF.

However, to develop a fiber-based optical reference that depends on molecular absorption, a hollow core is necessary. One option is the capillary fiber shown in Figure 1.4b. Because the core has a considerably lower index than the surrounding fused silica, guidance occurs through reflections and is quite lossy. An ideal loss for such a fiber is ~5 dB/m for a 100 µm core at 1500 nm, and the loss goes as $1/r^3$ where r is the radius of the capillary [25]. This fiber must also be oriented in a fairly straight fashion, as small bends can greatly increase

the transmission loss. As such, long lengths of this hollow waveguide are not suitable for the basis of portable frequency references.

Hollow-core photonic crystal fibers (HC-PCFs) offer guidance similar to SMF (~10 dB/km loss [26]) and the ability to be filled with gas like capillary fibers. These commercially available fibers have a periodic array of air holes (or a two dimensional photonic crystal lattice) surrounding a hollow core (either 10 or 20 μm in diameter) that causes destructive interference of light in the cladding but not in the core (Figure 1.4c). These are in effect two dimensional dielectric mirrors (creating a "photonic bandgap" where certain colors of light are not allowed to propagate in the 2D crystal plane), where the hole size and spacing have been optimized to guide light at 1550 nm with a bandwidth of 200 nm (see Figure 1.5a and b). These photonic bandgap fibers' (PBGFs) excellent guidance allows for long interaction lengths with molecules, which in turn facilitates low pressure experiments. There is one significant detriment to these fibers, however. Coupling into modes that exist in the silica region immediately surrounding the core (called "surface modes") occurs due to a large spatial overlap with the core mode [27]. This coupling is observed as an oscillatory background in the transmission spectrum, and is observed in Chapter 2.

There is also a special class of HC-PCF called kagome fiber (which is named after the Japanese basket weaving pattern resembling the star of David) that offers broadband guidance with slightly higher loss than photonic bandgap fibers [28]. This fiber does at first appear similar to the aforementioned fibers in that it has a photonic crystal lattice (Figure 1.5c), but the air-filling fraction (the ratio of the area of the air holes to the total area) is much higher. Also, photonic bandgaps occur at approximately $\Lambda/2$, where Λ is the lattice spacing (or distance between hole centers). In the kagome fiber, photonic bandgap guidance should occur for wavelengths near 6 μm ($\Lambda_{kagome} = 12\,\mu\text{m}$). This is compared with PBGF whose lattice spacing is 3.8 μm and offers guidance at 1550 nm. However, these fibers do allow guidance outside of their bandgap region (there are transmission windows at 550 to 750 nm and 1050 to beyond 1700 nm) with losses around 1000 dB/km. This guidance is described in detail in Ref. [28], and is generally explained by the minimal spatial overlap the core modes have with the cladding modes. This isolation of the core modes, combined with the very small amount of glass in the cladding region, minimize the effects of surface modes. While this fiber has high loss that is comparable to that of the capillary fiber, its low bend loss makes it similar to photonic bandgap

fiber. The fiber lengths necessary for this experiment are on the order of meters, and make it so that kagome fiber is still a viable option for use in portable frequency references.

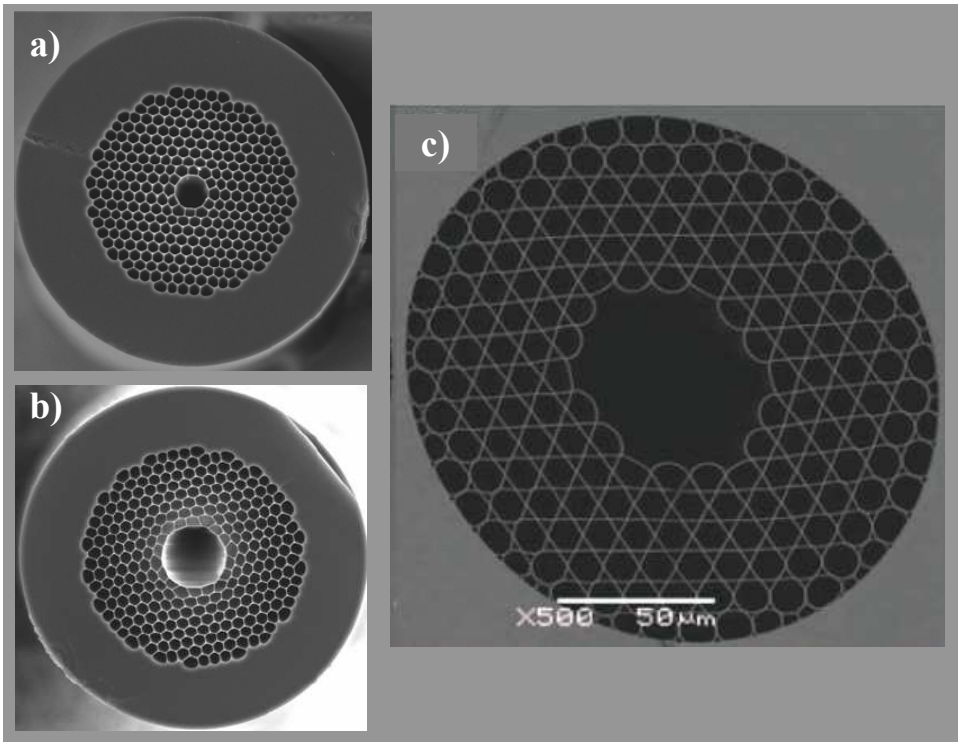

Figure 1.5 Cross-sections of different HC-PCF used in this work. All pictures have the same scale. a) 10 µm core and b) 20 µm core photonic bandgap fiber cross-sections taken from Ref. [26]. c) 70 µm kagome fiber cross-section taken from Ref. [28].

Due to these attributes of PBGF and kagome HC-PCF, they are the basis of the fiber-based portable frequency references presented in this work. The effects of both the advantages and disadvantages on the stability and accuracy of the fiber-based reference are investigated in the following chapters.

CHAPTER 2 - Saturated absorption spectroscopy inside hollow-core photonic crystal fiber

Using molecular absorption as a basis for laser frequency stabilization is appealing due to the narrow linewidths that can be observed experimentally. One such molecule that has an overtone absorption spectrum (described in Appendix A) in the near-infrared (IR) region is acetylene, and has been studied extensively [11-16, 20-22]. However, the natural linewidths of molecular transitions are not observable in acetylene due to the weak transition strengths as well as the presence of various broadening factors. The major source of broadening generally comes from the distribution of molecular velocities and their interaction with the laser field. When a molecule's velocity has some component along the propagation direction of the laser field, a Doppler frequency shift from the resonant frequency is observed. Other forms of broadening can also be present due to intermolecular collisions and high optical powers.

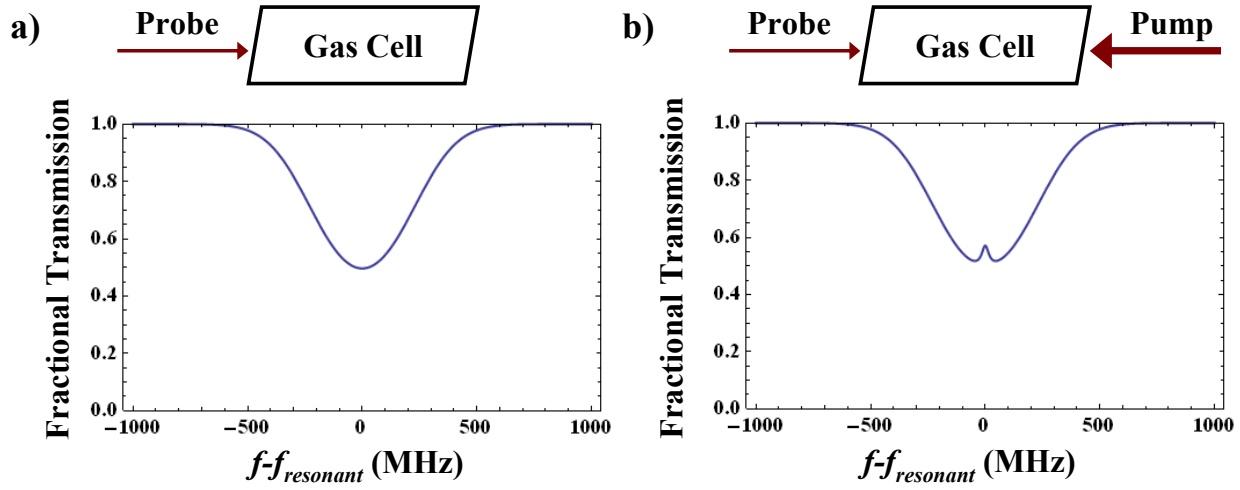

Figure 2.1 Fractional transmission of light through a gas cell versus frequency (a) when only a probe beam is present, and (b) when both a pump and probe beam are present.

To observe linewidths below the Doppler limit in molecular gases, nonlinear spectroscopy techniques are necessary. One such technique is saturated absorption (SA) spectroscopy, and was developed in the 1960's [29-33]. Additionally, many aspects of this research have since been considered to make this a very accurate form of spectroscopy [34-37]. SA spectroscopy uses a pump beam to excite molecules in a given velocity class and a probe

beam to then detect this absence of molecules in the ground state. Figure 2.1 shows the difference between the absorption spectrum in the absence and presence of a strong laser pump beam. If the pump and probe beams are created from the same laser source, then they must be antiparallel to each other to observe sub-Doppler absorption features. This is because it is necessary for both beams to interact with different molecular velocity classes except when both are on resonance. When the probe and pump beams interact with the same molecules, a reduction in the probe beam's absorption is observed. When the two beams are not interrogating the same molecules, then the probe signal is simply the unsaturated Doppler profile.

If long enough interaction lengths between the laser and the molecules are used, sufficiently low pressures can be used so that the linewidth is determined by the average time that molecules have to coherently interact with the laser field. Acetylene's overtone transitions near ~1530 nm have weak absorption coefficients. Therefore, in order to observe saturated absorption spectroscopy without considerable pressure broadening, interaction lengths on the order of one meter or greater are desirable. Free-space setups involving PBCs typically require a highly reflective cavity combined with a gas cell, and require precise alignment. In contrast, HC-PCF allows coupling of light into the air core, and provides low loss guidance over distances greater than several meters. However, collisions with the fiber core's inner glass walls limit the coherent molecular interaction time, and as a result broaden the observed sub-Doppler linewidth. These wall collisions are the largest source of sub-Doppler broadening in fiber spectroscopy, as low internal fiber pressures can be used in combination with long fiber length.

Investigation of HC-PCF's potential usefulness for SA spectroscopy is conducted by characterization of the sub-Doppler signals as a function of both internal fiber pressure and optical pump power. This is done with the the ends of the HC-PCF inserted in vacuum chambers, as sealed, low pressure fiber cells are difficult to fabricate, and are discussed in more detail in Chapter 5. The ends of the fiber are therefore loaded into vacuum chambers (whose volume are much greater than the volume of the fibers' core and surrounding air holes) and evacuated down to ~20 mtorr with a roughing pump (Figure 2.2). The vacuum chambers are then filled with the desired pressure of acetylene. Wedge-cut windows with infrared anti-reflective coatings (purchased from CVI Melles Griot) were used on one side of the vacuum chambers so that light could be coupled into the fiber ends from free space while minimizing reflections.

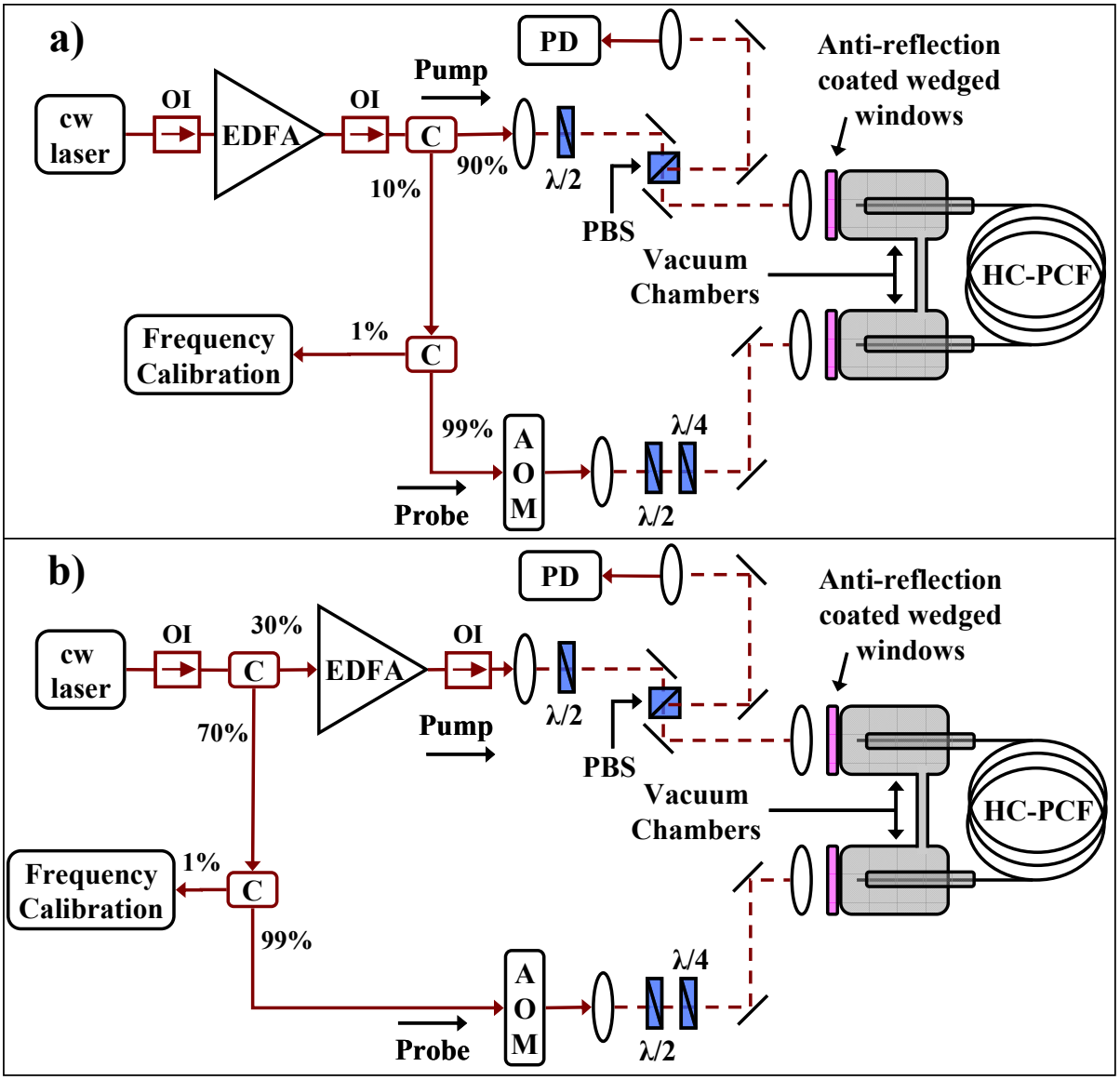

Figure 2.2 Optical layout for saturated absorption spectroscopy inside HC-PCF. The ends of the HC-PCF reside within vacuum chambers so that acetylene can be loaded into the evacuated fibers. Schematic a) splits the output of the erbium doped fiber amplifier (EDFA) to create both the pump and the probe at a fixed ratio to one another. Schematic b) splits the probe beam before the pump beam is amplified, thereby fixing the probe power, which allows for maximizing signal-to-noise ratio when shot noise limited, and fixes the amount of power broadening caused by the probe beam. This second schematic also has the advantage of independently applying modulations to either the pump or probe. Acousto-optical modulator (AOM), electro-optical modulator (EOM), coupler (C), polarizing beam splitter (PBS), optical isolator (OI), and photodetector (PD).

Two different cw laser sources were available for this experiment: an external cavity diode laser (ECDL) that could be tuned from 1505 nm – 1585 nm (or 10 THz around 195 THz), and a narrow linewidth (~500 Hz at 100 ms) fiber laser that could be scanned 10 GHz around the

P(13) $\nu_1 + \nu_3$ transition of $^{12}C_2H_2$ (both are described in more detail in Appendix B). An erbium doped fiber amplifier (EDFA) was then necessary to amplify the cw source laser up to 300 mW to achieve the appropriate pump powers for this experiment. This setup is depicted schematically in Figure 2.2a, where both the pump and probe beams are created from the output of the EDFA (Figure 2.2b illustrates an alternate setup that is more convenient to modify for experiments in Chapters 3 and 4). The probe beam, which is set at a fixed fraction of the pump power, is sent through an acousto-optic modulator (AOM) to shift the probe frequency. This causes the interference between the probe beam and any pump beam reflections to occur at one half the AOM frequency (f_{AOM} ~55 MHz), which can be easily filtered out electronically. The pump and probe beams are coupled into opposite ends of the HC-PCF to achieve the counter-propagating geometry necessary for SA spectroscopy using a single laser source. Polarization optics are used to separate the probe and pump beams by making the probe beam's polarization orthogonal to the pump beam's polarization at the polarizing beam splitter (PBS) after exiting the kagome fiber. The probe beam is then coupled back into a single-mode fiber and sent to a photodetector (PD) that is used to record the probe transmission. Applying a ramp voltage to the fiber laser's piezo-electric transducer (PZT) linearly scans the laser frequency, and an example of the resulting absorption spectrum is shown in Figure 2.3.

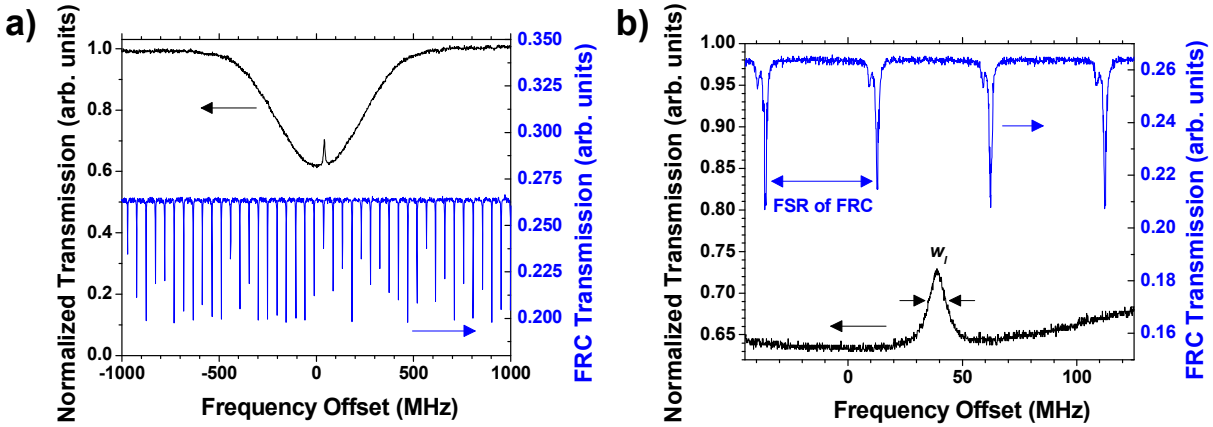

Figure 2.3 Saturated absorption spectrum vs. frequency with interferometer frequency calibration. a) (left axis) Normalized fractional transmission of a 4.1 m long HC-PCF near the P(13) transition for a pump laser power of 32 mW exiting the fiber, while the laser frequency was scanned at 1.2 GHz/sec. (right axis) The output from the FRC with a FSR of 48.01 ± 0.01 MHz. The contrast of the fringe depth is not 100% due to connector loss [38]. b) Zoom in of the sub-Doppler feature from a).

Frequency calibration

To properly characterize the linewidths of these absorption transitions, fitting of these spectra is necessary. For both types of cw lasers used in this experiment, however, applying a linear voltage to their scanning mechanisms does not translate into a linear frequency sweep. This is due to the hysteresis present in PZTs' motion when sufficiently large voltages are applied. It is generally necessary to apply these large voltages so that the entire Doppler profile can be observed (as seen in Figure 2.3a). Also, the manufacturers' specifications for the conversion between applied voltage and relative frequency change were not very accurate. Therefore, interferometers were setup so that a portion of the scanned laser light could be sent through them so that this signal and the absorption signal could be recorded simultaneously.

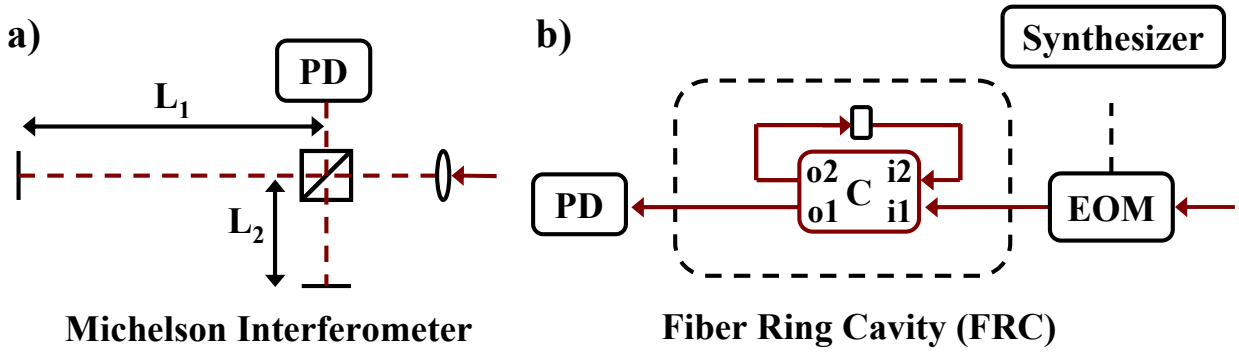

Figure 2.4 Interferometer schematics for laser frequency calibration. (a) Michelson interferometer schematic. The length of one arm (L_1) is larger than the other (L_2), and defines the free spectral range according to Equation 2.1. (b) Fiber ring cavity schematic. A standard 4-port fiber coupler (C) is used, where the input ports (i1 and i2) and output ports (o1 and o2) are labeled. For this setup, o2 should always be the lower coupling percentage of the two output ports, o2 and i2 are connected to make the the second pathway to the detector (and resembles a ring). In this case, o2 has a coupling value of 30%, while o1 has a complementary value of 70%. The output port of the cavity (o1) is then directed onto a large area photodetector, and can be seen in Figure 2.3 as the blue trace. If an EOM is used before the input of the cavity, then the cavity's free spectral range can be measured by changing the synthesizer's frequency so that the subsequent frequency sidebands are resonant with adjacent cavity resonances.

Two types of interferometers were used for frequency calibration and are shown in Figure 2.4. A Michelson interferometer was set up to have two different arm lengths, thus creating an interference signal on the photodetector whose free spectral range (FSR) is given by

$$FSR = \frac{c/n_{air}}{\Delta L} \qquad 2.1$$

where ΔL is the difference in path length, and for this case is $2(L_1 - L_2)$. While this system was robust, it does not lend itself readily to a portable setup. A fiber ring cavity (FRC) was also constructed to make a frequency calibrator that could be setup with standard fiber components [38]. A FRC is simply a 4 port fiber splitter where the secondary input (i2) and output (o2) port have been connected together. The primary output port (here defined as o1, and is the output port that has the higher coupling value) is connected to a photodetector, and thereby two paths have been created between the source and the photodetector. Light in both of these paths interferes, and for this case $\Delta L = L_{loop}$, where L_{loop} is the length of the connected input and output port. Common SMF optical patch cords can also be inserted in between o2 and i2 to easily change the FSR. Lengths can be practically measured down to the nearest cm, and therefore this calibration method offers accuracy on the order of 1% or better.

A higher-precision calibration method exists for the FRC where an electro-optic modulator (EOM) is used to place frequency sidebands on the light entering the FRC (EOMs are discussed in more detail in Chapter 3). The spacing between the sidebands and the central frequency is set by the drive voltage applied to the EOM. The frequency of the drive signal can then be changed so that the sidebands are resonant with the adjacent cavity modes. This can actually be extended up to any integer of the FSR, and gives accuracy on the order of 0.02% while requiring no knowledge of any lengths, refractive indices, or the speed of light.

Linewidth characterization results

Ultimately, the goal of investigating saturated absorption signals in HC-PCF was to find the narrowest linewidths with the strongest amplitudes. These strong, narrow signals will be the basis for cw laser frequency stabilization for use as a near-IR optical reference. Spectra have been recorded and analyzed at a variety of pressures and optical pump powers in HC-PCF with various core sizes to investigate these parameters. The first two types of HC-PCF used in this experiment were commercially available 10 and 20 μm PBGF [26], while the third type was 70 μm diameter kagome fiber obtained from our collaborators at the University of Bath (U.K.) [28].

These fibers have their advantages and disadvantages as described in Chapter 1, and are investigated in this section.

Fitting saturated absorption spectra in acetylene requires use of Beer's law [23], which is

$$FT = e^{-\alpha L} \tag{2.2}$$

where FT is the fractional transmission (or the ratio of the transmitted to the incident intensity), α is the absorption coefficient, and L is the interaction length between the molecules and the laser field. The absorption coefficient depends on both the number of molecules (N) and their cross-section (σ) and is given by

$$\alpha = \sigma N \tag{2.3}$$

Using the ideal gas law ($PV = NkT$), one can see that pressure (P) and N are linear if the volume (V) and temperature (T) are held constant. Due to the weak oscillator strengths of the $\nu_1 + \nu_3$ branch of IR transitions for acetylene, the absorption will have a Gaussian profile. The saturated absorption spectroscopy implementation allows observation of a narrow Lorentzian reduction in absorption when the pump and probe beams are resonant with the same molecular velocity class. The fitting equation used for the spectra recorded in this work was

$$\alpha L = -\ln(FT) = A_g e^{-2\left(\frac{f - f_{C_2H_2}}{w_g}\right)^2} \cdot \left(1 - A_l \frac{w_l^2}{4\left(f - f_{C_2H_2} - \frac{1}{2} f_{\text{AOM}} \right)^2 + w_l^2} \right) \tag{2.4}$$

where A_g is the amplitude of the unitless absorbance evaluated at resonance ($(\alpha L)_{\max} = -\ln(FT)\big|_{f = f_{C_2H_2}}$), w_g is the full width at $\frac{1}{e^{1/2}}$ (or 60%) of the Gaussian component, A_l is the amplitude of the Lorentzian component, w_l is the full width at half maximum (FWHM) for the Lorentzian component, $f_{C_2H_2}$ is the optical frequency of the acetylene transition of

interest, and f_{AOM} is the RF frequency of the AOM. The factor of ½ occurs in front of f_{AOM} for the following reason. The pump and probe beams are coupled into the HC-PCF in counter-propagating directions, so that the Doppler shift that the molecules experience are of opposite signs for the two beams. The equation for a molecule's Doppler shifted absorption frequency is

$$f_{abs} = f_{C_2H_2} + \vec{k} \cdot \vec{v} \tag{2.5}$$

Now, because the the pump and probe beams are created from the same laser source, their frequencies are related by

$$f_{probe} = f_{pump} - f_{AOM} \tag{2.6}$$

and the resulting wave numbers are given by

$$k_{pump} = \frac{2\pi f_{pump}}{c} \tag{2.7}$$

$$k_{probe} = \frac{2\pi \left(f_{pump} + f_{AOM} \right)}{c}. \tag{2.8}$$

However, due to the counter-propagating directions of the pump and probe, the unit vectors have opposite signs

$$\hat{k}_{probe} = -\hat{k}_{pump} \tag{2.9}$$

The condition of observing the narrow sub-Doppler feature in saturated absorption spectroscopy is that both the pump and probe are properly Doppler shifted to interact with the same set of molecules. This creates the following condition where

$$f_{C_2H_2} + \vec{k}_{probe} \cdot \vec{v} = f_{C_2H_2} + \vec{k}_{pump} \cdot \vec{v} \tag{2.10}$$

which simplifies to the following once Equations 2.7 - 2.9 are substituted in

$$f_{pump} = f_{probe} = \frac{1}{2} f_{AOM} \tag{2.11}$$

Similarly, the observed linewidth is reduced by a factor of two in this setup when compared to a setup that has a pump beam that does change frequency (which would necessarily need to be created from a separate source than the probe.

Figure 2.5a and b show the FWHM of the sub-Doppler feature, w_l, versus acetylene pressure inside the fiber and versus optical pump power exiting the fiber. In Figure 2.5a, the spectra in the various HC-PCFs all exhibit ~10 MHz/torr pressure broadening, in agreement with previous experiments at higher pressure [12]. A more notable trend, however, is the inverse relationship of the FWHM to the fiber's core size. This can be explained by transit-time broadening which is the minimum observable linewidth due to the limited interaction time between molecules and finite-sized beams. In free-space setups, the optical beam size can be adjusted by the appropriate choice of optics and narrow absorption features can be observed. Hollow optical waveguides used in this work have a set optical beam size, and this transit-time effect is ultimately the dominant source of broadening in the system at low pressures and low pump powers. The FWHM of the transit-time limited feature, $w_{l,tt}$, can be estimated by

$$w_{l,tt} = 0.375 \frac{v_{thermal}}{r_{1/e}} \tag{2.12}$$

where $r_{1/e}$ is the 1/e half width mode field radius of the optical beam and $v_{thermal}$ is the average thermal velocity for the molecules and is given by

$$v_{thermal} = \sqrt{\frac{2kT}{m}}. \tag{2.13}$$

This results in estimated widths of 46, 27, and 7.3 MHz for the 10 μm PBGF, 20 μm PBGF, and the large core kagome HC-PCF, respectively. For the kagome HC-PCF, there is no data for the

mode-field diameter, and since the core has an oval structure, the minor radius of 48 μm was used. There is good agreement with the zero-pressure intercepts of the experimental data in the three different fibers with widths of 36 MHz, 19 MHz, and 8.0 MHz, respectively (Figure 2.5a).

Linewidth broadening due to optical pump power was also investigated, and is shown in Figure 2.5b. According to Chapter 7 of Ref. [23], the power broadening experienced in a saturated absorption system where a single laser is used and the probe is much weaker than the pump,

$$w_l = \frac{w_{l,0}}{2}\left(1+\sqrt{1+\frac{P}{P_{sat}}}\right) \qquad 2.14$$

where $w_{l,0}$ is the linewidth in the absence of power broadening effects and P_{sat} is the optical power required to reduce the population-density difference (between the ground and excited state) to one half its unsaturated level. Linewidths in 20 μm PBGF (blue diamonds in Figure 2.5b) were fit using Equation 2.14, and values of $w_{l,0} = 27\,\text{MHz}$ and $P_{sat} = 49\,\text{mW}$ were obtained. Results were also obtained for data recorded in the kagome HC-PCF (green hexagons) with values of $w_{l,0} = 7.3\,\text{MHz}$ and $P_{sat} = 34\,\text{mW}$. These calculations neglect loss down the length of the fiber, and therefore are most likely overestimates. These values can be compared with the value of 23 mW reported in Ref. [39], where the reduction in observed absorption was used to calculate the saturation power.

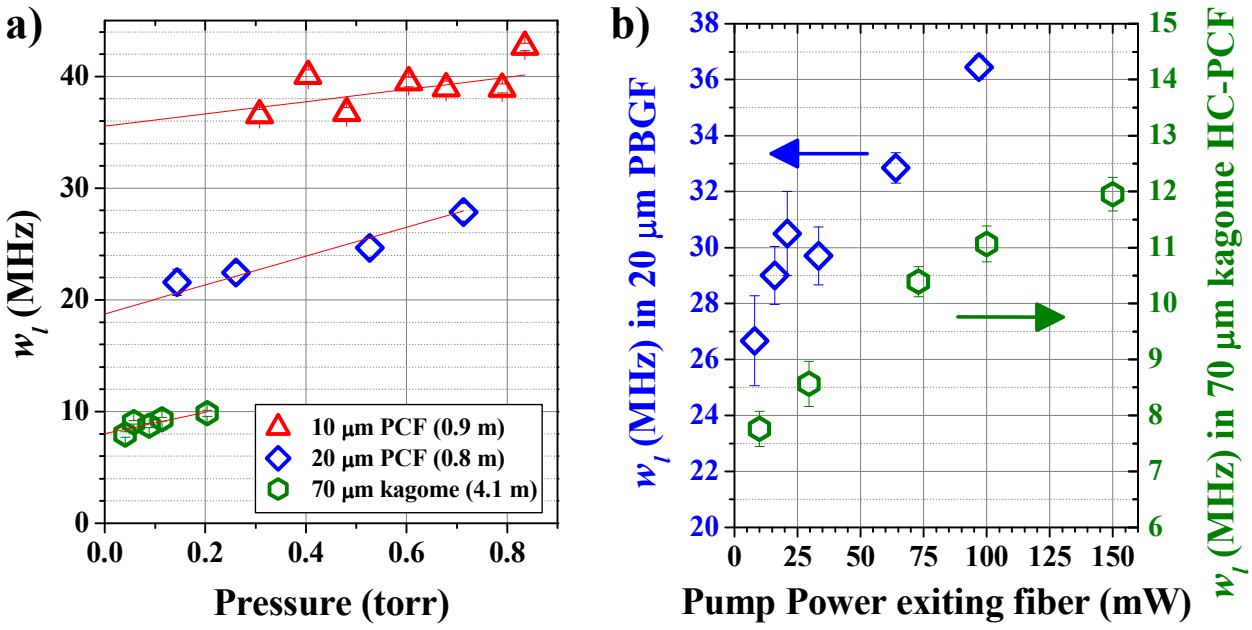

Figure 2.5 Sub-Doppler FWHM w_l as a function of acetylene pressure and optical pump power. a) w_l versus acetylene pressure with fit lines extrapolated to zero pressure for three different HC-PCFs. Data taken in the 10 µm (triangles) and 20 µm (diamonds) HC-PCF were taken on the P(11) transition [40], while data in the 70 µm kagome HC-PCF (hexagons) was taken on the P(13) transition [41]. The lengths of each fiber were 0.9 m, 0.8 m, and 4.1 m and the optical pump powers exiting the fibers were 30 mW, 29 mW, and 32 mW for the 10 µm, 20 µm, and 70 µm core fibers, respectively. Error bars from a chi-squared fitting routine are smaller than the symbol size. b) w_l versus optical pump power exiting the 20 µm PBGF (blue diamonds, left axis) and 70 µm kagome HC-PCF (green hexagons, right axis). For the 20 µm PBGF, the fiber length was 0.8 m and the pressure was 1 torr, corresponding to a FT = 25%. The kagome fiber's length was 1.4 m, and the pressure inside the fiber was near 200 mtorr, corresponding to 60% FT.

Although the kagome fiber exhibits the narrowest sub-Doppler features in HC-PCF to date, the inherent fiber loss makes it difficult to make a direct comparison with PBGF. There is less than a few percent power loss in PBGF over the course of a couple of meters, while kagome HC-PCF can easily lose 20% of the guided light every meter. This means that data recorded in kagome fiber exhibits more power broadening than data recorded in PBGF when the power exiting both fibers are equal. However, the kagome fiber does offer an advantage over PBGF in that there are no observable surface modes (see Chapter 1 for a detailed explanation of surface modes). Even though PBGF offers excellent low-loss guidance in the core, surface modes in these fibers cause an oscillatory background (shown in Figure 2.6) which can lead to shifts in the position of the sub-Doppler absorption feature's peak. When stabilizing a laser to a signal such

as this, this shift in peak position will directly translate into a frequency offset, and will degrade the performance of the reference. PBGF can be designed to reduce this effect [42], though most of the fiber that is commercially available has not corrected for this flaw. Kagome fiber on the other hand does not exhibit surface modes because of the reduced amount of silica present in the cladding area (see Figure 1.5 for a comparison between PBGF and kagome HC-PCF cross-sections), and is potentially more suitable for accurate frequency measurements.

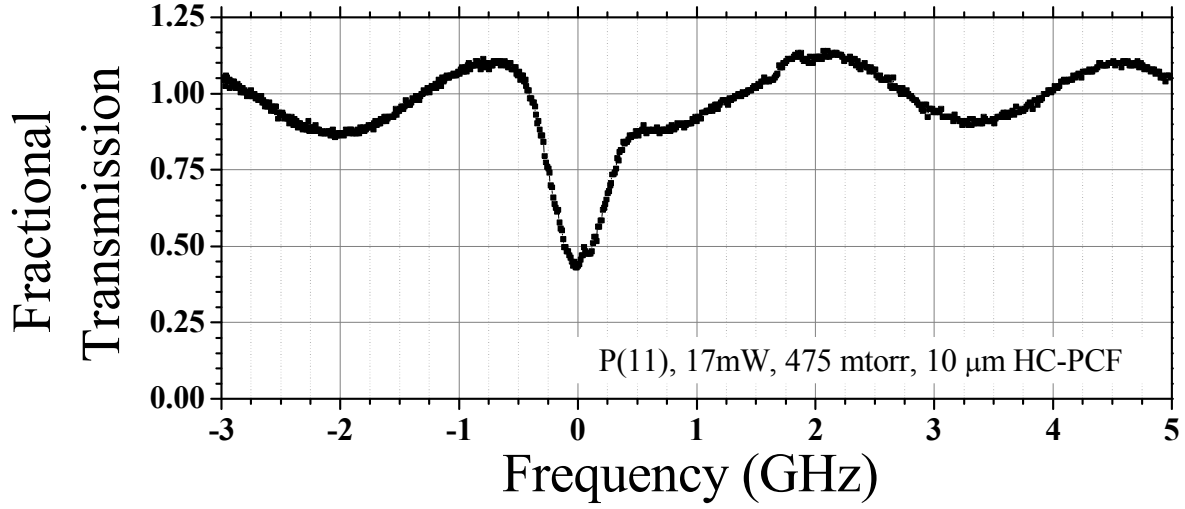

Figure 2.6 Fractional transmission saturated absorption signal in acetylene-filled 10 μm PBGF vs. frequency. The oscillatory background in this fiber is due to inherent coupling between the hollow-core mode and "surface modes" in the silica cladding. The $\nu_1 + \nu_3$ line, optical pump power exiting the fiber, and internal fiber pressure are listed at the bottom of the graph.

When determining suitability for optical references inside of fibers, the width of the absorption feature is not the only parameter that needs consideration. Frequency modulation spectroscopy, which is discussed in Chapter 3, is used to generate a derivative of the sub-Doppler feature that is useful for frequency stabilization. It is the slope of this derivative that will determine how well we can lock a laser's frequency to an absorption feature (the larger the slope, the better). We define a term called the discrimination (D) to estimate this ability, and is defined as

$$D = \frac{C}{w_l^2} \qquad 2.15$$

where C is the contrast of the sub-Doppler feature (or the amplitude of the sub-Doppler feature in fractional transmission units) and is defined here as

$$C = e^{-A_g(1-A_l)} - e^{-A_g}. \qquad 2.16$$

The parameter C is similar to the quantity described in Ref. [16] (whis is defined as the ratio of the height of the sub-Doppler feature to the height of Doppler broadened transition, and does not give a good indication of the signal-to-noise ratio). A plot of D versus pressure inside each of the fibers is included in Figure 2.7 and shows that kagome fiber offers D values on the order of 1,000 GHz^{-2}, which is a factor 10 improvement over PBGF. Free-space experiments that use high finesse cavities can still do much better than this, and from the work in Ref. [20], this experiment would offer D's near 20,000 GHz^{-2} ($C \sim 0.02$ and $w_l = 1$ MHz).

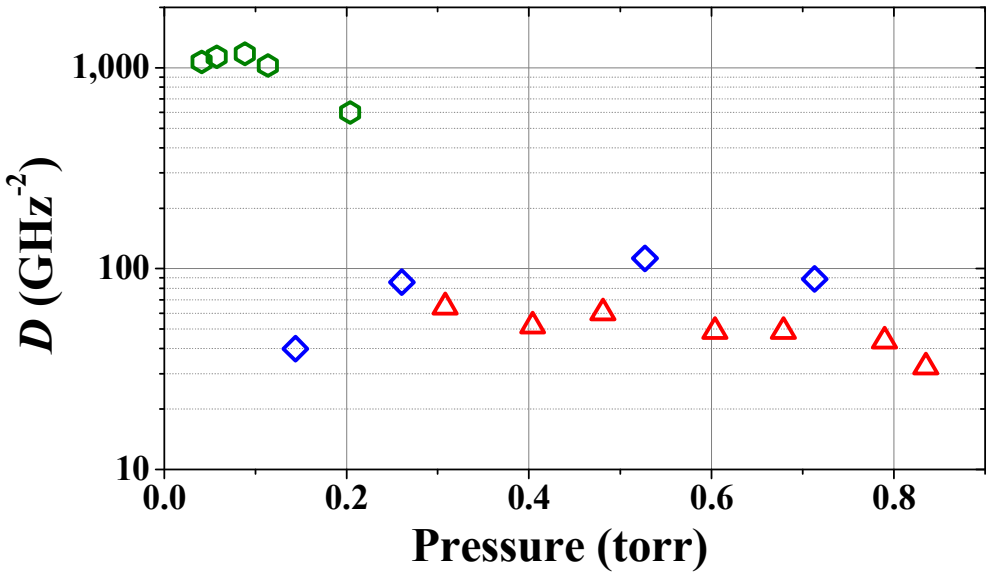

Figure 2.7 Discrimination (or Contrast/ w_l^2) versus pressure in 10 µm PBGF, 20 µm PBGF, and the large core kagome HC-PCF. These values were calculated from the results of Figure 2.5a. Optimal values of D can be observed in the middle of each data set, which roughly corresponds to 50% FT.

The discrimination was also calculated for the data taken versus power in Figure 2.5b. The results show that at low powers, D increases steadily (Figure 2.8). However, between 50 and 100 mW, the discrimination levels off. This indicates that the increasing amplitude of the

sub-Doppler feature at high optical powers is cancelled by the power broadening observed in the width.

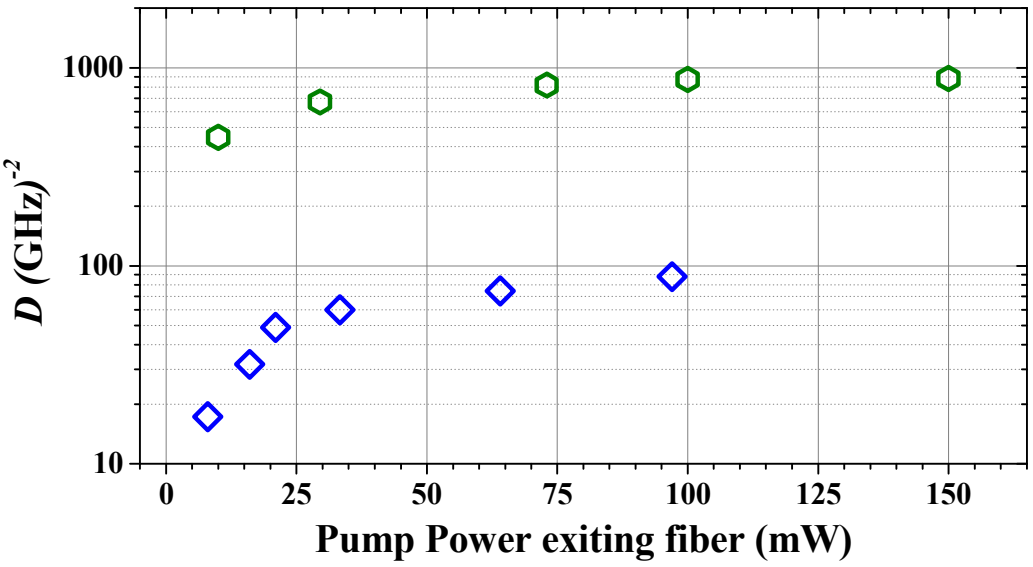

Figure 2.8 Discrimination (*D*) versus pump power in the 20 µm PBGF and the large core kagome HC-PCF from Figure 2.5b. The value of *D* increases with power up to a point, which appears to be near 100 mW.

In summary, the sub-Doppler linewidth has been investigated as a function of fiber pressure and optical pump power (where the measured linewidths in kagome HC-PCF are the narrowest in fiber to date). Also, the optimal conditions for laser frequency stabilization have been estimated. Working at a pressure that makes the FT equal to 50% and an optical power over 100 mW should give the strongest observable Lorentzian features, although small amounts of pressure and power broadening may be present. The optimization of the linewidth will be useful for the aim of this work. However, absorption features are not directly suitable for laser frequency stabilization due to their even symmetry (any deviations from the peak of the transition do not indicate whether an increase or decrease in frequency has occurred). While there are many types of modulation techniques available to generate absorption derivative signals (that have the necessary odd symmetry), one convenient and well-studied method is frequency modulation spectroscopy. This is the modulation scheme used throughout the rest of this work, and is described in detail in Chapter 3.

CHAPTER 3 - Frequency Modulation Spectroscopy

Frequency modulation (FM) spectroscopy is a technique capable of detecting absorption and dispersion features [36, 43] which are convenient to use to stabilize laser frequencies to either molecular transitions or cavity resonances. Originally invented for use in microwave spectroscopy experiments [44, 45], FM spectroscopy was later implemented in laser spectroscopy through the use of phase modulators (more commonly known as EOMs). This method generates signals that have zero-crossings that are suitable for laser stabilization, and is insensitive to laser intensity fluctuations to first order. This technique also has the advantage of operating at high modulation frequencies where the technical ($1/f$) noise is low.

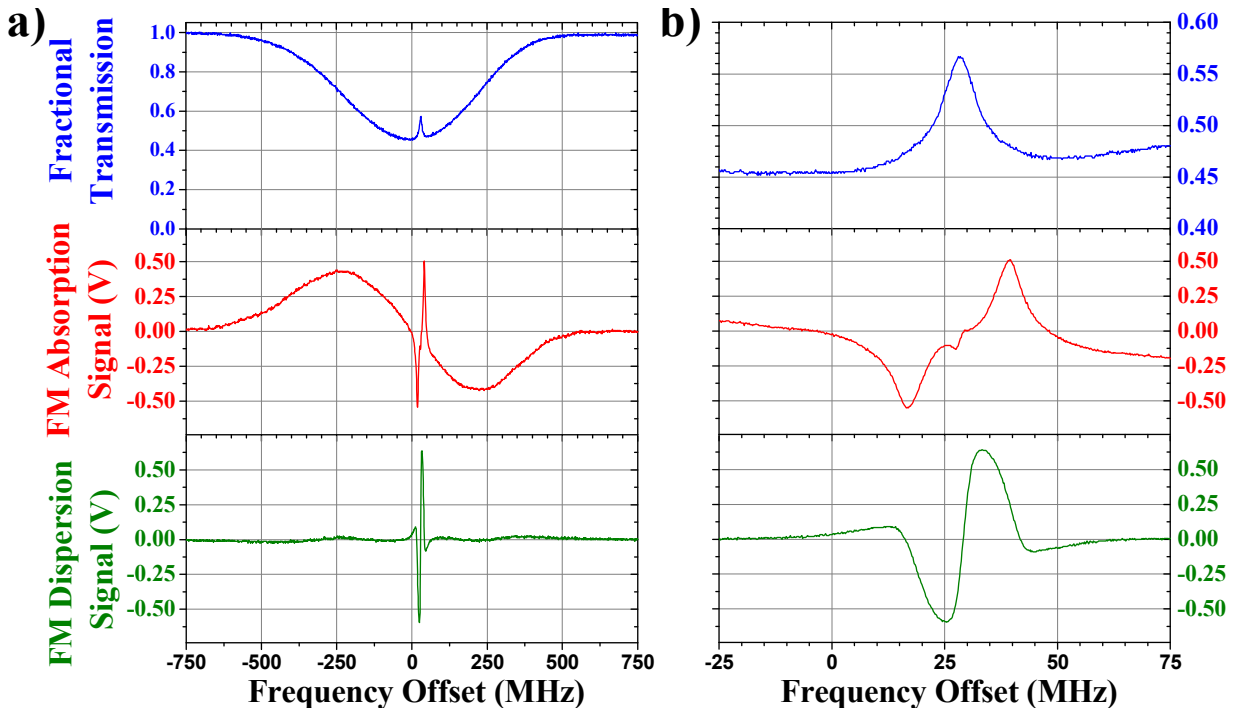

Figure 3.1 a) Saturated absorption fractional transmission, FM absorption signal, and FM dispersion signal versus frequency in kagome HC-PCF. Data were taken on the P(13) $\nu_1+\nu_3$ ro-vibrational transition. b) Zoomed in view of spectra in a).

FM spectroscopy is incorporated into the SAS setup by placing an EOM in the probe beam path. An EOM is a crystal whose refractive index changes in the presence of an external electric field, which is generally accomplished by placing parallel plates on either side of the crystal. These are commonly implemented in fiber coupled devices, where relatively small

voltages (<5 V) can operate the device at high RF frequencies (up to 10 GHz). Passing an optical laser beam through an EOM while driving the parallel plates with an RF modulation signal causes the incident light to experience phase modulation and takes the form

$$E_t(t) = E_0 \cos\left(f_{laser} t + M \cdot \cos\left(f_{\mathrm{FM}} t\right)\right). \tag{3.1}$$

where $E_t(t)$ is the transmitted electric field, E_0 is the amplitude of the incident field, f_{laser} is the frequency of the incident laser, M is the amplitude of the modulation signal (or modulation index), and f_{FM} is the frequency of the RF modulation. Using the trigonometric identity $\cos(a \pm b) = \cos(a)\cos(b) \mp \sin(a)\sin(b)$, Equation 3.1 can be rewritten as

$$E_t(t) = E_0\left(\cos\left(f_{laser} t\right)\cos\left(M \cdot \cos\left(f_{\mathrm{FM}} t\right)\right) + \sin\left(f_{laser} t\right)\sin\left(M \cdot \cos\left(f_{\mathrm{FM}} t\right)\right)\right). \tag{3.2}$$

There also exist identities to further expand the nested cosine terms, and are

$$\begin{aligned}\cos\left(M \cdot \cos\left(f_{\mathrm{FM}} t\right)\right) = {} & J_0(M) - J_2(M)\cos\left(2 f_{\mathrm{FM}} t\right) - J_{-2}(M)\cos\left(-2 f_{\mathrm{FM}} t\right) \\ & + 4J_{+4}(M)\cos\left(4 f_{\mathrm{FM}} t\right) + 4J_{-4}(M)\cos\left(-4 f_{\mathrm{FM}} t\right)...\end{aligned} \tag{3.3}$$

$$\begin{aligned}\sin\left(M \cdot \cos\left(f_{\mathrm{FM}} t\right)\right) = {} & J_1(M)\cos\left(f_{\mathrm{FM}} t\right) - J_{-1}(M)\cos\left(-f_{\mathrm{FM}} t\right) \\ & - 3J_3(M)\cos\left(3 f_{\mathrm{FM}} t\right) + 3J_{-3}(M)\cos\left(-3 f_{\mathrm{FM}} t\right)...\end{aligned} \tag{3.4}$$

where $J_n(M)$ is the n^{th} order Bessel function (n is an integer) evaluated at M. Substituting Equations 3.3 and 3.4 into 3.2 yields

$$\begin{aligned}E_t(t) = E_0 (& J_0(M)\cos\left(f_{laser} t\right) + \left(J_1(M)\cos\left(f_{\mathrm{FM}} t\right) - J_{-1}(M)\cos\left(-f_{\mathrm{FM}} t\right)\right)\sin\left(f_{laser} t\right) \\ & - \left(J_2(M)\cos\left(2 f_{\mathrm{FM}} t\right) + J_{-2}(M)\cos\left(-2 f_{\mathrm{FM}} t\right)\right)\cos\left(f_{laser} t\right) + ...\end{aligned}. \tag{3.5}$$

Equation 3.5 can be further simplified to the form

$$E_t(t) = E_0(J_0(M)\cos(f_{laser}t) + \left(J_1(M)\cos(f_{\mathrm{FM}}t) - J_{-1}(M)\cos(-f_{\mathrm{FM}}t)\right)\cos(f_{laser}t + \pi/2) + \left(J_2(M)\cos(2f_{\mathrm{FM}}t) + J_{-2}(M)\cos(-2f_{\mathrm{FM}}t)\right)\cos(f_{laser}t + \pi) + \ldots) \quad . \qquad 3.6$$

It can be shown that these individual cosine terms can be combined, and result in

$$E_t(t) = E_0(J_0(M)\cos(f_{laser}t) + J_1(M)\cos\left((f_{laser} + f_{\mathrm{FM}})t + \pi/2\right) + J_{-1}(M)\cos\left((f_{laser} - f_{\mathrm{FM}})t - \pi/2\right) + J_2(M)\cos\left((f_{laser} + 2f_{\mathrm{FM}})t + \pi\right) + J_{-2}(M)\cos\left((f_{laser} - 2f_{\mathrm{FM}})t + \pi\right) + \ldots) \qquad 3.7$$

where it is clear that the resulting output laser spectrum contains additional coherent components (called sidebands) at $f_{\mathrm{laser}} \pm n \cdot f_{\mathrm{FM}}$.

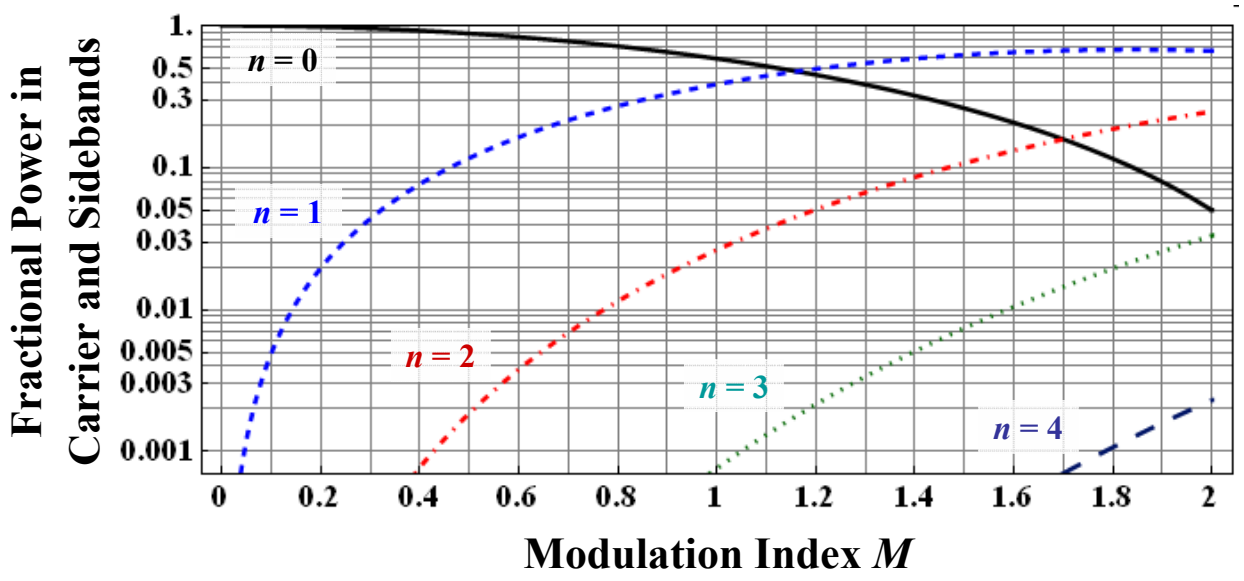

Figure 3.2 Fractional power in the output spectrum of an EOM as a function of *M*. The power of the incident wave and first through fourth order sidebands are included (*n* = 0, ±1, ±2, ±3, and ±4 respectively). It can be seen that for a modulation of 0.75 or less more than 99% of the power is contained within the central carrier and the first order sidebands. Also, when *M* = 1.15, approximately half of the power is contained within the first order sidebands.

If $M \leq 1$, the amount of power in the sidebands of order two or greater is much smaller than that of the power in the central carrier and the first order sidebands. Figure 3.2 shows a plot

of the fractional power contained within the central carrier and sidebands as a function of M (this is a root-mean-square (RMS) calculation, which effectively depends on $J_n^2(M)$). Therefore, only the first order sidebands are considered beyond this point, as values of $M \leq 1$ are used experimentally.

Ignoring all but the first order sidebands in Equation 3.7, the electric field of a laser transmitted through an EOM can be rewritten as $E_1(t) = \frac{1}{2}\left(\tilde{E}_1(t) + \tilde{E}_1^*(t)\right)$, where

$$\tilde{E}_1(t) = E_0\left(-\left(\frac{M}{2}\right)e^{i(f_{laser}-f_{FM})t} + e^{if_{laser}t} + \left(\frac{M}{2}\right)e^{i(f_{laser}+f_{FM})t}\right). \quad 3.8$$

If the light is then coupled into an acetylene-filled HC-PCF, each spectral component experiences a different attenuation (δ), phase shift (ϕ), and transmission (T) described by

$$\delta_j = \frac{\alpha_j L}{2} \quad 3.9$$

$$\phi_j = \frac{n_j}{c} L\left(f_{laser} + j \cdot f_{FM}\right) \quad 3.10$$

$$T_j = e^{(-\delta_j - i\phi_j)} \quad 3.11$$

where α is the absorption coefficient, L is the length of the sample, n is the refractive index of the sample, c is the speed of light, and j = 0, ±1, denoting the spectral components at f_{laser} and $f_{\text{laser}} \pm f_{\text{FM}}$, respectively. The transmitted field through the sample, $E_2(t) = \frac{1}{2}\left(\tilde{E}_2(t) + \tilde{E}_2^*(t)\right)$, is given by

$$\tilde{E}_2(t) = E_0\left(-T_{-1}\left(\frac{M}{2}\right)e^{i(f_{laser}-f_{FM})t} + T_0 e^{if_{laser}t} + T_{+1}\left(\frac{M}{2}\right)e^{i(f_{laser}+f_{FM})t}\right) \quad 3.12$$

Directing this light on a square-law detector results in an intensity $I_2 = \frac{c\left|\tilde{E}_2(t)\right|^2}{8\pi}$. Dropping terms of M^2, and assuming that the difference observed between the individual sidebands and the central carrier's absorption and phase shift are small (i.e. $\left|\delta_0 - \delta_{\pm 1}\right| \ll 1$ and $\left|\phi_0 - \phi_{\pm 1}\right| \ll 1$),

$$I_2(t) = \frac{cE_0^2}{8\pi}\left(1 + \Delta\delta \cdot M\cos\left(f_{FM}t\right) + \Delta\phi \cdot M\sin\left(f_{FM}t\right)\right) \tag{3.13}$$

where $\Delta\delta = \left(\delta_{-1} - \delta_{+1}\right)$ and $\Delta\phi = \left(\phi_{-1} + \phi_{+1} - 2\phi_0\right)$. Subsequently, mixing of the electronic photodetector signal with an RF signal at f_{FM} allows observation of either an absorption ($\Delta\delta$) or dispersion ($\Delta\phi$) signal. For the case of saturated absorption spectroscopy, the absorption and dispersion parameters are defined as

$$\delta(f) = \frac{A_g}{2} \cdot e^{-2\left(\frac{f - f_{C_2H_2}}{w_G}\right)^2} \cdot \left(1 - A_l \cdot \frac{\left(w_L\right)^2}{4\left(f - f_{C_2H_2} - \frac{1}{2}f_{AOM}\right)^2 + \left(w_L\right)^2}\right) \tag{3.14}$$

$$\phi(f) = \frac{A_g A_l}{2} \cdot \frac{2w_L\left(f - f_{C_2H_2} - \frac{1}{2}f_{AOM}\right)}{4\left(f - f_{C_2H_2} - \frac{1}{2}f_{AOM}\right)^2 + \left(w_L\right)^2} \tag{3.15}$$

where the parameters are defined in Equation 2.4.

The power incident on a photodetector with an area A is given by $P_2(t) = A \cdot I_2(t)$. Combining this with Equation 3.13 yields

$$P_2(t) = P_0\left(1 + \Delta\delta \cdot M\cos\left(f_{FM}t\right) + \Delta\phi \cdot M\sin\left(f_{FM}t\right)\right) \tag{3.16}$$

where $P_0 = A \cdot \frac{cE_0^2}{8\pi}$. The output current from the photodetector will contain DC and RF terms, and will be of the form $i_{total}(t) = i_{DC} + i_{RF}(t)$. The two components of the current are given by

$$i_{DC} = ge\eta \frac{P_0}{h f_{laser}} \tag{3.17}$$

$$i_{RF}(t) = ge\eta \frac{P_0}{h f_{\text{laser}}} \left(\Delta\delta \cdot M \cos\left(f_{FM} t\right) + \Delta\phi \cdot M \sin\left(f_{FM} t\right) \right) \tag{3.18}$$

where g is the electronic gain of the photodetector, e is the charge of an electron, and η is the optical-to-electrical efficiency of the detector.

It is useful to consider the signal-to-noise ratio (SNR) of the electrical modulation signal. The main sources of noise for this system are shot noise (i_{shot}) and thermal noise (i_T), as $1/f$ noise is negligible for lasers at RF frequencies. The root-mean-square (RMS) electrical noise power for these two noise processes depend on the square of the current, and add in quadrature ($\overline{i}_N^2 = \overline{i}_{shot}^2 + \overline{i}_T^2$) since they are uncorrelated. The RMS shot noise and thermal noise powers are given by

$$\overline{i}_{shot}^2 = 2ge i_{DC} \Delta f = 2g^2 e^2 \eta \left(\frac{P_0}{h f_{laser}} \right) \cdot \Delta f \tag{3.19}$$

$$\overline{i}_T^2 = \left(\frac{4kT}{R} \right) \cdot \Delta f \tag{3.20}$$

where Δf is the bandwidth of the detection electronics, k is Boltzmann's constant, T is the temperature, and R is the input impedance for the detection electronics. The SNR is then defined as

$$SNR = \frac{\overline{i}_{RF}^2}{\overline{i}_N^2} = \frac{\frac{1}{2} g^2 e^2 \eta^2 \left(\frac{P_0}{h f_{\text{laser}}} \right)^2 M^2 \left((\Delta\delta)^2 + (\Delta\phi)^2 \right)}{2 g^2 e^2 \eta \left(\frac{P_0}{h f_{laser}} \right) \cdot \Delta f + \left(\frac{4kT}{R} \right) \cdot \Delta f} \tag{3.21}$$

It should be noted that the electronic detection scheme that will be employed picks out either the absorption or the dispersion term.

Considering the two dominant noise processes in Equations 3.19 and 3.20 one can see that as the optical power is increased on the detector, the shot noise will dominate. This level occurs when

$$P_0 > P_{0,\min} = \frac{(2kT) \cdot h f_{laser}}{R g^2 e^2 \eta} \tag{3.22}$$

For the case of this experiment, T = 300 K, R = 40 kΩ (for the New Focus model 1811 125 MHz photodetector, listed in detail in Appendix B), g = 1, and η = 0.9, and result in $P_{0,\min} = 1.2\ \mu\text{W}$. Figure 3.3 shows a plot of the SNR for the 125 MHz and 1 GHz photodetectors (New Focus model 1611) with asymptotes for low and high power, and the transition between the two noise regimes can clearly be seen.

Because the saturation power of acetylene inside PCF is on the order of 20 mW, the probe beam can be on the order of several mW's without observing any considerable power broadening. In this case, the total electrical noise power becomes $\overline{i}_N^2 \simeq \overline{i}_{shot}^2$. Therefore, combining Equations 3.18 and 3.19, the SNR in Equation 3.21 simplifies to

$$SNR \approx \frac{\overline{i}_{RF}^2}{\overline{i}_{shot}^2} = \frac{\eta}{4\Delta f} \left(\frac{P_0}{h f_{\text{laser}}} \right) M^2 \left((\Delta\delta)^2 + (\Delta\phi)^2 \right) \tag{3.23}$$

Here it is clear that increasing probe power (P_0) or the modulation index M can increase the SNR.

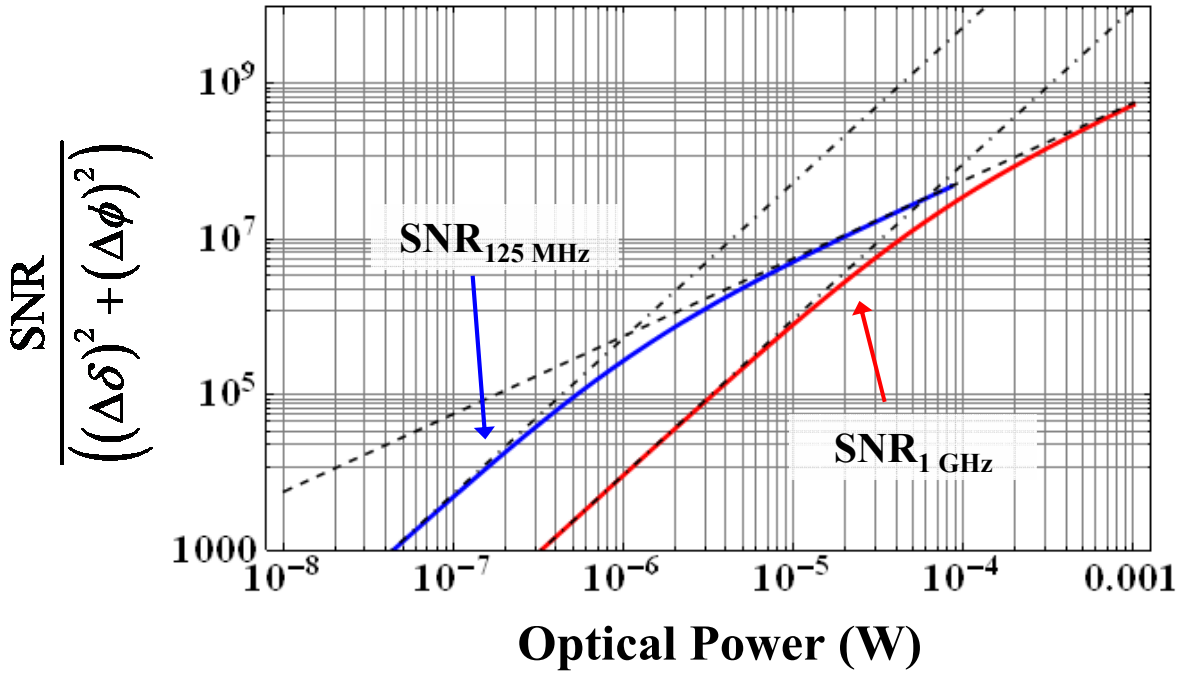

Figure 3.3 Plot of $\mathrm{SNR}/\left((\Delta\delta)^2+(\Delta\phi)^2\right)$ vs. optical power from Equation 3.21 for the 125 MHz (blue solid curve) and 1 GHz (red solid curve) New Focus photodetectors (listed in Appendix B). Also included are extrapolated fit lines of the SNR when thermal noise dominates at low power (dash-dotted lines) and when shot noise dominates at high power (dashed lines). The transition between these two processes occurs where the two extrapolated lines intersect, and is around 1.2 μW and 50 μW for the 125 MHz and 1 GHz detectors, respectively. The 125 MHz detector saturates near 80 μW of optical power, while the 1 GHz detector saturates near 1 mW.

It is also useful to make experimental observations of the noise level in our system to determine if we are in fact limited by the optical shot noise. If we are limited by the optical shot noise, then the ratio of the shot noise to the mean optical power will be the same as the ratio of the shot noise on the current to the DC current level generated at the photodiode. This ratio will also determine the shot noise level on the voltage produced from the photodetector's gain circuit, and all three quantities are related by

$$\frac{\bar{P}_{0,shot}}{P_0}=\frac{\bar{i}_{shot}}{i_{DC}}=\frac{\bar{V}_{shot}}{V_{DC}} \qquad 3.24$$

where V_{DC} is the voltage produced by the photodetector's amplification circuit. It is useful to use the relation

$$P_0 = \frac{V_{DC}}{G_{trans} R_\lambda} \tag{3.25}$$

to convert the optical power into an experimentally measurable voltage (G_{trans} and R_λ are the transimpedance gain and responsivity of the photodetector, respectively). The electrical shot noise power of the photodetector (with light) can then be calculated by

$$P_{ele,shot} = \frac{\overline{V}_{shot}^2}{R} = \left(\frac{\overline{i}_{shot}}{i_{DC}} \right)^2 \frac{V_{DC}^2}{R} = 2geG_{trans} R_\lambda \left(h f_{laser} \right) \frac{V_{DC}}{R} \Delta f \tag{3.26}$$

where R is 50 Ω, corresponding to the input impedance of the spectrum analyzer (Equations 3.18, 3.19, 3.24, and 3.25 have been used for simplification). Power on a spectrum analyzer is typically reported in decibels with respect to 1 mW (dBm), which makes Equation 3.26 become

$$P_{ele,shot(dBm)} = 10 \log_{10} \left(\frac{2geG_{trans} R_\lambda \left(h f_{laser} \right) \frac{V_{DC}}{R} \Delta f}{0.001\,\mathrm{W}} \right). \tag{3.27}$$

A calculation of the shot noise power level for 67 μW of optical power on the 125 MHz photoreceiver yielded a level of -77 dBm. Experimentally, a power level of -79 dBm was measured, in good agreement with calculation. The optical power was ultimately limited by the saturation level of the 125 MHz. Due to the consequences of Equation 3.23, a 1 GHz photodetector was eventually employed to allow higher optical probe powers to be used, effectively increasing the SNR.

If the electronic signal from Equation 3.18 is sent to an RF mixer also driven at f_{FM}, the absorption or dispersion can be extracted. Due to the mixing process, the resulting signal has

components at DC and $2f_{FM}$. Therefore a low-pass filter is used to isolate the DC signal (shown in Figure 3.4) which is useful for laser frequency stabilization.

FM spectroscopy: experimental schematic and observed spectra

FM spectroscopy is observed in acetylene-filled HC-PCF, and the schematic for this experiment is shown in Figure 3.4. There are a couple of differences between this setup and the saturated absorption spectroscopy setup in Chapter 2. The first is the presence of a fiber EOM in the probe path. The second is the presence of a fiber amplitude modulator (AM) before the EDFA. This modulates the pump beam, which effectively removes any voltage offsets on the error signal (this amplitude modulation produces a signal which is the difference between when the pump is on and off, and the voltage offsets observed are either due to the Doppler background or the fiber guidance, and are typically on a much slower time scale than this modulation frequency). Because of optical power limitations on both the EOM and AM, and due to the fact that these modulations need to be applied separately to the probe and pump beam, the setup in Figure 2.2b is the basis for this experiment. Finally, a fiber splitter has been added before the interferometer to provide light for the heterodyne experiment necessary to fully characterize the laser after stabilization has been achieved.

Laser stabilization is achieved by employing an FM spectroscopy technique capable of detecting Doppler-free dispersion signals. The optical and electrical schematics for cw laser stabilization are shown in Figure 3.4, and contain slight modifications of the optical setup in Figure 2.2. The probe beam passes through a fiber EOM (General Photonics $LiNbO_3$ phase modulator) to generate FM sidebands (f_{FM} = 22 MHz) where 50% of the carrier power is shifted into the first order sidebands ($M \sim 1$). Also, amplitude modulation (f_{AM} = 900 kHz) of the pump is used to reduce offsets due to the Doppler-broadened background. A high bandwidth PD (New Focus 1811-FC) is used to detect the modulation frequencies and requires fiber coupling via the PD fiber. The PD signal is filtered, amplified, and mixed at both f_{FM} and f_{AM} to observe a Doppler-free absorption signal shown at the bottom left corner of Figure 3.5. This dispersion feature with odd-symmetry is used as the input error signal to servo the cw fiber laser to the P(13) transition of the $v_1 + v_3$ ro-vibrational transition in $^{12}C_2H_2$.

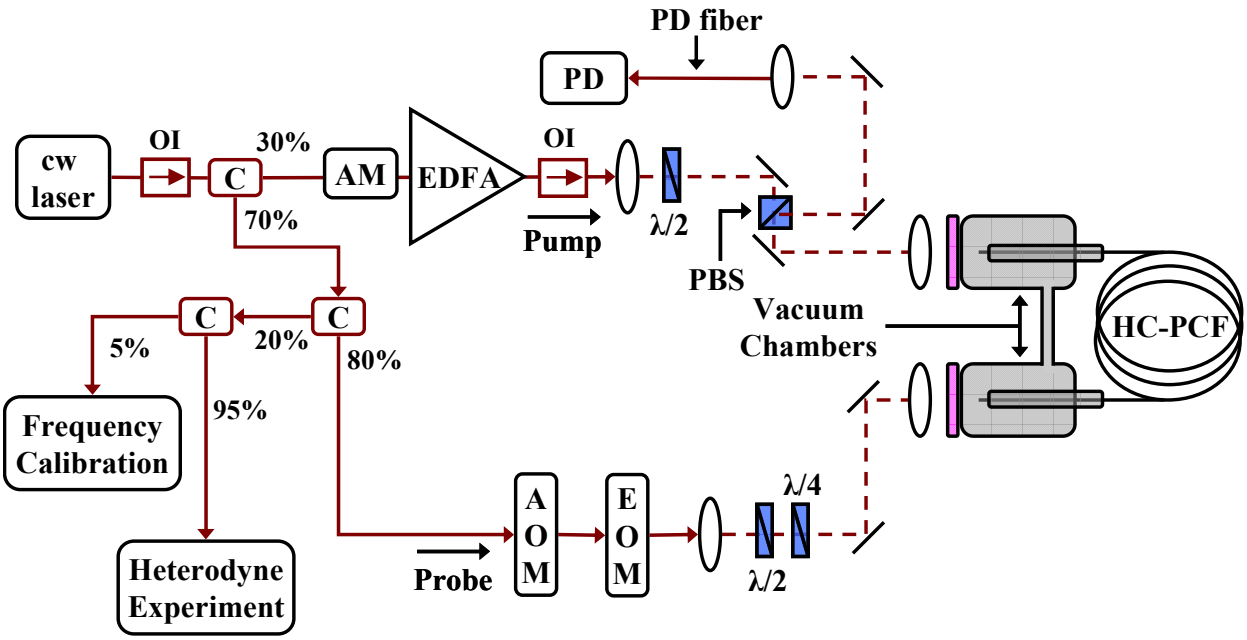

Figure 3.4 Optical schematic for FM spectroscopy inside HC-PCF. The schematic is similar to Figure 2.2b, and differs only in the couplers used to split a portion of the probe beam for the heterodyne experiment. Also, an EOM phase modulates the probe beam directly after the AOM stage. The probe passes through the acetylene-filled HC-PCF and is detected by the PD, whose electrical signal is sent to a servo circuit after demodulation. Also, the pump beam is amplitude modulated (before amplification), which requires another stage of demodulation but offers reduced noise on the final error signal and ensures a minimization of offsets.

The error monitor (or the input to the servo controller) can be analyzed before and after laser stabilization to determine how well the laser is locked. To do this, the error monitor was sent to a fast Fourier transform (FFT) spectrum analyzer (which is a type of electrical spectrum analyzer that can make accurate low frequency measurements) to observe the spectral content below 100 kHz. Figure 3.6 shows that when the laser is locked the low frequency components (up to 3 kHz) are slightly reduced while higher frequency components are increased. This increase is called a "servo bump" and is typical for servo controllers. This result indicates that we are stabilizing the laser to the acetylene transition for low frequencies at the expense of adding faster noise components.

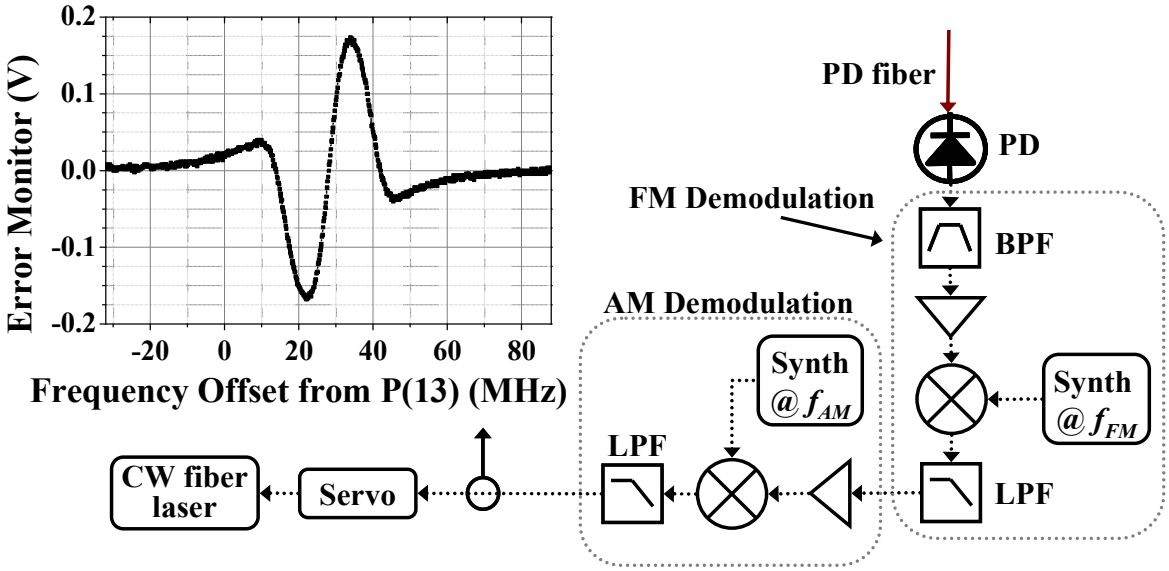

Figure 3.5 Electrical schematic for FM spectroscopy. The probe signal is directed onto a photodetector and then sent to the FM demodulation circuit ($f_{FM} = 22\,\text{MHz}$). Demodulation consists of a band-pass filter (BPF), an amplifier, a mixer driven at the desired demodulation frequency, and a low-pass filter (LPF). The resulting signal is then sent to the AM demodulation circuit ($f_{AM} = 900\,\text{kHz}$), which produces the signal shown in the graph. This signal serves as the error signal for standard servo electronics which feeds back to the fiber laser's PZT to stabilize the optical frequency.

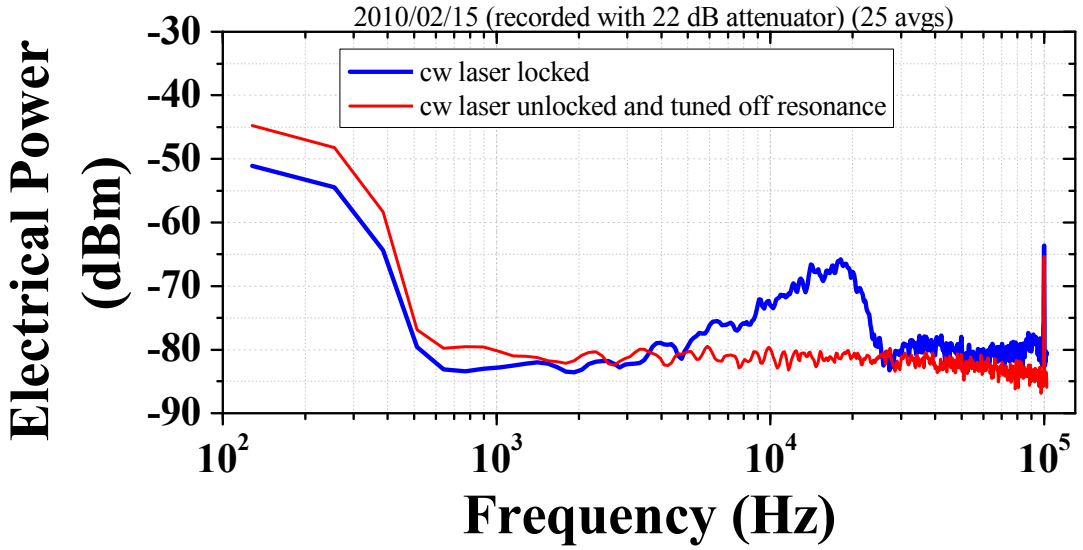

Figure 3.6 The error signal power spectrum when the cw laser is locked (blue) and unlocked (red). The PZT on the fiber laser only allows feedback up to approximately 20 kHz, indicated by the "servo bump" in the locked signal. Because the fiber laser is inherently very narrow, the noise spectrum is not significantly reduced. Resolution for this measurement was 128 Hz.

This type of analysis is characterized as an "in-loop" measurement because we are using the electronic stabilization signal to characterize the laser's stabilization. In-loop measurements are not adequate to fully characterize a reference. The reason for this is that any additional noise on the electronic locking circuits can be written onto the stabilized cw laser, and will not be observable at the error monitor output. An example of this would be noise that is on the electrical power lines in the laboratory. This noise could be transferred to the electronic locking circuit, and therefore written onto wall outlet lines, but might not be detected by the FFT spectrum analyzer (if the noise is written onto this machine as well). As it has been mentioned previously, the only accurate way to fully characterize a frequency reference is through a heterodyne experiment with another optical reference. The results of these "out-of-loop" measurements are the topic of Chapter 4.

CHAPTER 4 - Frequency reference characterization

Frequency references are characterized by their frequency stability and frequency accuracy. Both of these quantities can be degraded by systematic (non-random) and random noise processes. Errors in calibration or observed frequency drifts are examples of systematic noise processes, while electronic shot noise is a common random noise process. Basic statistics such as the mean and the standard variance can be used to describe the quality of a reference, though the sample variance for several noise types does not converge as the number of samples grows (such as flicker and random walk noise). As a result, neither of these statistics gives specific information on the reference's stability. An example of this is shown in the right-most graph in Figure 4.1, where the average frequency versus time is plotted for a reference that is both stable and accurate. The leftmost graph shows a stable but inaccurate reference, whose standard deviation would be similar to the aforementioned. However, if one considers the middle two graphs, the mean and standard deviation appear to be similar despite the two references' different behavior. It becomes apparent in these instances that the standard statistics cannot completely characterize references with frequency drift versus time.

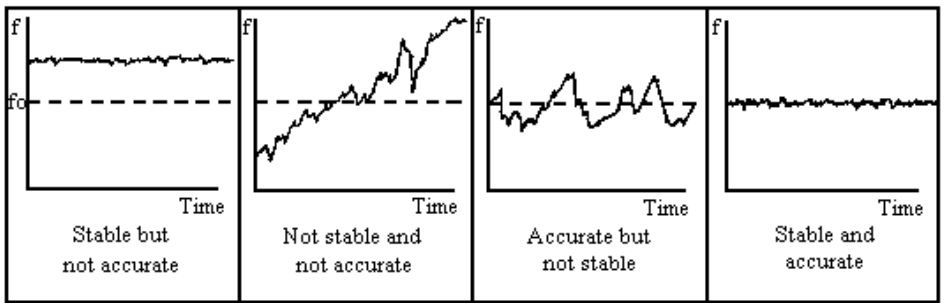

Figure 4.1. Average frequency value of several different frequency references vs. time illustrating the difference between accuracy and stability (taken from Ref [46]).

A different way to calculate frequency stability was proposed by D.W. Allan to better characterize frequency references. This new quantity, called the two-sample variance or the Allan variance, has the ability to identify different noise types, converges for most noise types at large sample numbers, and uses the standard experimental implementation for data collection.

The Allan variance differs from the standard variance in that the point to point deviations are analyzed instead of the deviations from the mean, and is defined as

$$\sigma_y^2(\tau) = \frac{1}{2}\left\langle \sum_{n=1}^{N} \left(y_{n+1} - y_n\right)^2 \right\rangle \qquad 4.1$$

where y_n is the n^{th} frequency measurement which has been averaged for a time τ. It is shown in Ref. [47] that $\sigma_y^2(\tau) \sim \tau^{\mu}$ where $-2 \le \mu < 2$ and μ corresponds to different noise types. These different noise types are generally defined by their power spectral density (S_y) which take on the form

$$S_y(f) = f^{\alpha} \qquad 4.2$$

where $-3 < \alpha \le 2$ and is related to μ by the relation $\alpha = -\mu - 1$ (except for $\alpha = 2$).

Direct frequency measurements of an optical source are not possible due to speed limitations of electronic detectors, though indirect measurements are possible through a heterodyne comparison with another reference. Frequency chains, where RF and optical references were linked together through various heterodyning stages, were first used as a stable, accurate reference in the heterodyne experiment [48]. While this type of frequency reference does offer broad spectral coverage, there are regions in the spectrum that cannot be covered due to available cw laser sources (or require additional complicated nonlinear experiments to produce spectra in this region). This detriment limits frequency chains' usefulness for some spectroscopic applications, and the complicated electronic and optical setup limits their availability.

Frequency combs are an alternative to frequency chains, and rely on the output of a single mode-locked laser to provide a broad spectrum of coherent frequencies. The coherence of sequential laser pulses from a mode-locked laser was first shown in Ref. [49], and eventually led to an understanding of pulses in the time and frequency domain shown in Figure 4.2 (taken from Ref. [50]). It took nearly 20 years of development to fully understand and control the output spectrum of these lasers [51] due in large part to available mode-locked lasers and nonlinear

materials. One major advance was the discovery of Kerr-lens-mode-locking of Ti:sapphire lasers that produced very short pulses in the time domain and therefore had very large spectral bandwidths. Additionally, nonlinear fibers (which allow low-loss guidance in small cores over several meters) were manufactured that are suitable for broadening the spectrums of these lasers. This spectral broadening allows stabilization of all the frequency components in the comb, making it a very useful spectral ruler.

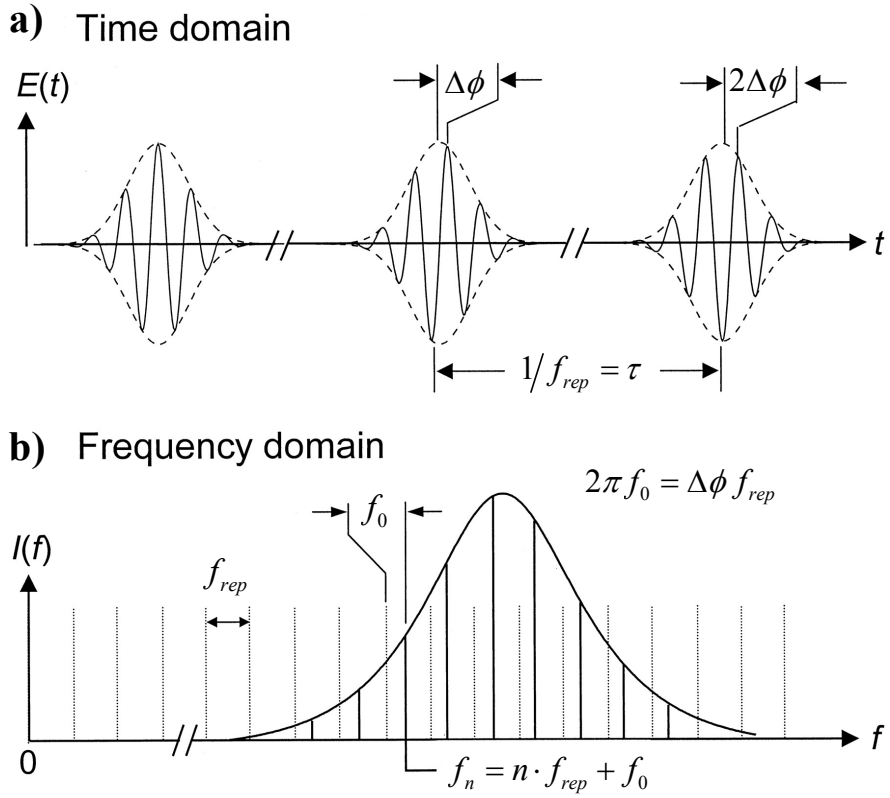

Figure 4.2 Time and frequency domain of the output of a stabilized mode-locked laser (taken from Ref. [50]). a) In the time domain, pulses are separated by τ (or f_{rep}), and the phase of the electric field evolves from pulse to pulse in a deterministic manner ($\Delta\phi$). b) In the frequency domain, spectral components are spaced by f_{rep}, and are offset from DC by f_0.

The temporal output of a stabilized mode-locked laser, or frequency comb, has two characteristic components; namely the time between pulses (τ) and the phase evolution ($\Delta\phi$) between the peaks of the electric field and the pulse envelope (Figure 4.2a). Considering the frequency components necessary to produce these short pulses by means of a Fourier transform, it becomes apparent that there are two characteristic quantities in the frequency domain (Figure

4.2b). They are the repetition frequency (f_{rep}) and the carrier-envelope offset frequency (f_0) and are related to the time domain components by [50]

$$f_{\text{rep}} = \frac{1}{\tau} \tag{4.3}$$

$$2\pi f_0 = \Delta\phi\, f_{\text{rep}} \tag{4.4}$$

The individual spectral components in this spectrum are evenly spaced by f_{rep}, and are offset from DC by f_0. Therefore, knowledge of the integer mode number, n, of a given comb "tooth" (or discrete spectral component) allows precise knowledge of the comb tooth's frequency, and is given by

$$f_n = n \cdot f_{rep} + f_0 . \tag{4.5}$$

Stabilization of a frequency comb's repetition frequency is relatively simply to accomplish. First, a portion of the laser's output is detected on a fast photodetector. The RF spectrum of the photodetector will contain frequency components at integer multiples of f_{rep} due to the individual modes interfering with one another. This signal is filtered so that only one of these interference frequencies is present and is then sent to a servo that changes the length of the cavity (typically accomplished through a PZT of some form).

Stabilization of f_0 is a bit more involved experimentally because it typically requires broadening the output spectrum of the laser to span an octave. This technique is known as self-referencing [50], and uses a nonlinear crystal to double a low frequency component of the spectrum to interfere with a high frequency component (also known as an f-2f interferometer). If the n^{th} tooth of the comb is frequency doubled (using a nonlinear process), the resulting frequency of this spectral component will occur at $2f_n = 2n \cdot f_{\text{rep}} + 2f_0$. If this spectral component is then interfered with the $2n^{\text{th}}$ component of the comb (whose frequency by definition is $f_{2n} = 2n \cdot f_{\text{rep}} + f_0$ from Equation 4.5), difference frequency generation allows

observation of f_0. This signal is then filtered and sent to a servo that feeds back to an intracavity dispersion mechanism (detailed for individual combs in the following section).

Frequency comb stabilization vastly simplifies both the setup and operation of a vast array of phase-stabilized optical frequency components when compared with frequency chains. The techniques for comb stabilization have been well studied, and are implemented in this work in a few different ways that depend on the particular type of laser that the comb is based on. The following section gives a general overview of the three different types of frequency combs used in this experiment along with their mechanisms used for stabilization.

Frequency combs used in the heterodyne experiment

Three different frequency combs were used to test both the accuracy and stability of the cw acetylene reference. The first comb listed below is based on a free-space laser, and is similar to previous Ti:sapphire combs where the repetition frequency can be altered by changing the length of the free-space cavity. The necessary task of changing the repetition frequency is detailed in the absolute frequency measurement section. The two following combs are fiber based, and offer much easier operation compared to the free-space comb while also adding the advantage of being portable by nature. A general summary of each comb is listed below along with references containing more detailed operation.

Free-space Cr:forsterite laser frequency comb

A free-space prism-based Cr:forsterite (Cr:f) laser was used as the basis for a near-IR frequency comb due to the ability to make large (~kHz) changes to the repetition frequency while it was stabilized [52]. A schematic of this laser is shown in Figure 4.3a where a linear cavity with prisms used for dispersion compensation is implemented. The operation of this laser (conducted by Rajesh Thapa and Karl Tillman) is similar to Ti:Sapphire lasers, although the Cr:f crystal must be chilled to -10 deg C to achieve lasing. Typically, frequency stabilization only lasted for an hour or two which made it difficult to collect long-term stability data with this comb. The schematic for the f-2f interferometer and a typical spectrum of the supercontinuum (SC), or the broadened output spectrum that achieves an octave of bandwidth, are also included in Figure 4.3b and c.

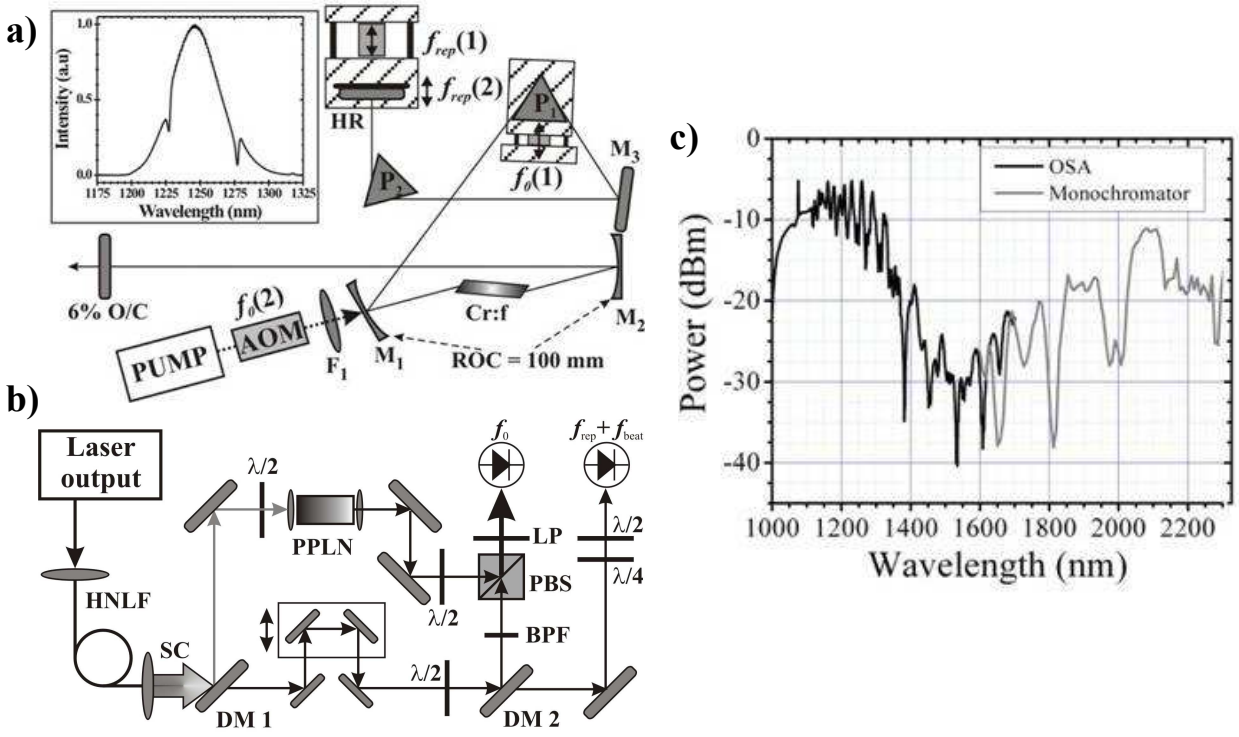

Figure 4.3. a) Free-space Cr:f laser using prisms for dispersion compensation. Also indicated are the various mechanisms for stabilizing both the repetition frequency and the carrier-envelope frequency. Listed are high reflector (HF), prisms (P), and radius of curvature (ROC) of the indicated mirrors. b) f-2f interferometer schematic for f_o stabilization. Listed are highly nonlinear fiber (HNLF), supercontinuum (SC), dichroic mirror (DM), and periodically poled lithium niobate (PPLN). c) Output spectrum of the Cr:f comb. These figures are taken from Ref. [53].

Two sets of control schemes were necessary for the stabilization of f_{rep} and f_0 due to the large frequency noise and drift observed with this laser. The repetition frequency of this laser was stabilized by sending control signals to two PZTs (with different response bandwidths) attached to the cavity's high reflector that allowed for coarse and fine frequency stabilization. The carrier-envelope offset frequency was coarsely stabilized by moving one of the cavity prisms in and out of the laser beam path by means of an attached PZT to change the intracavity dispersion. Because of the prism's relatively large mass (compared with the PZT), only slow fluctuations were removed from f_0. Therefore, an AOM was placed directly after the pump laser to control the peak power in the laser cavity (which in turn also affected the cavity

dispersion). In this comb, f_{rep} was generally stabilized near 125 MHz and due to available electronic filters f_0 was stabilized near 35 MHz.

Figure-8 fiber laser frequency comb

A fiber laser frequency comb was made available by Dr. Brian Washburn and Jinkang Lim, and is similar to the one described in Ref. [54]. The laser itself consists of two loops of fiber (thus making a "figure-8") which contain polarization controllers, an isolator, and erbium fiber as the gain material (shown in Figure 4.4). Light is coupled out of the laser via a coupler, amplified, and then sent to another fiber stage for SC generation. Amplification is achieved by using erbium doped fiber which is pumped in both the forward and backward directions with 1480 nm laser diodes. This allows high enough pulse powers to be reached so that the following highly nonlinear fiber (HNLF) broadens the spectrum of the laser pulses until an octave is covered. A free-space f-to-2f interferometer is then used to detect f_0, which is suitable for stabilization.

The two control mechanisms used for comb stabilization in this setup are a PZT attached to a section of the fiber cavity to control the length of the cavity (and thus f_{rep}) and the current on the pump laser diode which changes the intracavity pump power (and stabilizes f_0). Typically, f_{rep} was stabilized near 113 MHz while f_0 was stabilized anywhere from 60-90 MHz (due to the range of the tunable band-pass filter used to isolate f_0).

This comb was easier to operate than the Cr:f comb, but occasionally offered challenges in maintaining stabilization for extended periods (more than 4-5 hours). To achieve this length of stabilization time, the comb was enclosed in a Plexiglas box where the figure-8 laser was directly mounted on a water-cooled plate for active temperature control.

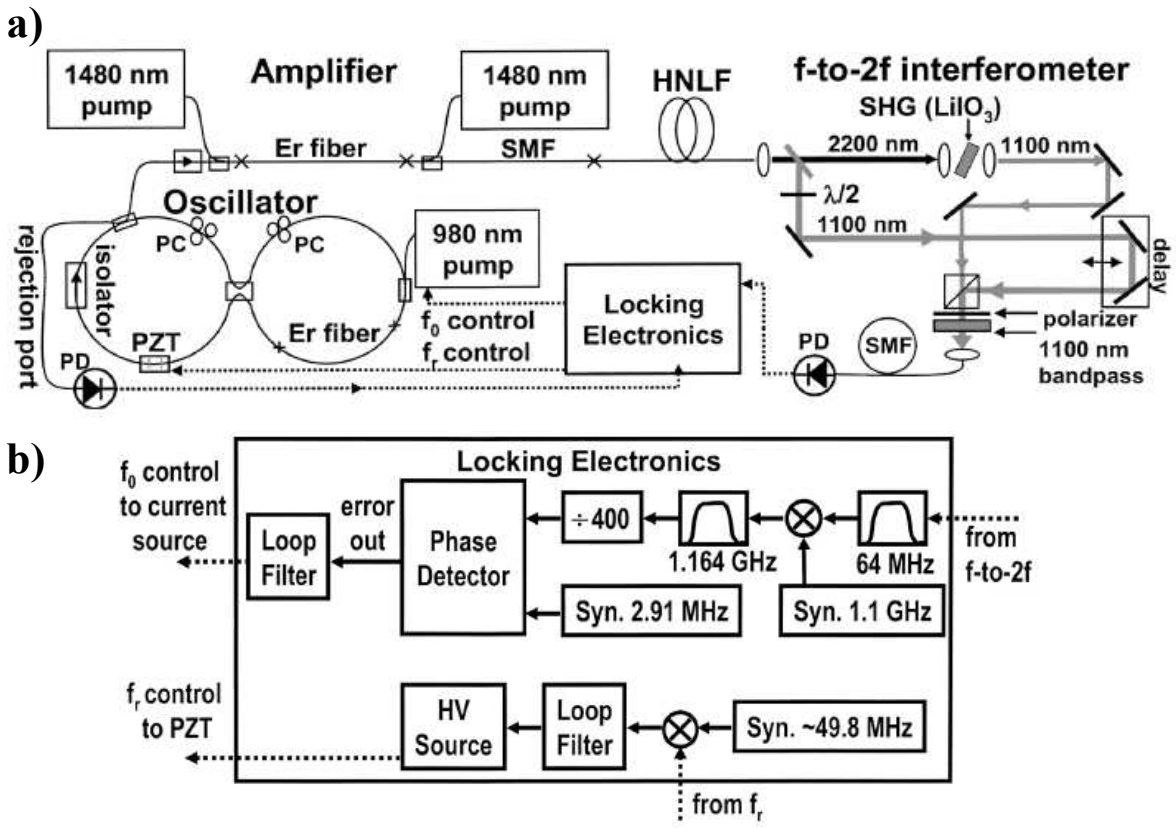

Figure 4.4 Figure-8 fiber laser frequency comb schematic, reproduced from Ref. [54]. a) Optical schematic for the laser, supercontinuum generation, and f-2f interferometer. In this figure, the repetition frequency is indicated as f_r. b) Electrical schematics for stabilizing f_{rep} and f_0.

Carbon nanotube fiber laser frequency comb

The most convenient comb available for the heterodyne experiment was the self-starting carbon nanotube fiber laser (CNFL) frequency comb [55] shown in Figure 4.5 (the CNFL was created by Jeff Nicholson at OFS laboratories and the SC generation and comb stabilization were accomplished by Dr. Washburn and Jinkang Lim). The CNFL has a ring configuration where the carbon nanotubes act as a saturable absorber inside the cavity, and are placed on the end of an optical connector of a PZT fiber stretcher which is used to control the cavity length. The laser is followed by a parabolic pulse fiber amplifier which uses a low-dispersion-slope HC-PCF [56] before a supercontinuum is generated in the highly nonlinear fiber.

Similar to the figure-8 comb, feedback to a PZT and the current of the pump laser diode are used to stabilize f_{rep} and f_0. Here f_{rep} was stabilized near 167 MHz while f_0 was stabilized anywhere between 60 and 130 MHz.

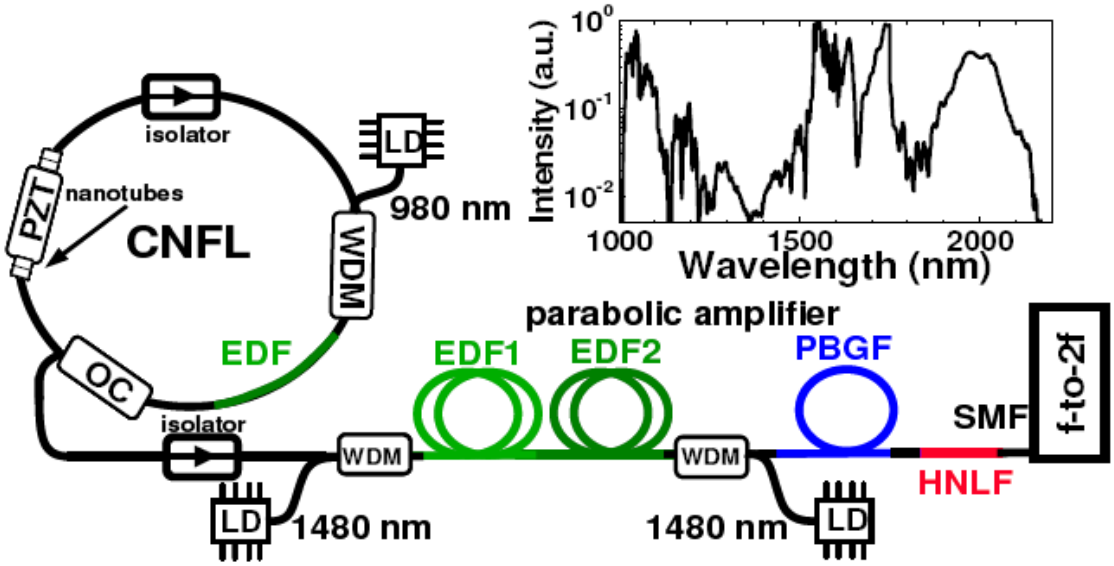

Figure 4.5 Schematic of the phase-stabilized CNFL frequency comb from Ref. [55]. LD: laser diode; OC: output coupler; WDM: wavelength division multiplexer; PZT: piezo-electric transducer; EDF: erbium-doped fiber; PBGF: photonic bandgap fiber; SMF: single mode fiber. Inset: the supercontinuum after the HNLF.

Frequency stabilization of combs to a GPS-disciplined Rb clock

Frequency combs can be stabilized very precisely to either optical or electrical frequency references. Referencing a comb to an atomic clock would result in the highest stability and accuracy currently available. However, atomic clock setups are generally expensive and are not available at Kansas State University. An alternative to using an atomic clock is using a global positioning system (GPS) disciplined rubidium clock receiver and is the system used for the measurements presented in this work. At short time scales (< 1 day), the Rb reference determines the instability of this reference. To obtain long term stability, the Rb/GPS is synchronized to several (typically 9) GPS satellites that are in turn synchronized to a laboratory atomic clock. The particular unit used is a Precision Test Systems model GPS10RB GPS-disciplined Rb oscillator (Rb/GPS) and generates several stable 10 MHz signals that are used as

references for all frequency counters and the comb synthesizers [57]. The behavior of this particular unit is specified to give a fractional frequency instability of approximately $2\times10^{-11}\,\tau^{-1/2}$ (where τ is the averaging time). This reference is ultimately limited by the short term instability of the Rb oscillator.

While combs can be frequency stabilized with very high precision, the easiest way to measure this is to compare with a more stable source. Alternatively, comparing two combs directly (although they would ideally have the same stability) could be done to verify that the stability of the Rb/GPS is being transferred without any additional instability. However, due to the different repetition frequencies of our various frequency combs, a problem arises from the fact that the pulses in the time domain will only overlap at the least common multiple of the time between pulses for the two combs. For the case of the Cr:f comb and the CNFL comb (with f_{rep}'s near 125 MHz and 167 MHz, respectively), the time between pulses would be approximately 8 and 6 ns, respectively. This means that every 3$^{\text{rd}}$ pulse from the Cr:f comb would interact with 4$^{\text{th}}$ pulse from the CNFL comb which would reduce the overall SNR of this measurement (as compared with the case where both repetition frequencies were equal). Further complicating this measurement is the different phase evolutions both combs would experience. This would result in further reduction of the SNR due to the different temporal positions of the electric fields' peak for each set of interfering pulses.

An alternate approach can be taken to characterize the stability of the frequency combs. This method relies on interfering both combs separately with the cw reference and is shown in Figure 4.6a. When conducting a single heterodyne experiment, the Allan deviation that is calculated from this measurement merely sets an upper limit for the instability of both references. However, if a third reference is used so that three separate heterodyne experiments are conducted simultaneously, the exact uncertainty for each reference can be determined (not simply an upper limit) [58, 59]. This is known as a "3 cornered hat" technique. For the reasons listed above, the third corner of this triple heterodyne experiment is not possible due to the particular frequency combs that are available. Therefore, we have conducted a "2/3 cornered hat" measurement (where only two heterodyne experiments are conducted simultaneously). While this measurement does not allow for absolute characterization for any single reference, it does accomplish an indirect comparison of the two combs. Because both combs are referenced to the same Rb/GPS unit, this measurement sets an upper limit to how well the combs are

referenced to this reference. Figure 4.6b shows the fractional frequency instability of the two heterodyne experiments (which appear to lie on top of one another) from Figure 4.6a. Also plotted is the fractional frequency instability of the difference between the two beat notes (where any fluctuations due to the cw acetylene reference have been subtracted from one another). This calculation effectively sets an upper limit on the stabilization ability of both combs (approximately $3\times10^{-12}\,\tau^{-1/2}$), which is well below the Rb/GPS quoted instability of $2\times10^{-11}\,\tau^{-1/2}$, and shows that the instability of the Rb/GPS is indeed transferred to the frequency combs without any extra noise.

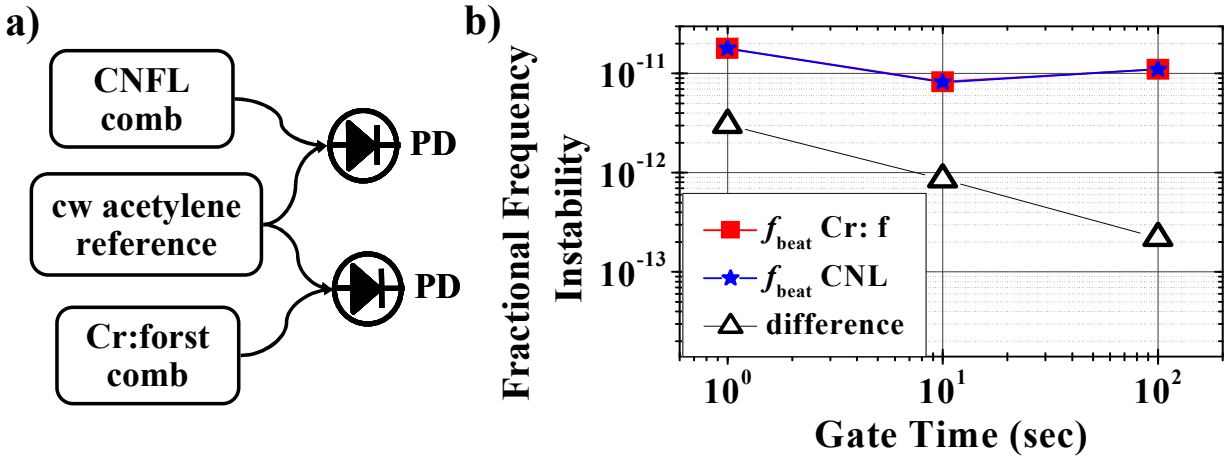

Figure 4.6 Block schematic and fractional frequency instability of the 2/3 cornered hat experiment. a) The output of each indicated comb is combined with a portion of the cw acetylene reference in fiber couplers, and then separately heterodyned on a photodetector. This allows both beat notes to be counted simultaneously. b) Fractional frequency instability of both beat notes (recorded over the same time interval) versus averaging time. Also plotted is the instability of the difference between the two beat notes, setting an upper limit for the instability between the two combs. This, however, does not give any information on the stability of the Rb/GPS reference since it is common to both measurements.

Accuracy measurements

The first quantity considered to fully characterize this cw optical reference is the accuracy of its absolute frequency. A schematic of the optical heterodyne measurement is given in Figure 4.7a, while a conceptual representation of what is occurring in the frequency domain is listed in Figure 4.7b. The comb is first filtered with a fiber-coupled optical band-pass filter, and then combined with the cw reference in a fiber coupler. This heterodyne signal is then directed

onto a photodetector, which is band-pass filtered in the RF domain and amplified. The fundamental comb parameters, f_{rep} and f_0, are counted with HP53132A 12-digit frequency counters, and the RF heterodyne signal (f_{beat}) and the AOM used in the cw reference (f_{AOM}) are counted with HP53131A 10-digit frequency counters. To make this accuracy measurement, it was necessary to use the Cr:f frequency comb because it facilitates large changes in its repetition frequency (on the order of kHz).

To explain the significance of the data taken in this section, a basic understanding of the relation between the frequency comb and the cw reference is necessary. The optical reference's frequency (f_{laser}) and the nearest comb tooth's frequency (f_n) are given by the equations

$$f_{laser} = f_x + \tfrac{1}{2} f_{AOM} \tag{4.6}$$

$$f_{laser} \pm |f_{beat}| = f_n \tag{4.7}$$

where f_x is the experimental frequency of the P(13) $v_1 + v_3$ ro-vibrational transition in $^{12}C_2H_2$, f_{AOM} is the frequency of the probe beam's AOM, f_n is the frequency of the nearest comb tooth, and n is the integer mode number of this nearest tooth. Combining Equations 4.5 - 4.7 yields

$$f_x + \tfrac{1}{2} f_{AOM} \pm |f_{beat}| = n \cdot f_{rep} \pm |f_0| . \tag{4.8}$$

The signs of f_{beat} and f_0 are ambiguous due to the mixing process, and are determined by changing the frequency lock point of both f_{rep} and f_0 while observing f_{beat}. The absolute frequency of the reference cannot be determined in a single measurement due to the uncertainty in determining n (due to the mode spacing of the laser being below the spectral resolution of optical spectrum analyzers).

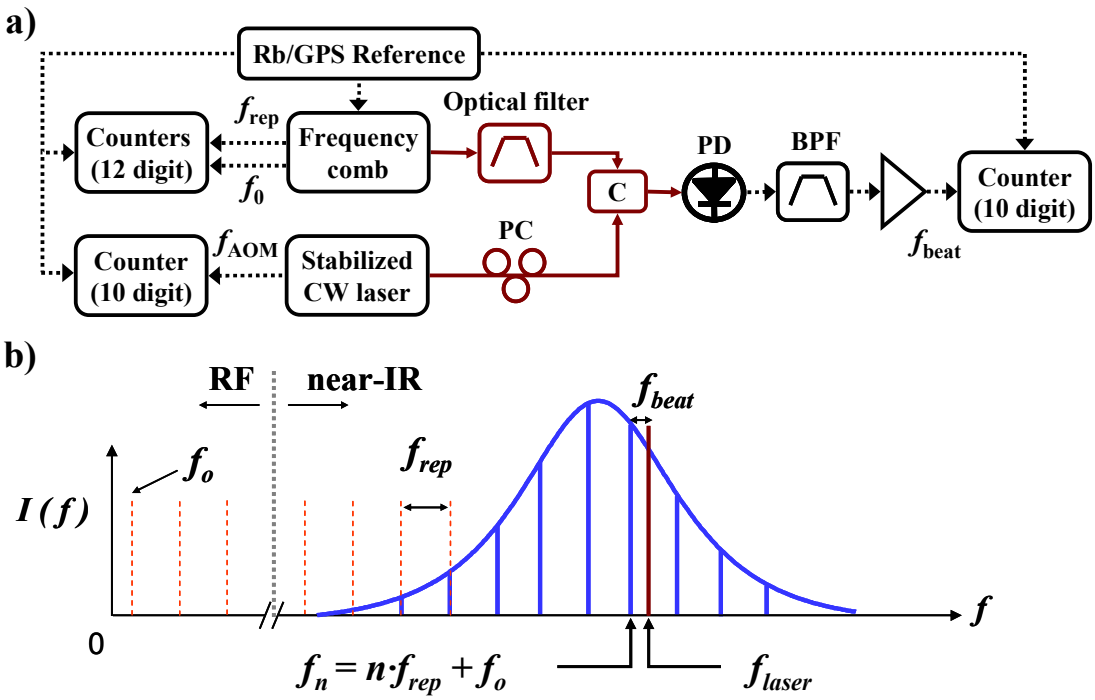

Figure 4.7 a) Optical and electrical schematic for the heterodyne beat between a frequency comb stabilized to a rubidium-disciplined GPS clock (Rb/GPS) and a cw laser stabilized to $^{12}C_2H_2$ inside kagome HC-PCF. Solid red lines indicate optical fiber coupling and dotted black lines indicate electrical connections. Shown are a fiber coupler (C), fiber polarization controller (PC), photodetector (PD), and electrical band-pass filter (BPF). b) Spectrum of the frequency comb with the cw reference (f_{laser}). There is a discontinuity in the frequency axis to show both the RF and near-IR domains. Red dotted lines indicate positions of individual comb teeth that have little or no power, while solid blue lines indicate teeth with observed optical power. Individual frequencies are listed in detail in this section.

The reference's frequency is therefore calculated by using a technique similar to Ref. [60] which uses a Vernier approach. After an initial heterodyne measurement, the repetition frequency is changed such that f_{beat} represents the beat between the optical reference and the $n+m^{th}$ comb tooth, where the integer m can be directly observed. This frequency measurement is directly analogous to the improved precision one can make in a length measurement using two different length scales. Comparing Equations 4.5 - 4.7 for two different values of f_{rep} allows for the solution of n in terms of f_{beat}, f_{AOM}, $f_{rep,1}$, $f_{rep,2}$, f_0, and m. Assuming that the instabilities of these parameters are uncorrelated, the uncertainty of n (Δn) is given by

$$\Delta n = n\sqrt{\frac{2\left(\left(\Delta f_0\right)^2+\left(\Delta f_{beat}\right)^2+\left(\tfrac{1}{2}\cdot\Delta f_{AOM}\right)^2\right)+\left(m\cdot\Delta f_{rep}\right)^2}{\left(m\cdot f_{rep,2}\right)^2}+\frac{2\left(\Delta f_{rep}\right)^2}{\left(f_{rep,2}-f_{rep,1}\right)^2}} \qquad 4.9$$

where $f_{\mathrm{rep},1}$ and $f_{\mathrm{rep},2}$ are the initial and final repetition frequencies, respectively, and the Δf's indicate the uncertainty on each frequency. Typical uncertainties of the frequencies after averaging for 30 minutes are estimated by their standard deviations, and are: $\Delta f_0 \approx 1$ Hz, $\Delta f_{\mathrm{beat}} \approx 20$ kHz, $\Delta f_{\mathrm{AOM}} \approx 1$ kHz, and $\Delta f_{\mathrm{rep}} \approx 1$ mHz. To know n to the nearest integer ($\Delta n < 1$) in Equation 4.9, values of $m > 900$ would be necessary, but keeping the comb locked over such a large change is challenging and time-consuming. Therefore, measurements are made with $m \approx 10$ at two different values of f_{rep} separated by up to 200 kHz. Each measurement therefore had a $\Delta n \approx 40$ and f_{laser} was calculated for the two data sets for all possible values of n. When compared, 6 measurements agreed at a single value of f_{laser} to within 100 kHz. Thus the mode number of the nearest tooth was resolved. However, higher accuracy of ± 20 kHz was expected on the ~10 MHz wide feature in view of the ± 2 kHz accuracy achieved with a ~1 MHz wide sub-Doppler feature in PBCs [13, 14] and vapor cells [22].

Beat-note frequency shifts due to alignment

The cause of the 100 kHz inaccuracy was investigated because this value was roughly a factor of five larger than expected (due to a simple argument of the ratio of linewidths in this experiment to that of free-space measurements). The cause of the 100 kHz inaccuracy was discovered to be the laser alignment into the kagome fiber and the photodetector collection fiber as shown in Figure 4.8. When the pump or probe beam alignment into the kagome fiber was changed such that the power through the fiber was reduced by a factor of two, the frequency lock point of the acetylene-stabilized laser experienced ~100 kHz shifts. In contrast, no shifts were observed when the power was reduced by a factor of two while alignment was preserved. Similar changes in alignment into the PD fiber (middle right of Figure 3.4), which was initially single mode fiber (Corning SMF-28), demonstrated shifts on the order of 100's of kHz. The PD fiber was switched to multi-mode fiber (MMF), and the frequency dependence on the pump and probe alignment was found to be smaller by roughly a factor of two, while the frequency dependence of the coupling into the PD fiber remains on the order of 100 kHz. More importantly, the frequency shift became centered about the optimum alignment for peak power.

When the system's peak power was optimized through the kagome and PD fiber, the frequency of the lock point was repeatable to ±20 kHz. No shifts greater than 10 kHz were observed when servo polarity, FM phase polarity, and AM phase polarity were reversed.

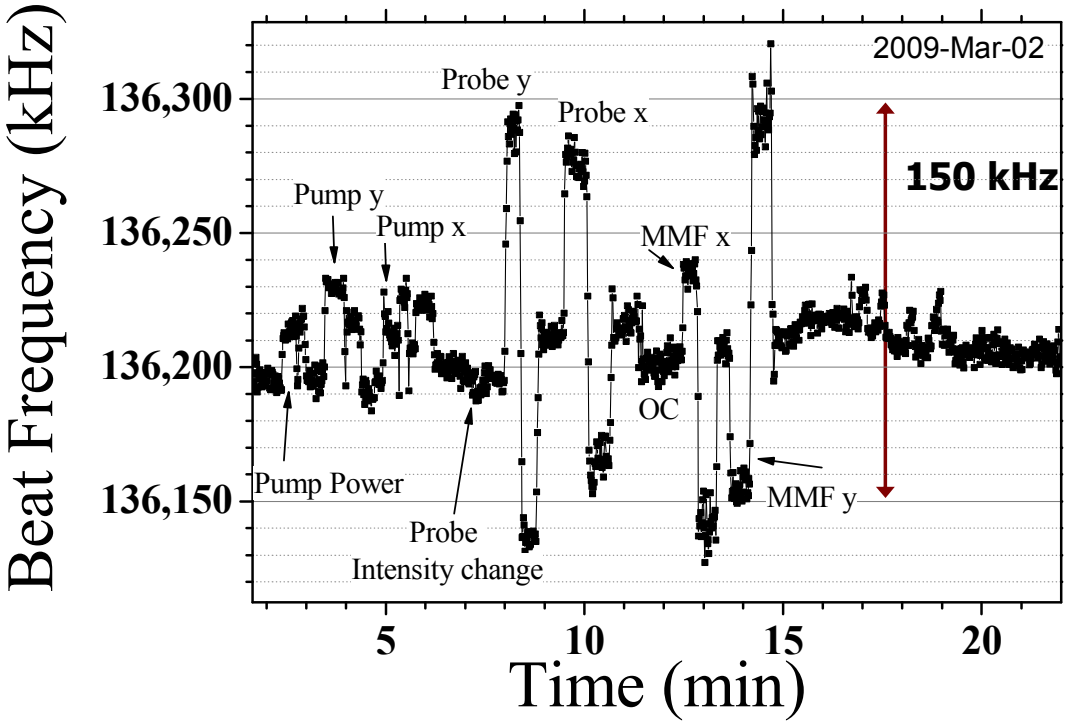

Figure 4.8 Frequency shifts of the cw reference due to pump and probe misalignment. The beat frequency between the CNFL comb and the cw reference is plotted vs. time, and the text on the graph indicates what parameters of the cw reference were changed to result in a change of the beat note frequency. x: horizontal mirror position; y: vertical mirror position; MMF: multimode PD fiber; OC: original coupling.

The dependence of the laser frequency on pump and probe alignment suggests that different spatial modes inside the kagome fiber experience different phase shifts. The alignment sensitivity is mitigated with the placement of a multi-mode fiber before the PD, suggesting that the multi-mode PD fiber collects more of the higher order modes simultaneously, allowing the various shifts from various modes to cancel more completely. It is reasonable that different spatial modes experience different shifts. Shifts in saturated absorption signals are known to arise from wave front curvature [35] and in angular beam deviations [37]. If one considers the pump (or probe) beam to be in the fundamental mode, and some of the power of the probe (or pump) beam to be in the next higher mode, then a series of crossings between the pump and

probe occur. The effective angle between the guided modes can be calculated from the difference in the propagation constant β, which in the case of kagome HC-PCF can be approximated to that of a capillary waveguide:

$$\beta_{nm} = k\left(1 - \left(\frac{u_{nm}}{k(d/2)}\right)^2\right) \tag{4.10}$$

In Equation 4.10, k is the wave vector amplitude and d is the fiber core diameter. The subscripts are the guided mode indices and u_{nm} is the m^{th} root of $J_{n-1}(u_{nm}) = 0$ [61]. During a misalignment, the coupled beam can partially "hop" from the fundamental mode HE_{11} to the first higher order mode set (TE_{01}+HE_{21}). The propagation mismatch between the two sets of modes is

$$\Delta\beta = \left(\lambda/\pi d^2\right)\left(u_{11}^2 - u_{21}^2\right) = 2.8\left(\lambda/d^2\right) \tag{4.11}$$

From a simple ray picture the phase mismatch between these modes corresponds to a mismatch of their wave fronts of

$$\Delta\theta = \left(\lambda/\pi d\right)\left(u_{11} - u_{21}\right) = 0.45\left(\lambda/d\right)\mathrm{rad} \tag{4.12}$$

If the beams were to cross in free-space at this angle at one end of an absorption cell, a frequency shift of

$$\Delta f = (v_{\mathrm{thermal}}/\lambda)\sin(\theta/2) = 2\,\mathrm{MHz} \tag{4.13}$$

would be observed [37]. We postulate that many crossings occur in the kagome fiber, causing the shifts to generally cancel out. Additionally, the pump and probe beams are likely to be exciting different distributions of higher order modes, which could account for these residual shifts. In a fused, vibrationally isolated photonic crystal fiber cell (i.e. a gas-filled HC-PCF

spliced to a conventional optical fiber) [62], such random shifts are likely to be reduced, although a permanent shift may result.

Determination of the cw reference's absolute frequency

To fully characterize the gas-filled fiber frequency accuracy, a series of measurements were made under a variety of acetylene pressures. The beat between the stabilized cw laser and the convenient CNFL comb was counted for over 1000 s at 1 s gate time and averaged. The absolute frequency of the acetylene-stabilized laser (f_{laser}) was already measured to within 100 kHz with the Cr:f laser, which allowed for the determination of n (which by definition is an integer) in subsequent measurements from Equations 4.5 - 4.7. Figure 4.9 plots the frequency of the reference with the AOM shift removed (f_x) versus acetylene pressure inside the kagome fiber, and each data point indicates an independent realignment of the SAS setup. A linear fit through these data gives a zero-pressure intercept of (195,580,979,379.6 ± 5.6) kHz with a slope of (-369 ± 48) kHz/torr. Both of the listed errors are statistical (or Type A) uncertainty.

Systematic shifts and uncertainties in the absolute frequency arise due to residual gas pressure, fiber alignment, pump power, and attenuation in the fiber (all of these parameters are considered Type B, or non-statistical, uncertainty). The residual pressure in the chamber was ~20 mtorr, which implies a 7.4 kHz uncertainty using the measured pressure shift of -369 kHz/torr. This pressure shift has an error of ± 61 kHz/torr when a 10% pressure calibration error is included, and is near the value of (-270 ± 30) kHz/torr (2 σ error) recorded at pressures of ~50 torr in Ref. [12]. Alignment shifts were also considered, and were effectively transformed into statistical error by repeated alignment of the system. A frequency shift of -1.6 kHz was calculated by multiplying a previously reported power shift of -11.4 Hz/mW [20] by 144 mW of average pump power, accounting for attenuation down the length of the fiber.

The P(13) frequency measured in this work is listed alongside an error budget in Table 4.1 with values from Ref.s [13, 14]. It should be noted that the total error bar on this measurement is within an order of magnitude of those from similar experiments using SAS in power build-up cavities and vapor cells with ~1 MHz FWHM sub-Doppler features [13-15, 20-22, 63]. The measured value, when corrected for pressure and power shifts, is (195,580,979,378.0 ± 9.3) kHz, which agrees with previously measured values within the uncertainty. From this agreement, we conclude that shifts caused by molecules colliding with the fiber core walls are below the 10 kHz

level. Thus the gas-filled kagome fiber is a suitable medium for portable precision spectroscopy, potentially increasing the current calibration standard by four orders of magnitude.

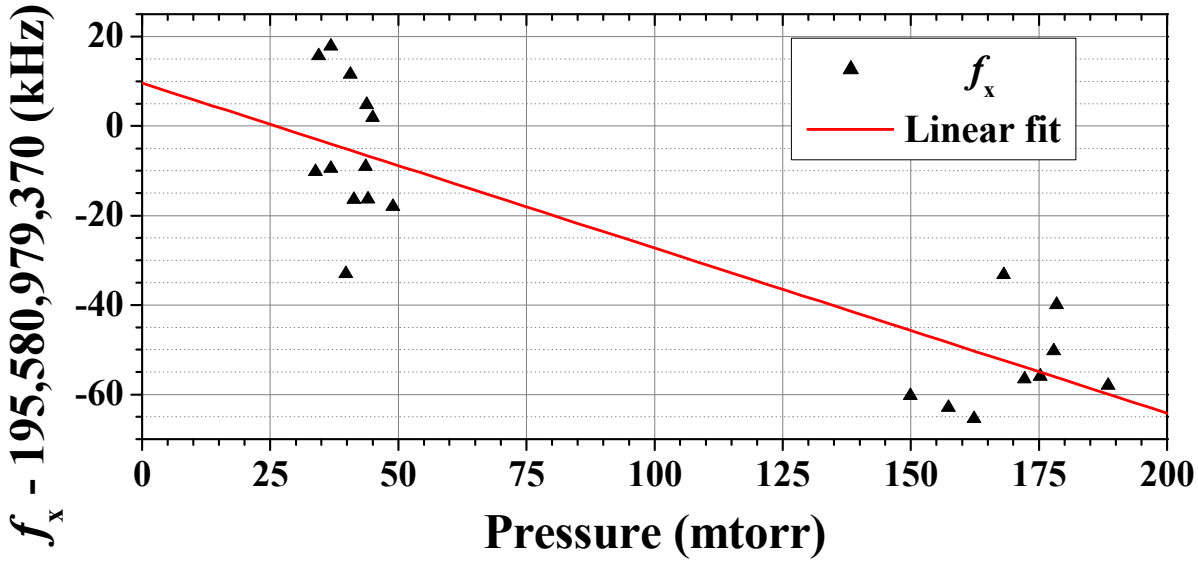

Figure 4.9 Absolute frequency of the acetylene-stabilized laser versus acetylene pressure inside the 4.1 m kagome fiber with a linear fit line. Each data point indicates an independent alignment to avoid frequency offsets due to free-space coupling into the kagome fiber. The linear fit gives a zero-pressure intercept of (195,580,979,379.6 ± 5.6) kHz and a slope of (-369 ± 48) kHz/torr.

Table 4.1. Mean $^{12}C_2H_2$ $\nu_1+\nu_3$ P(13) frequency and error budget for this work and for referenced work [13, 14].

	Uncertainty (kHz)				Mean P(13) value (kHz)
	Statistical†	Pressure‡	Power‡	Total	
This work	5.6	7.4	0.6	9.3	195,580,979,378.0
Ref. [14]*	-	-	-	3.7	195,580,979,370.4
Ref. [13]	2.0	10.0	-	10.2	195,580,979,371.1

† Type A uncertainty

‡ Type B uncertainty

* individual uncertainties were not listed for the P(13) line

Stability measurements

The precision of a frequency reference's oscillation as a function of averaging time is the most common parameter used to describe its stability. Ideally, as the averaging time of the oscillation frequency is increased, the measurements should become more precise. On a long enough time scale, however, all frequency references experience degradation in their precision due to various noise processes. Due to the ease of use and long stabilization times achievable with the CNFL frequency comb, most stability measurements of the cw reference were conducted with this comb. The setup for this measurement is the same as the absolute frequency measurement (Figure 4.7a), and an example of the counted beat note frequency is included in Figure 4.10a.

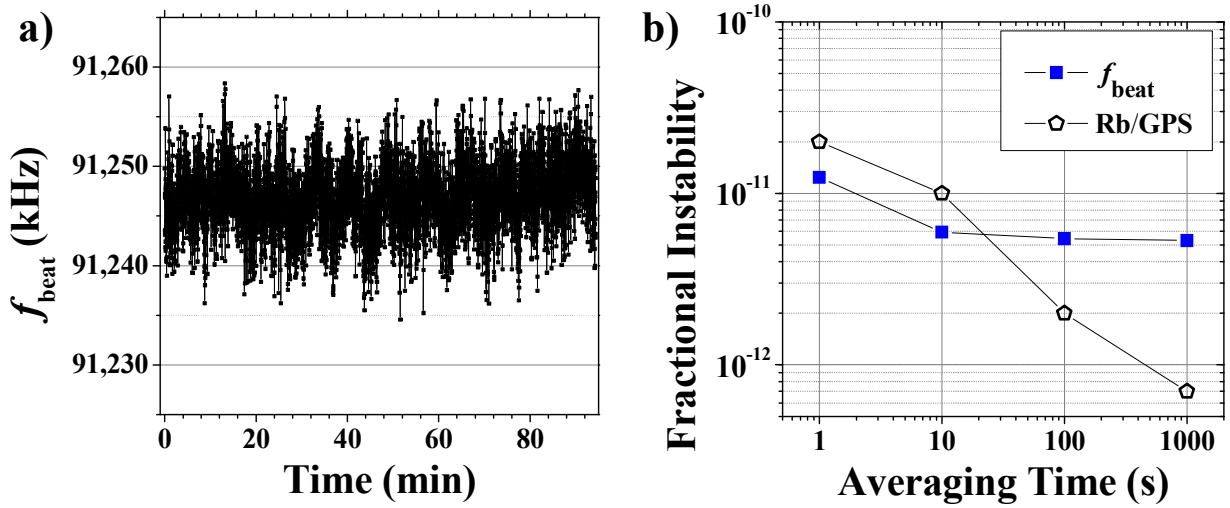

Figure 4.10 a) Frequency of the beat between the HC-PCF acetylene-stabilized laser and the CNFL frequency comb vs. time, recorded at a 1 s gate time using a counter. Oscillations with a period of ~10 minutes correlate to air-conditioner cooling cycles. b) Optical fractional frequency instability vs. averaging time for f_{beat} (filled squares) and the GPS disciplined Rb oscillator (open pentagons). A triangle deviation, similar to an Allan deviation, was calculated for f_{beat}.

At 1500 nm, the dominant source of instability in the CNFL comb is due to the Rb/GPS instability being transferred to f_{rep}. Equation 4.1 was used to calculate the triangle deviation, an estimate of the Allan deviation that is distorted by the interpolation of our frequency counters [64]. The counters experience a small amount of dead time between consecutive counts, making the recorded data not truly consecutive. However, this dead time is typically on the order of 40 ms, and when counting at averaging times of 1 s or greater, the difference between the

triangle deviation and the Allan deviation is negligible. Fractional frequency instabilities were calculated for f_{beat} (σ_{beat}) and f_{rep} (σ_{rep}) in the optical domain to determine the heterodyne instability and the comb's in-loop instability. Because of the limitations of in-loop measurements, the Rb/GPS instability (pentagons) was plotted alongside the beat frequency instability (squares) in Figure 4.10b. The instabilities given by the Rb/GPS manual are typical values, and have not been measured for the particular unit used in this experiment. The CNFL comb's instability is limited by the Rb/GPS reference, and therefore dominates the beat frequency's instability at short gate times. The beat sets an upper limit on the instability of the HC-PCF acetylene-stabilized laser, which is within an order of magnitude of other acetylene-based frequency references in power build-up cavities and gas cells at 1 s averaging times (shown in Figure 4.11) [14, 15, 22]. The higher instability is attributed to the broader sub-Doppler linewidths observed in HC-PCF (~8 MHz) relative to the linewidths of free-space configurations used in the previously mentioned experiments (~1 MHz). Also, deviations from the expected $\tau^{-½}$ behavior (for $\tau > 10$ s) that occur in this work are attributed to the air-conditioner cycles, and are seen in Figure 4.10a as oscillations that occur every 15 minutes. The correlated behavior between the room temperature and the beat note frequency was investigated, but a direct dependence was never determined. It is possible that thermal effects on the fiber could be responsible for this shift (changing the waveguide slightly and therefore shifting the relative population of modes described early in this chapter concerning the alignment sensitivity).

The optimum potential relative instability of this reference can be estimated from the equation

$$\sigma_{y,opt}(\tau) = \frac{w_l}{f_{C_2H_2} \cdot \mathrm{SNR} \cdot (BW)\tau^{1/2}} \qquad 4.14$$

where BW is the bandwidth of the low-pass filter right before the servo electronics. This equation is taken from Ref. [65] (which presents it as a simple estimate for the optimum stability of atomic clocks) and modified slightly to account for bandwidth of the detection electronics and averaging time. Values of $w_l = 8\,\mathrm{MHz}$, $f_{C_2H_2} = 195\,\mathrm{THz}$, $\mathrm{SNR} = 100$, and $BW = 60\,\mathrm{kHz}$ were used to obtain a fractional instability of 1.7×10^{-12} at 1 s when the 125 MHz photodetector was

implemented in the cw reference. Higher SNR values of 600 could be obtained by switching to the 1 GHz photodetector and result in a fractional instability of 2.8×10^{-12} at 1 s. This is significantly below the measured instability at 1 s, indicating that a better optical reference is necessary to properly characterize the cw reference at short times. A second cw reference is currently being fabricated and assembled to facilitate this measurement.

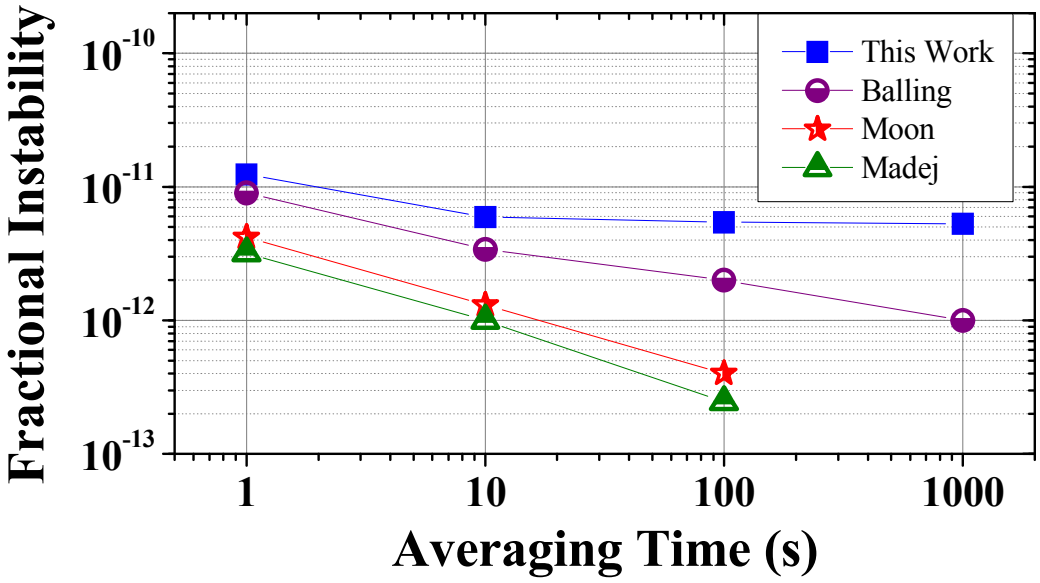

Figure 4.11 Fractional instability versus averaging time for this work (using kagome HC-PCF) and other references based on free-space saturated absorption spectroscopy of acetylene setups. The names listed in the legend correspond to the following references: Balling [22], Moon [15], and Madej [14].

Investigation of stability and beat note shifts at low optical powers and reduced temperatures

Techniques were investigated which lead to a reduction in the observable linewidth with an aim towards improving the stability of frequency references inside kagome HC-PCF. The limited interaction time between molecules and the laser field, imposed by the size of the core diameter, sets the minimum observable linewidth in HC-PCF. In the largest core HC-PCFs available, the observable linewidths are an order of magnitude larger than those in free-space power buildup cavities. The linewidth broadening that the fiber inherently induces in this experiment sets a fundamental limit on our ability to stabilize a laser's frequency for use as an optical reference. Additionally, reducing the alignment sensitivity of the pump and probe beams

into the fiber (simply by reducing the linewidth) would be of great benefit to the reference's accuracy.

Initial experiments of saturated absorption spectroscopy involved using free-space laser beams, and observed linewidths were generally limited by the molecular transit-time in the laser field which was set by the beam size [66]. Using a perturbation method to calculate the line shapes in this experiment, Ref. [34] found that linewidths below the transit-time limit could be observed. The reasoning for this lies in the fundamental setup of this experiment. The observed sub-Doppler signal is created through contributions of molecules that all have no velocity component down the length of the fiber. This, however, still allows for molecules to have a variety of transverse speeds. If the optical pump power is reduced sufficiently below the saturation power, a case can be realized where the fastest molecules will be unlikely to absorb a pump photon before colliding with the core walls. This causes an effective attenuation of the fast molecules' contribution to the saturated absorption signal, leaving an observable linewidth that is narrower than the transit-time limit. In addition to working at low optical pump powers, low pressures are necessary so that the system is dominated by transit-time broadening and not intermolecular collisions. These finding were investigated by Hald, et.al. in Ref. [67] to observe linewidth reduction in 10 μm PBGF, though no efforts to the author's knowledge have been made to investigate this effect in other HC-PCF.

Although reduced linewidths have been observed in molecular systems, there have not been any published results to the author's knowledge on using this narrower line to improve the stabilization of a laser. A consideration of the sub-Doppler feature's linewidth and depth (or D from Equation 2.15) is appropriate to determine if this method will be feasible to use in laser frequency stabilization. When the optical power is much lower than the saturation power (or the weak-field approximation given in Ref. [23] as Equation 7.29a), the saturated absorption signal has an absorbance given by

$$\alpha L = A_g e^{-2\left(\frac{f-f_{C_2H_2}}{w_g}\right)^2} \cdot \left(1-\frac{1}{2}\frac{P}{P_{sat}}\left(1+\frac{w_l^2}{4\left(f-f_{C_2H_2}-\frac{1}{2}f_{\mathrm{AOM}}\right)^2+w_l^2}\right)\right). \qquad 4.15$$

When the frequency is centered on the Lorentzian component, this equation becomes (to good approximation)

$$\alpha L_{sub-D} = A_g \cdot \left(1 - \frac{P}{P_{sat}}\right) \tag{4.16}$$

where αL_{sub-D} is the peak value of the reduced absorption. The contrast in this situation can be calculated from Equations 2.16 and 4.16:

$$C = e^{-A_g\left(1-\frac{P}{P_{sat}}\right)} - e^{-A_g}. \tag{4.17}$$

Because the pressure will necessarily need to be low, A_g will be small, and a Taylor expansion of the exponents about zero in Equation 4.17 leads to

$$C = A_g \frac{P}{P_{sat}}. \tag{4.18}$$

The amount of power broadening in the linewidths for this experiment will be negligible, resulting in a discrimination of

$$D = \frac{A_g P}{P_{sat} \cdot w_l^2}. \tag{4.19}$$

Here, D can be used to observe trends in the SNR, and is clearly a function of both power and pressure (from Equation 2.3). Because the pump power must be reduced by over a factor of 100 to get down to the necessary level to see linewidth reduction, the linewidth must decrease by at least a factor of 10 to maintain the same SNR at high powers. Reductions by a factor of 3 were observed in Ref. [67] over roughly this same range, which indicates that there may be no advantage to employing this technique, as the stability of the locked cw laser might be degraded more by the reduction in sub-Doppler height than it is improved by the reduction in linewidth.

Experimental observation of linewidth reduction through slow molecule selection

Experimentally, it was quite straight-forward to see a linewidth reduction by reducing the pump power. Because the sub-Doppler feature was quite small at both low pressure and low pump powers, frequency modulation spectroscopy was implemented (detailed in Figure 3.4) to both increase the observable SNR and to produce a suitable feature for laser-locking. In this particular setup, the probe beam was less than or equal to 200 μW (the probe power was set equal to the pump power in the case when the pump power was below 200 μW). The pump beam was set to different powers by the combination of waveplate adjustments before the polarization beam splitter and insertion of neutral density filters into the beam path before entering the kagome PCF.

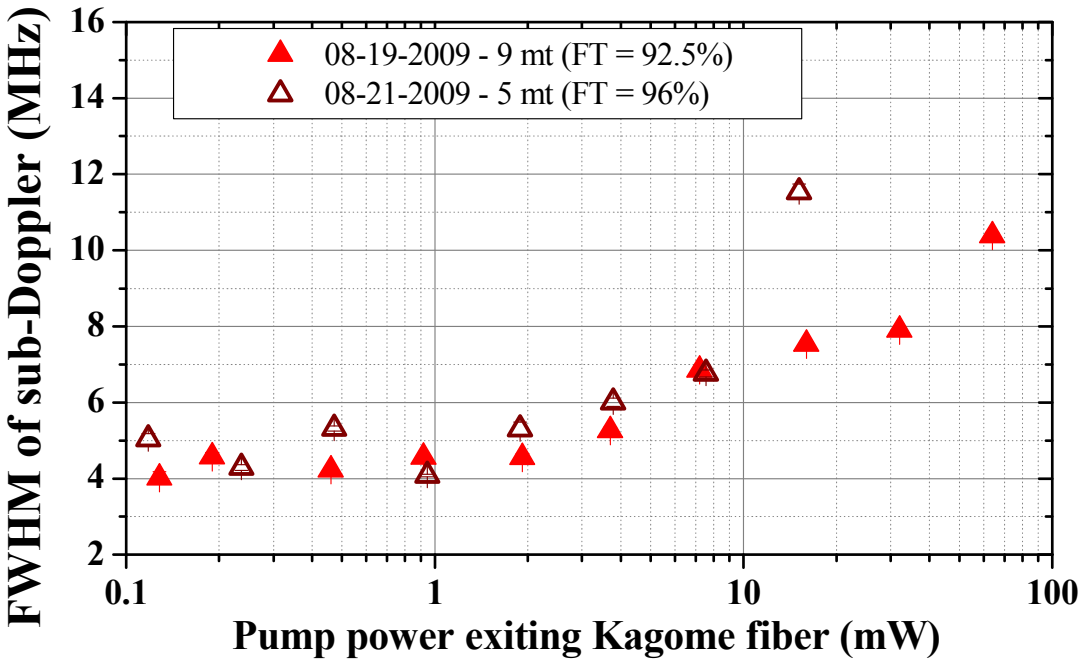

Figure 4.12 FWHM of sub-Doppler feature versus pump power exiting the 4.1 m kagome HC-PCF. FM spectroscopy dispersion signals were recorded and fit according to Equation 3.15. It is unclear why the 5 mtorr, ~15 mW data point exhibits a larger than expected linewidth, though lack of optimization of either the FM or AM electronic phase could easily account for this. Data was recorded and analyzed with the help of Shun Wu and Chenchen Wang.

The resulting reduction in observed linewidths is shown in Figure 4.12 for two different fiber pressures. There appears to be a factor of two reduction in the linewidths (from 8 to 4 MHz) when comparing data taken at low power and near or above the saturation power (34 mW for kagome HC-PCF in this work or 23 mW as reported in Ref. [39]). This is a smaller

amount of narrowing than the factor of 3 the authors in Ref. [67] found when investigating this effect on 10 μm core PCF (from 44 to 15 MHz). One possible reason for this could be that the authors of Ref. [67] used longer PBGF (close to 10 m) which caused the FT of their system to be close to 50% for a fiber pressure of 23 mtorr. Remembering from Chapter 2 that $A_g = (\alpha L)_{\max} = -\ln(FT)\big|_{f=f_{C_2H_2}}$, working with longer fibers decreases the FT on resonance, which in turn increases A_g. Because kagome HC-PCF is only attainable through our collaborators at the University of Bath, investigation of this effect in a longer fiber has not yet been possible. Additionally, the residual pressure in the fiber could broaden the minimum observable linewidth due to the vacuum setup of this experiment.

The SNR of the FM dispersion signal was measured and is plotted in Figure 4.13. At low pump powers, the SNR is nearly linear as a function of pressure. Observing that the linewidths do not show any noticeable reduction below 2 mW of pump power in Figure 4.12, Equation 4.19 predicts this functionality. This reduction in SNR is detrimental to the stability of the cw reference, as can be observed in the optimum calculation given in Equation 4.14.

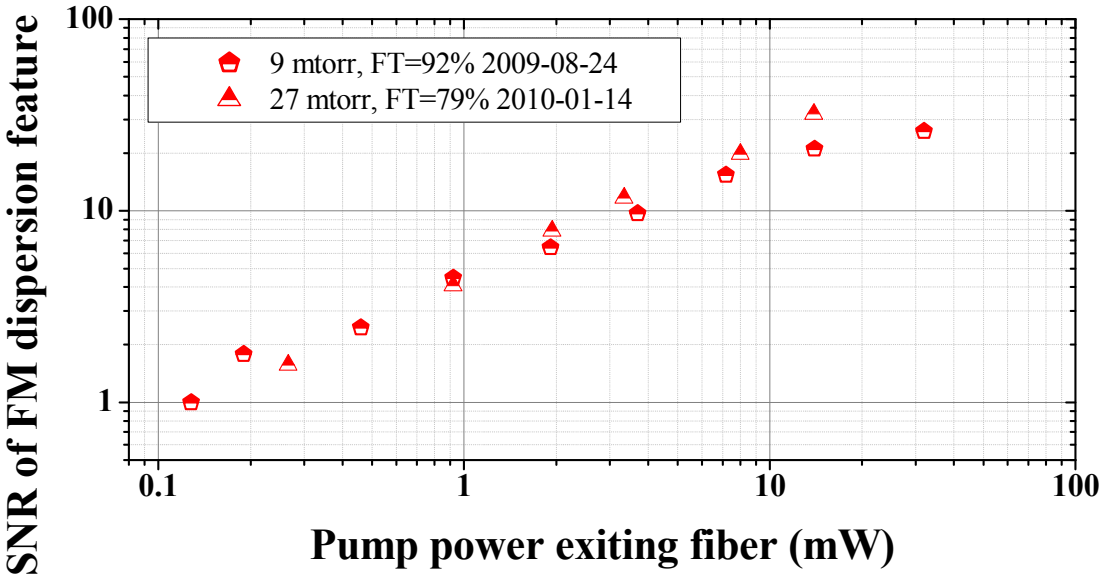

Figure 4.13 SNR of the FM dispersion signal versus pump power exiting the fiber. Data recorded with the help of Shun Wu and Chenchen Wang.

Efforts were next enacted to test the stability of the cw reference under the conditions of low fiber pressure and low optical pump power. First, the stability was measured with high

pump power at two different fiber pressures to determine if a decrease in the SNR would degrade the stability. This was indeed the case, and is shown in Figure 4.14a. Figure 4.14b shows a similar trend when instead of the fiber pressure the optical pump power is reduced. At longer gate times there is good agreement between the ratio of the SNR's (found in Figure 4.13) and the ratio of the fractional instabilities. Additional data were recorded to determine the repeatability of this trend, and it was found that decreases in the SNR appear as increases in the fractional instability.

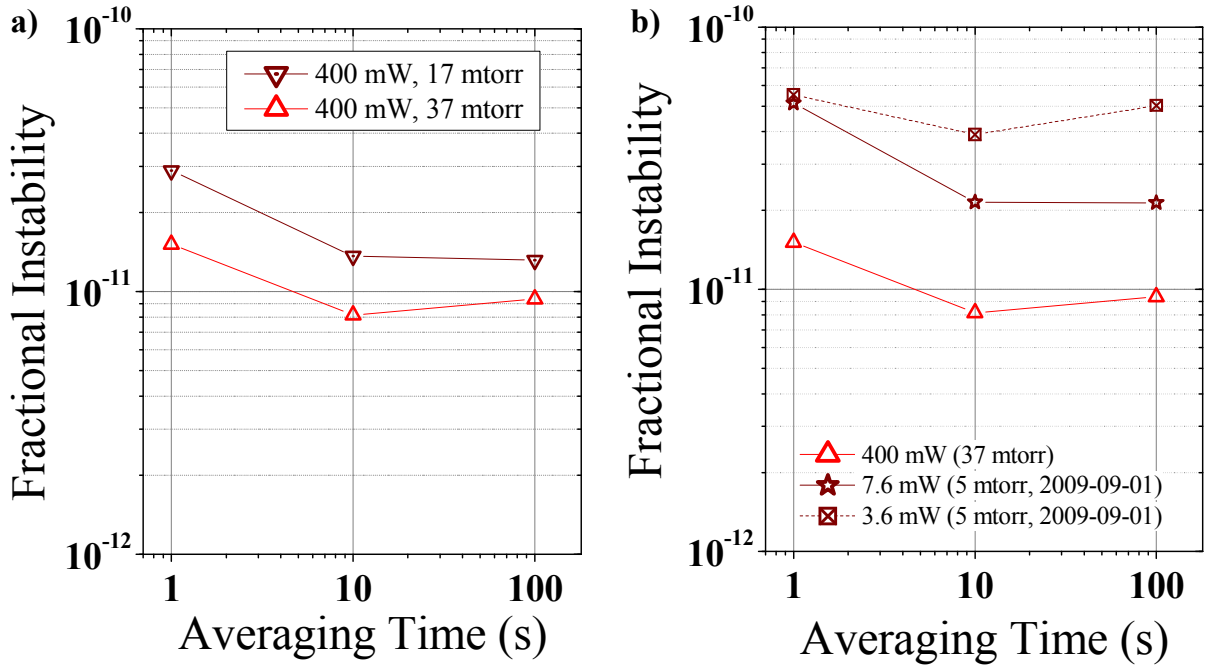

Figure 4.14 a) Fractional instability of the beat note for two different internal fiber pressures of the cw reference vs. averaging time. The legend indicates the optical pump power and the internal fiber pressure. The observed ratio of the 37 mtorr SNR to the 17 mtorr SNR was 1.7, while the average ratio of the fractional instability of the 17 mtorr data to the 37 mtorr data was 1.8. b) Fractional instability for two different (low) optical pump powers of the cw reference versus averaging time. The high power instability data is included as a reference.

Molecular temperature reduction to increase the SNR

One idea to try and increase the SNR at low optical powers was to reduce the temperature of the HC-PCF. This would reduce the molecules average speed according to Equation 2.13. This reduction in temperature should affect the Gaussian component of the absorption line by narrowing the observed width and decreasing the FT on resonance. Also, since the sub-Doppler

feature is limited by transit-time broadening, one might expect to see a narrowing of the linewidth due to a reduced temperature. However, it is likely the case that even at powers that are close to the saturation power, some portion of the fast molecules are not able to saturate before colliding with the fiber core wall. Reducing the temperature may have a minimal effect on the sub-Doppler feature in this case.

A thermal isolation box with a lid was constructed so that a majority of the length of the fiber could be placed inside and cooled. Cooling the reservoir of gas is not feasible in the current setup, as the vacuum chambers are rather large and contain rubber gaskets. This thermal box was made out of rigid polystyrene, and has a reservoir chamber adjacent to the fiber compartment so that a temperature bath could be loaded without pouring the liquid directly on the fiber (see Figure 4.15). Approximately ~20 cm on each end of the fiber is unavailable for cooling due to the vacuum chambers.

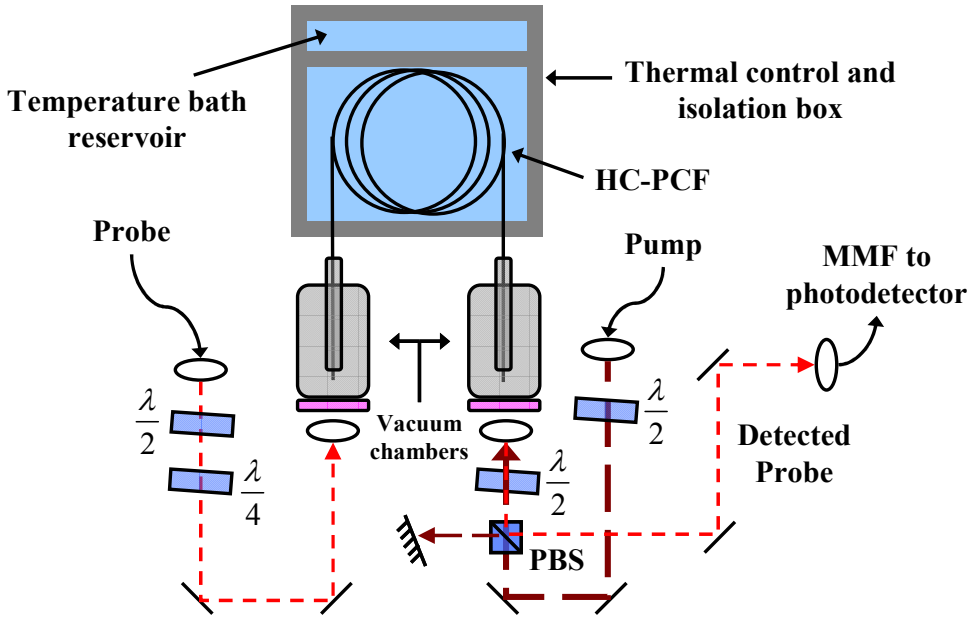

Figure 4.15 Physical layout (top view) of the cw reference with the thermal control and isolation box. The thermal box has a separate reservoir (with holes drilled at the bottom to connect) so that a temperature bath can be loaded without directly pouring it on the HC-PCF. This is the same layout as detailed in Figure 3.4.

Acetylene has a long sublimation range and, for the pressure range of interest, a sublimation point near 105 K for 10 mtorr of vapor pressure is shown in Figure 4.16. Initial experiments were therefore done with a dry ice (solid CO_2) and ethanol bath to make sure the fiber could withstand substantial changes in temperature. The sublimation point of CO_2 is 195

K, and the presence of ethanol does not change this noticeably. However, the bath temperature was measured to be 235 K, which may be due to a small amount of the polystyrene box dissolving in the mixture [68]. The ratio between room temperature and the dry ice bath is rather modest, and while a slight reduction in the Doppler height and width was observed, no change in the sub-Doppler feature's width was seen. Further attempts to lower the temperature were achieved by Chenchen Wang using liquid nitrogen and a heating plate with a temperature servo controller. Temperatures below ~165 K appeared to condense the acetylene and caused the absorption to disappear. The most likely cause of this higher vapor pressure is the presence of acetone vapor, as commercially available acetylene comes dissolved in acetone for safety reasons (acetylene will decompose explosively when stored in its pure form at pressures of 1 atm or greater).

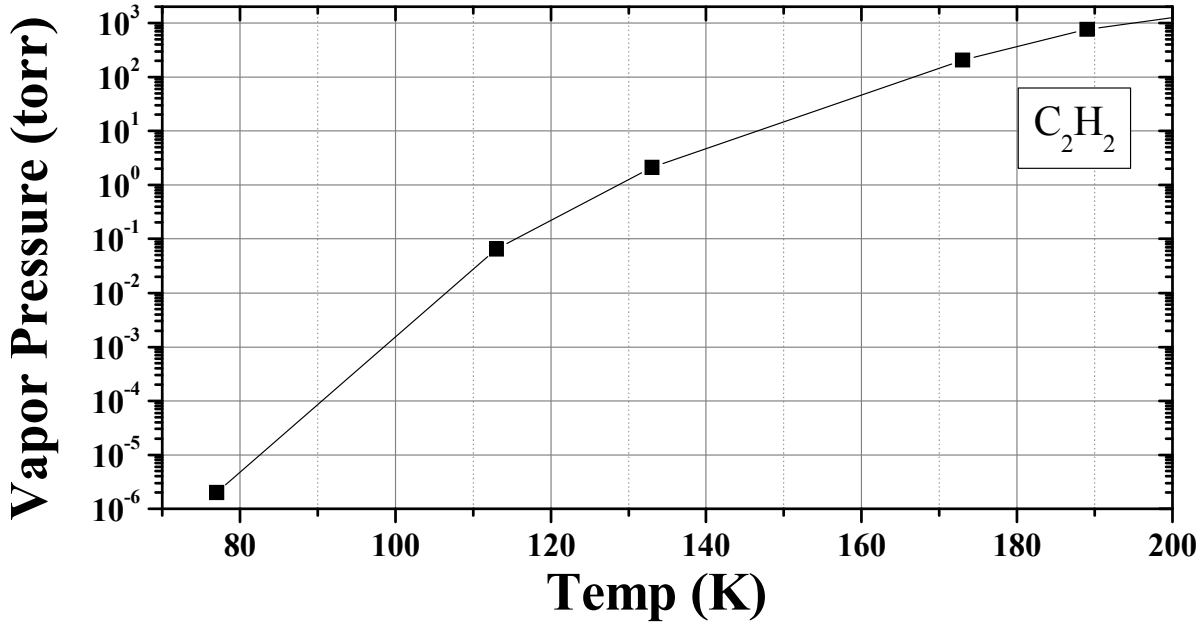

Figure 4.16 Acetylene's vapor pressure vs. temperature. Data points taken from Ref. [69].

Saturated absorption and FM spectra were recorded when the fiber was cooled to ~175 K. The Doppler width depends on the square root of temperature (as it linearly depends on the average molecular velocity), and one can calculate the ("*cold*") temperature of the molecules from the following equation:

$$\frac{w_{G,cold}}{w_{G,hot}} = \sqrt{\frac{T_{cold}}{T_{hot}}} \tag{4.20}$$

where the "*hot*" subscripts indicate room temperature. Similarly, the amplitude of the absorption coefficient can be used to calculate the temperature of the molecules since it depends linearly on the number of molecules present. Using the ideal gas law, and because the fiber ends are effectively connected to infinite reservoirs, the number of molecules are inversely proportional to the temperature. This leads to the relation

$$\frac{A_{G,cold}}{A_{G,hot}} = \frac{\ln\left(FT_{cold}\right)}{\ln\left(FT_{hot}\right)} = \frac{T_{hot}}{T_{cold}} \tag{4.21}$$

A temperature sensor was placed in the thermal box, and after temperature stabilization was achieved, a value of 175 K was measured. The Gaussian parameters were also recorded, and using Equations 4.20 and 4.21 yielded average temperatures of 186 K and 168 K (special thanks to Chenchen Wang for the considerable time she spent setting up the temperature stabilization system). The measured FWHM of the sub-Doppler feature, however, was found to be independent of temperature, even at higher optical powers (shown in Figure 4.17). The conclusion drawn from this is that the transit-time effect must already "filter out" the faster moving molecules at room temperature. When the temperature is reduced, the average molecular speed is reduced, but there are now more molecules available to be saturated.

Inspection of these sub-Doppler signals revealed an increase in the SNR by almost a factor of two (as expected from Equations 4.19 and 4.21) and is shown in Figure 4.18. This is a direct result of increasing the absorption by the inverse of the ratio of the temperatures (295/175 = 1.7). Although cooling the acetylene does give rise to higher SNR's, this modest increase will not alleviate the increased instability present in a reference operating under these parameters.

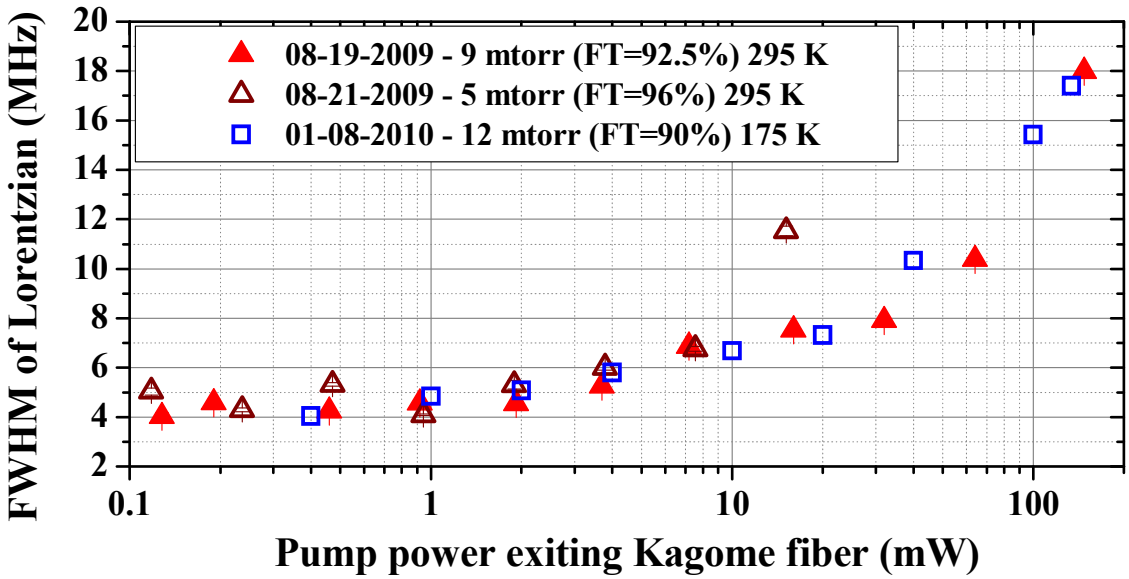

Figure 4.17 FWHM of dispersion feature at 175 K vs. pump power exiting Kagome PCF. Data from Figure 4.12 were included for reference.

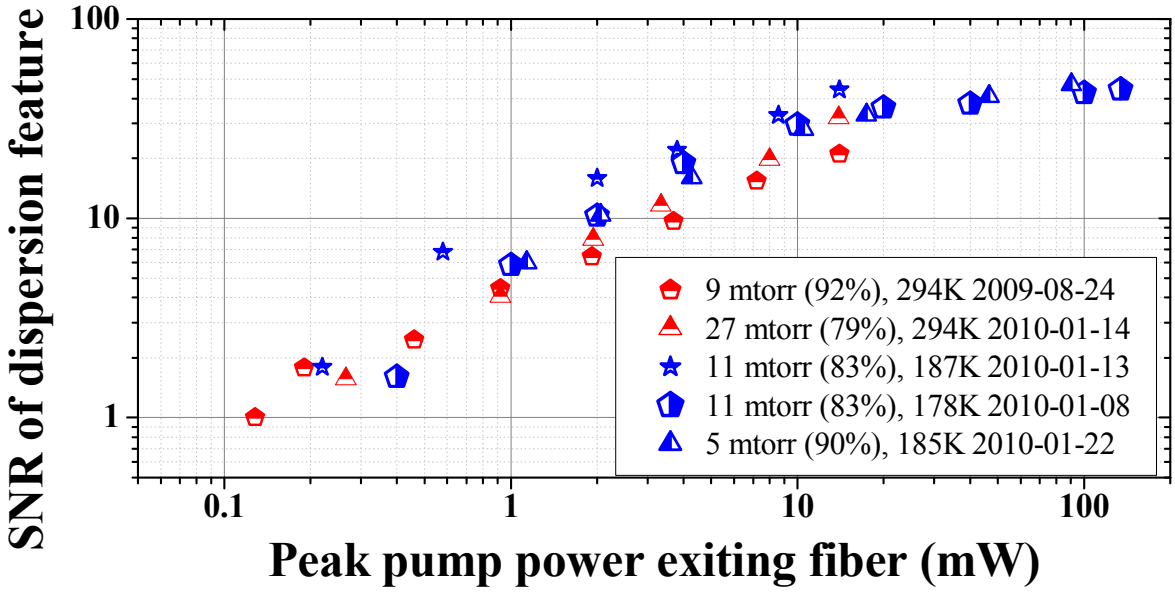

Figure 4.18 S/N ratio of sub-Doppler dispersion feature vs. pump power exiting the kagome PCF. Blue symbols indicate "cold" data near 180 K, while red symbols indicate data taken near room temperature (~295 K). The "cold" data is nearly a factor of two larger than the room temperature data.

The fractional instability was investigated, and the previously reported trend between SNR and fractional instability was again verified. The ratio of the SNR's (cold to hot) was 1.7, while the ratio of the fractional instabilities (hot to cold) was 1.8, again showing good agreement.

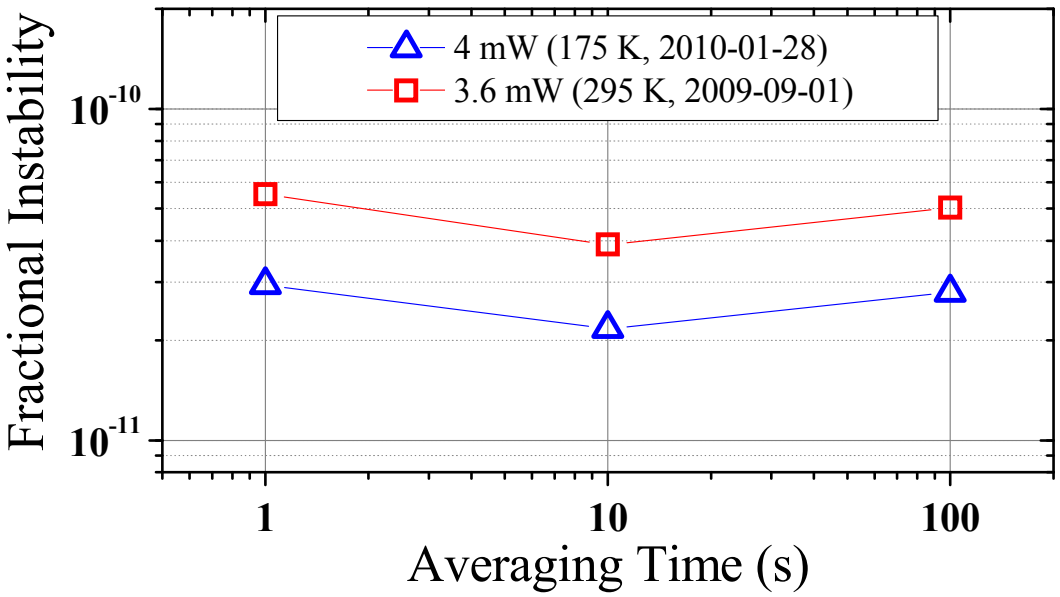

Figure 4.19 Fractional instability of the acetylene reference at 175 K (blue triangles) and 295 K (red squares) versus averaging time. The optical pump powers for the two measurements are listed in the legend. The ratio between the 295 K and 175 K fractional instabilities was 1.8, while the ratio of the 175 K to the 295 K SNR was 1.7.

While slow molecule selection did allow observation of linewidths below the transit-time limit, the reduction in SNR was too detrimental to make this technique useful in the current cw reference. Temperature reduction could be employed to improve the SNR, though incorporation of a temperature control system in a portable setup would not be worthwhile due to the small SNR increase that is observed. Investigation of the alignment sensitivity at low pump powers is still necessary to completely exhaust this area of research, though it is doubtful that meaningful measurements can be made with the degraded fractional stability.

CHAPTER 5 - Development of portable frequency references

The work presented thus far has considered the optimal capabilities HC-PCF offers to the field of optical frequency references. To fully realize the portable nature of HC-PCF, molecular gases must be trapped at low pressure (10^{-4} atm) inside the fiber, while maintaining the capability of coupling light into and out of the fiber with low loss. This requires melting solid core fiber to both ends of the HC-PCF (shown in Figure 5.1) while preventing contaminants from entering the cell. Sealing the second end of the HC-PCF while maintaining these conditions has proven to be rather difficult, and this chapter discusses the tools, techniques, and results encountered in this project.

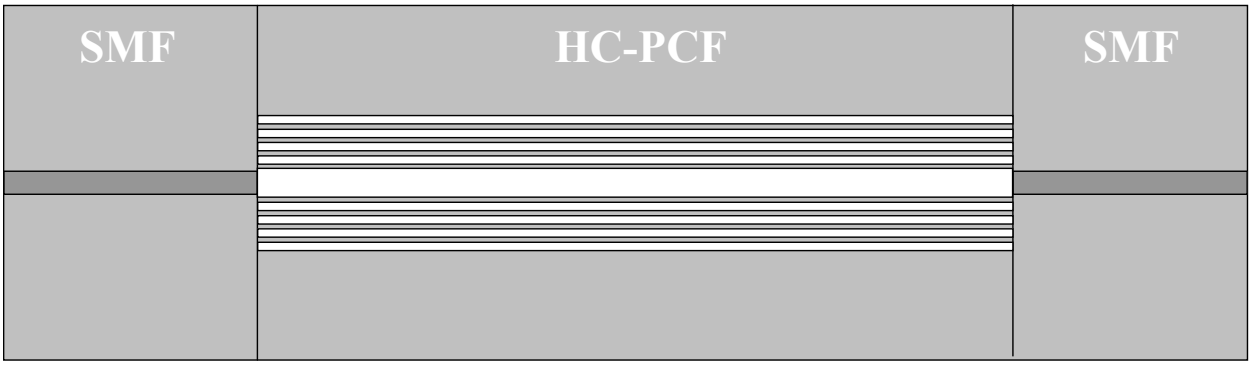

Figure 5.1 Fiber cell schematic. Detailed cross sections of the fibers can be seen in Figure 1.5. SMF is fused to both ends of the HC-PCF, with the intention of trapping a low-pressure molecular gas inside.

Fiber fusion splicers

Heating two fibers such that they melt together can be achieved through a few different types of lab equipment called fiber fusion splicers. Conventional fiber fusion splicers are made to operate in air, as their original purpose was to connect or repair solid core fibers in telecommunication networks. The most common type of splicer is an electric arc splicer (Figure 5.2a), which specifically relies on the presence of oxygen to make an arc. Another common splicer is the filament splicer (Figure 5.2b), and depends on the black body radiation emitted from the filament. Typically filament splicers use a purge the splicing region with an inert gas (such as argon) to lengthen the life of the tungsten filament (similar to incandescent light bulbs).

The last type of splicer in occasional use relies on CO_2 laser light whose wavelength also coincides with an appreciable absorption band of silica (Figure 5.2c). These laser splicers have the advantage of working in either vacuum or air, but are not commercially available. Our laboratory has developed a homemade setup to create low pressure fiber cells. The initial aim of this system was to be able to make the second splice while under vacuum to reduce molecular contamination.

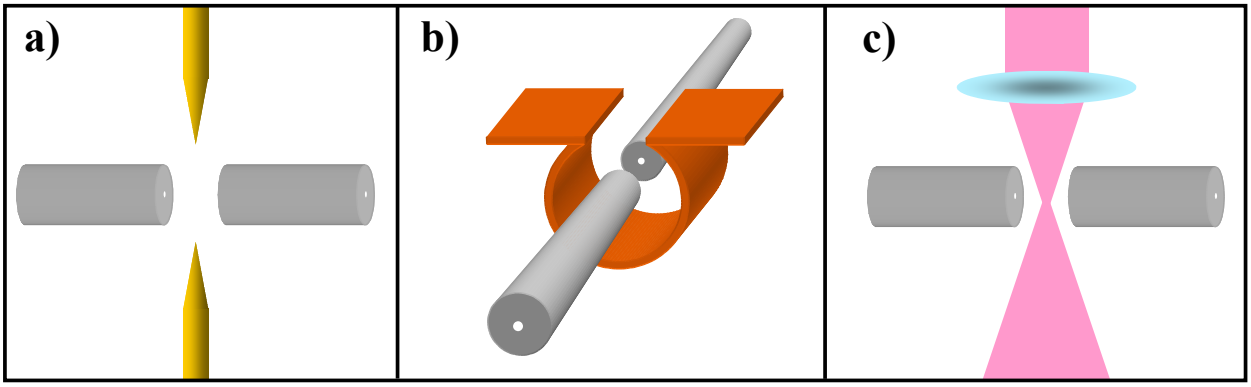

Figure 5.2 Basic schematics for various splicing schemes. a) Electric arc fusion splicer schematic. Fibers are fused by bringing them near a set of electrodes (shown in gold), after which a high voltage is applied to produce an electric arc. b) Filament fusion splicer schematic. Fibers are fused by radiative heating from a filament (typically tungsten). c) CO_2 laser splicing schematic. CO_2 laser light is focused onto fibers by means of a lens.

Verification of saturated absorption signals after splicing SMF to HC-PCF

Photonic crystal fiber is inherently more fragile than SMF due to the large amount of air found in the cladding region. Despite this fact, it was reported by Dr. Fetah Benabid's group that cleaving and splicing HC-PCF to SMF could be achieved with relatively low loss in the first experiment involving a high-pressure, hydrogen-filled fiber cell (~80 bar) [62]. Dr. Benabid's group also discovered a method to create the first low pressure gas cell by leaving the HC-PCF under vacuum and using a splicer to taper the fiber end to seal it [70]. This tapered end was then spliced to SMF and resulted in a rather large optical loss of 10 dB. This was not a problem for the electromagnetically-induced transparency signals they were investigating in acetylene, and although they did record a saturated absorption trace, the signal to noise ratio is hard to discern.

In an effort to replicate this splicing result in Ref. [62], a colleague in Dr. Corwin's laboratory, Dr. Rajesh Thapa, discovered a very easy and repeatable method using an arc splicer to fuse 10 and 20 μm HC-PCF with SMF [71]. Upon investigating the quality of these splices

under vacuum in a saturated absorption spectroscopy setup (Figure 5.3), it was discovered that the Fresnel reflection from the splice's glass-air interface was sufficient to act as a probe beam. This discovery comes as no surprise in retrospect, as using pump reflections to observe sub-Doppler linewidths are the basis for power buildup cavities [13-15, 17].

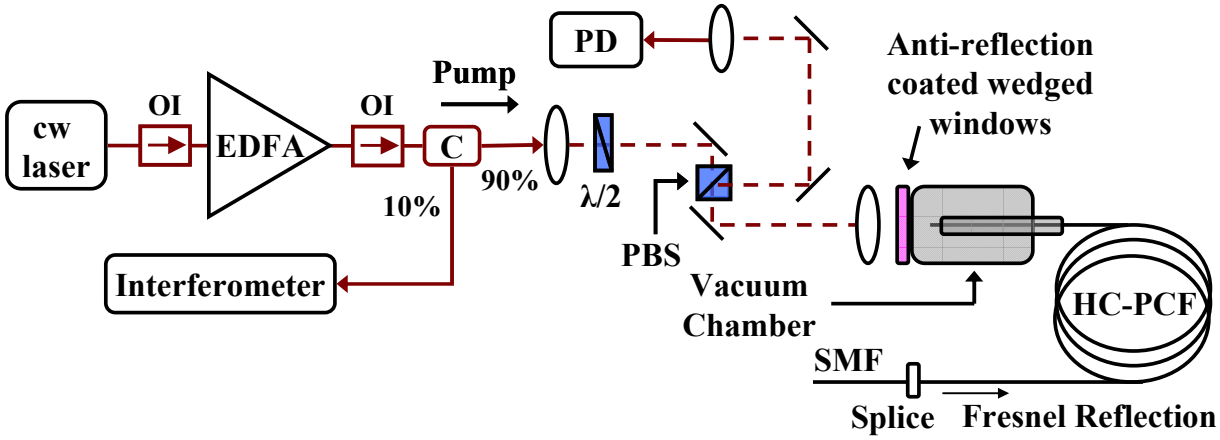

Figure 5.3 Saturated absorption spectroscopy schematic using a reflected pump beam from a spliced 20 µm HC-PCF/SMF half cell.

Two different 20 µm HC-PCFs listed in Table 5.1 were used to measure the absorption data. Figure 5.4a shows spectra inside Fiber 2 filled with 500 mtorr of acetylene at various powers exiting the fiber. At higher optical powers, more molecules become saturated, as can be seen in the absorption's reduction. The oscillatory background transmission is due to wavelength-dependent coupling between core modes and surface modes [27]. This coupling is caused by the location of the transmission band-edge of the HC-PCF. Fiber has recently been fabricated to reduce this effect [42], and would be better suited for gas cells.

Table 5.1 Fiber half-cells used for saturated absorption spectroscopy.

Fiber	PCF Length (m)	PCF Fiber Type	Splice Loss (dB)	
			(SMF → PBGF)	(PBGF → SMF)
2	0.40	19 cell 20µm HC19-1550-01 Crystal Fibre A/S	0.3 - 0.5	> 2.0
3	2.60			

Figure 5.4b and c show the observed broadening of the sub-Doppler linewidth as a function of pressure and power. The pressure data were taken at a power of 50 mW exiting the

HC-PCF fiber (30 mW was measured exiting the SMF, and the average measured splice loss was 2.2 dB), and therefore exhibits more broadening that those widths shown in Figure 2.5. Both graphs show that the measured linewidths had more scatter in Fiber 3, which can be attributed to a larger amplitude of surface modes than observed in Fiber 2.

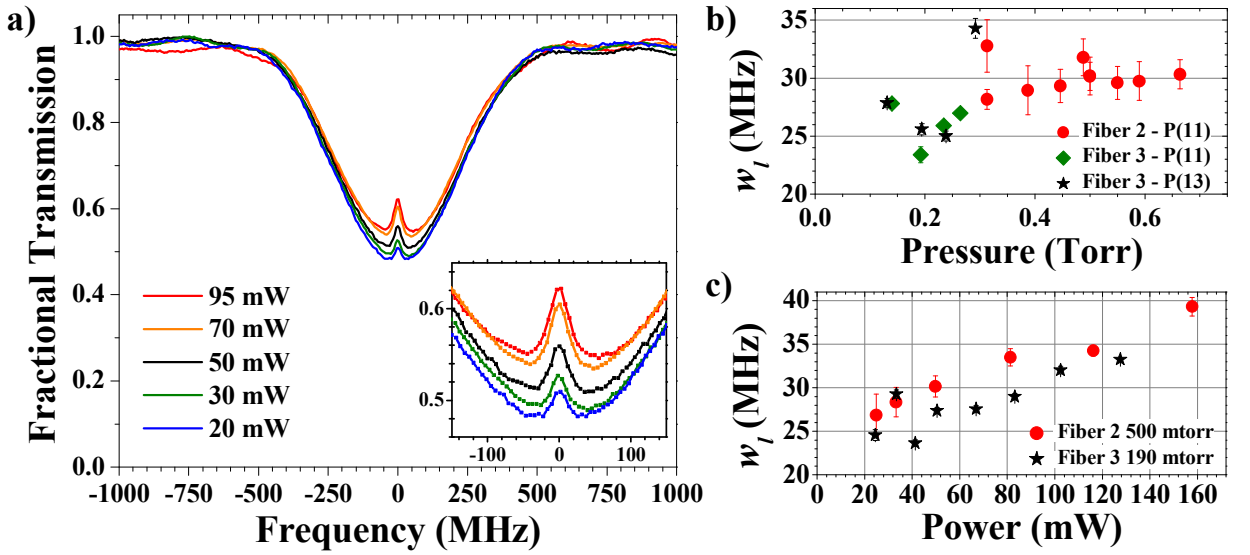

Figure 5.4 Linewidth data for saturated absorption spectroscopy using a pump reflection in HC-PCF. (a) Fractional transmission versus frequency in Fiber 2 with a pressure of 500 mtorr and at various optical powers. As the pump power is increased, transparency in the Doppler profile is observed, as well as broadening of the sub-Doppler feature (seen in inset). (b) Sub-Doppler linewidth w_l versus pressure. These data were taken at 50 mW exiting the fiber, and therefore exhibit more power broadening than those signals in Figure 2.5. Data taken in Fiber 3 appear to have had more surface modes present, and therefore exhibit more scatter than data taken in Fiber 2. (c) Sub-Doppler linewidth w_l versus power.

Equation 2.4 was used to fit the data in Figure 5.4a, although A_g is expected to be a factor 2 larger and A_l a factor two smaller in this setup than in the two-beam technique for the same gas pressure and fiber length, in the limit of low pump power. This arises because the probe beam is inherently created from the pump beam and therefore experiences the same absorption as the pump beam (see Figure 5.3). At low powers, this leads to the probe's absorbance being twice as large as in the two-beam case because it travels twice the path length. However, when the power of the pump beam approaches the saturation limit, the fractional transmission of the pump beam increases. Mathematically, we approximate the absorbance, neglecting propagation effects, as:

$$A_g = A_{g0}(1+(1+P/P_S)^{-1/2}) \qquad 5.1$$

where A_g is the peak absorbance of the pump beam at low powers [23]. In contrast, $A_g = A_{g,0}$ for the two beam probe absorbance. The functional dependence of Equation 5.1 is observed in Figure 5.4 as an increase in the amplitude of the fractional transmission on resonance with increasing power.

Progress towards making fiber cells

Dr. Corwin's research group has constructed a CO_2 laser splicer for fiber cell fabrication. is coupled into the chamber in the transverse direction. Making the first splice at one of the HC-PCF a half-cell (i.e. joining a solid core fiber to one end of the HC-PCF) can be done with a conventional fiber fusion splicer in air. The HC-PCF half-cell can then be evacuated in a vacuum chamber, where a gas at low pressure can be loaded into the fiber. While it is easily feasible to couple laser light into a vacuum and melt fiber ends, arranging the fibers in a precise manner so as to maximize optical transmission through the fibers is not an easy task.

Therefore, alternate methods were sought to create a fiber cell. One such technique is given by Ref. [72], where a low pressure of acetylene and a high pressure of helium (> 1 atm) are simultaneously loaded into a fiber half-cell. This allows one to remove the unspliced HC-PCF end and make a splice to solid core fiber in a conventional splicer. Contamination in the cell is minimized if the splice is made quickly because the over-pressurized helium-acetylene mix flows out of the fiber. After a successful splice, helium will diffuse out of the silica fiber after approximately 8 hours. This technique was successful in creating the first low pressure fiber cell, although with a drawback. Because both ends of the HC-PCF were cleaved at 90 degree angles, any light coupled into the cell would interfere with reflections that occur at these interfaces. This cavity interference would be detrimental to saturated absorption signals, although Dr. Benabid's lab did successfully record electromagnetically induced transparency signals (which is a 2-beam, 2-color, copropagating experiment). It is apparent that removing one of the 90 degree splices is necessary to be able to observe SAS signals with any sort of appreciable SNR. While a graduate student under the guidance of Dr. Benabid, Dr. Francois Couny discovered that it is possible to not only cleave HC-PCF at an 8 degree angle, but to

splice it to an angle cleaved solid core fiber [73]. This discovery would eliminate the back-reflection in a cell (shown in Figure 5.5), though a polarization maintaining (PM) fiber splicer is required to make this splice.

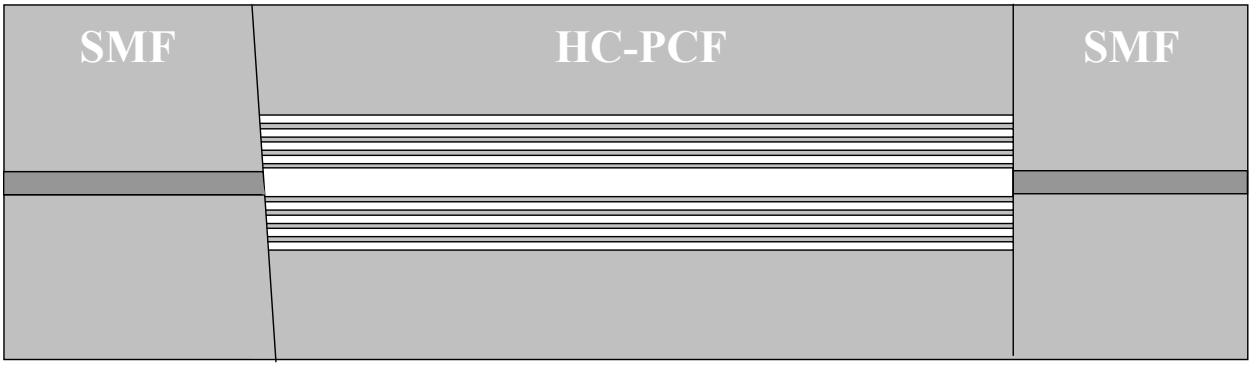

Figure 5.5 Angled HC-PCF cell schematic.

A collaboration was formed with Dr. Benabid at the University of Bath (U.K.) to work on this angled fiber cell project. Due to the resources available in Dr. Benabid's lab (including a PM splicer and essentially an endless supply of HC-PCF), it was determined that I would be sent to Bath for four months to work on this project. One-cell kagome fiber (core diameter = 25 μm) was chosen as the HC-PCF to be used in this project, as kagome fiber does not suffer from surface modes like PBGF does. The cross-section of this kagome fiber is shown in Figure 5.6 along with an example of an angle splice.

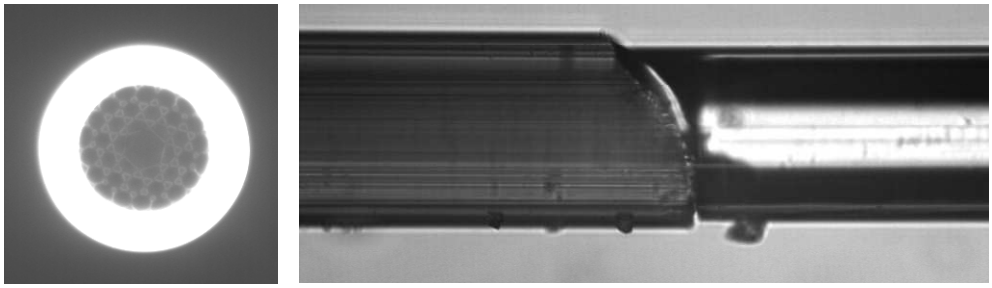

Figure 5.6 Kagome cross section and unsuccessful splice attempt (kagome HC-PCF on the left, SMF on the right). Imperfect fusion between the PCF and SMF can be seen, and allows leakage of gas into the fiber cell core.

Making a successful angle cleave on a HC-PCF is a critical first step in achieving an angle splice. This turned out to take most of my time at Bath, as the available cleaver was very inconsistent at making these cleaves Figure 5.7a-b. It was also necessary to use small pieces of

plastic (specifically bubble wrap) to buffer the HC-PCF from the cleaving arm so as not to crush the fiber. This style of cleaver (as most are) was designed with solid core fiber in mind, and the photonic crystal structure of the cladding could not withstand excessive force. Implementation of the protective plastic piece raised the repeatability of proper cleaves, though it was still at a fairly low rate (~40%).

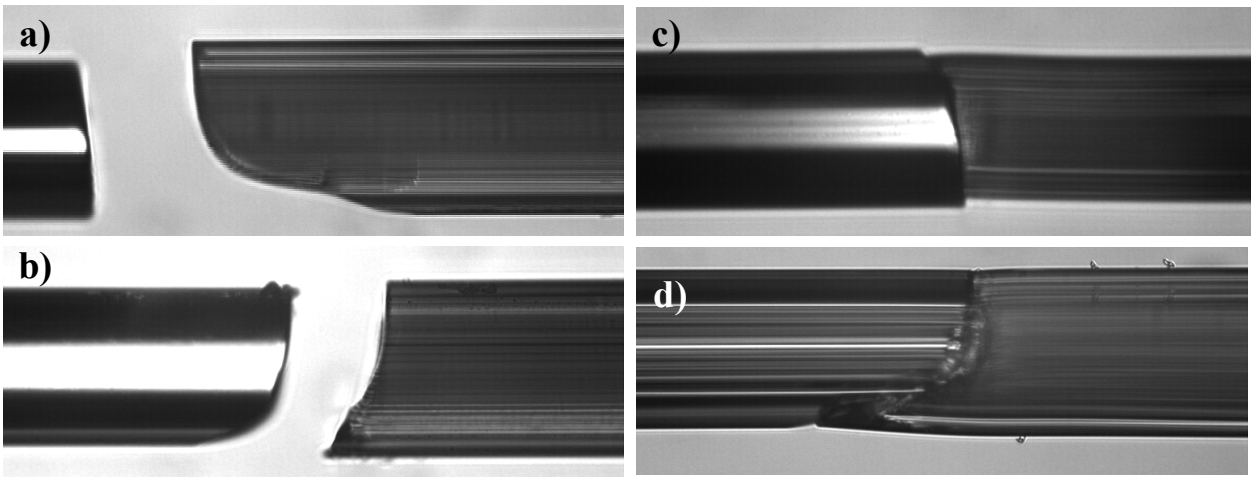

Figure 5.7 Unsuccessful SMF and PCF angle cleaves and splices (solid core fibers on the left and HC-PCF on the right for each photograph). a) Excessive shearing of the kagome fiber allows gas to leak out from the core after splicing. b) Attempts were made to denature the SMF angle cleave to complement the denatured HC-PCF angle cleave. Leaks were still present after splicing. c) and d) Even though splices appeared to be fused all the way around the fiber, it was consistently seen that leakage occurred, indicating at least some partial region had not made solid contact between the PCF and SMF.

Before the higher repeatability method of angle cleaving HC-PCF was found, splices were attempted with the "bad" angle cleaves. While the fibers appeared to be fused together, and the optical loss was not detrimental, small leaks were found that allowed the acetylene in the core to escape. A successful angle splice was eventually made, but other problems persisted with respect to the fiber gas cell fabrication. Cells were made where the Doppler absorption profile could be seen, but sub-Doppler features were never observed indicating gas contamination (most likely making the second splice).

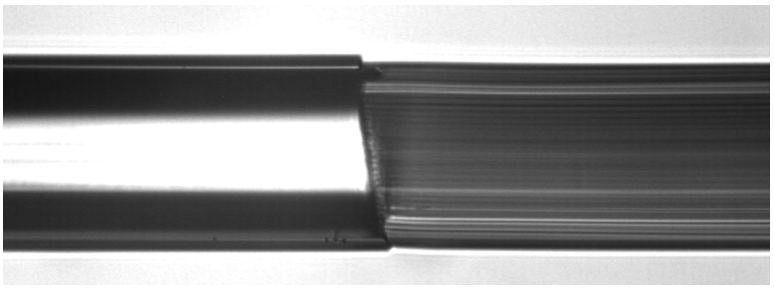

Figure 5.8 Successful angle splice with low optical loss and relative high mechanical strength.

Future prospects for HC-PCF gas cells

Investigation of HC-PCF splicing to solid core SMF in this chapter was restricted to 10 and 20 μm PBGF and single cell 25 μm kagome HC-PCF due to the size of the optical mode field diameters in these fibers. Larger core fiber, such as 70 μm kagome HC-PCF, would exhibit much higher transmission loss when fused to SMF due to the large mode field diameter mismatch. It is of course possible to use solid core multimode fiber (where core sizes range from 50 – 60 μm) instead of SMF, though not all fiber optic components are available with this fiber type (and when they are, they tend to be more expensive).

Efforts were conducted to test the stability of a reference based on 10 μm PBGF due to the similar size of this fiber's mode field diameter when compared with that of SMF's. A setup similar to Figure 3.4 was implemented to stabilize a cw fiber laser, and the resulting fractional frequency instability of the subsequent heterodyne experiment with a stabilized frequency comb is plotted in Figure 5.9. At short time scales, the instability is roughly a factor of 10 worse than data collected in the 70 μm kagome HC-PCF, which is consistent with the reduction of the slope of the sub-Doppler dispersion feature (estimated from the discrimination in Figure 2.7). Also, the optimal instability was calculated to be 2.2×10^{-11} from Equation 4.14 (where SNR = 37, $\Delta f = 38\,\text{MHz}$, and BW = 60 kHz). This value, while a factor of 10 above that of the optimal calculated instability in kagome fiber, is a factor of 10 below the observed value in 10 μm HC-PCF. Efforts to optimize the stability of this reference were not conducted, and require further investigation. Additionally, it would be interesting to investigate the accuracy of such a reference to determine how useful this fiber would be for sealed-cell references.

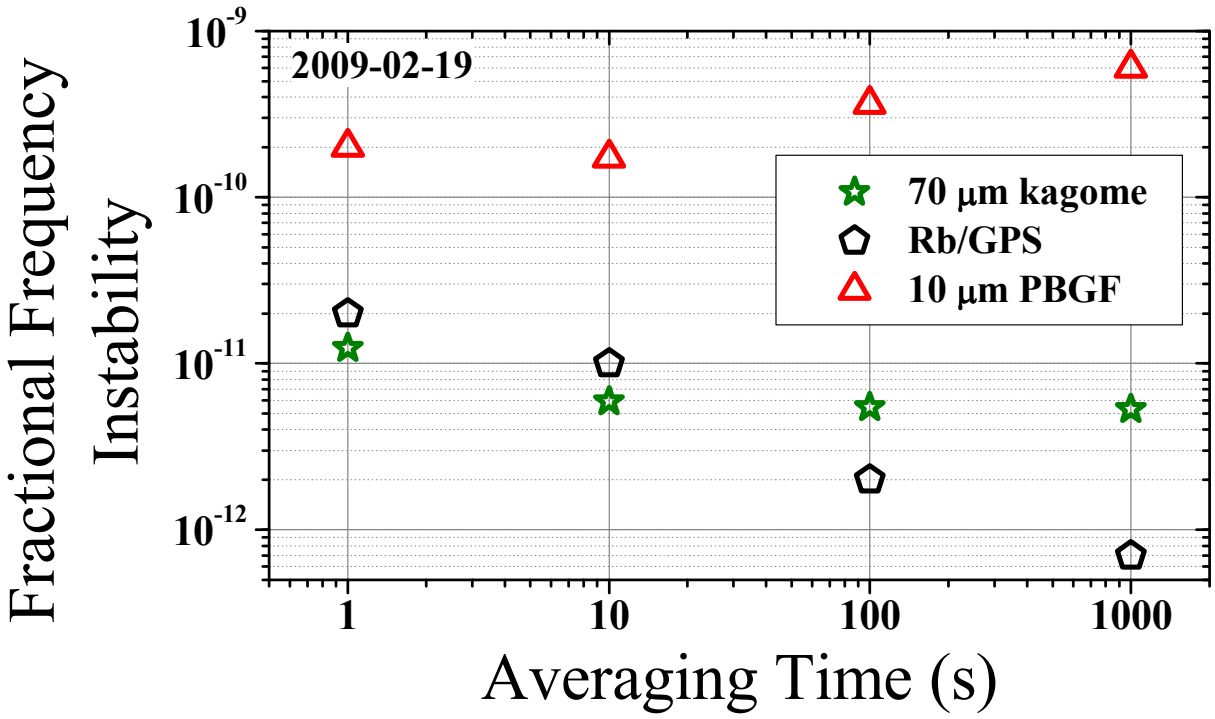

Figure 5.9 Fractional frequency instability of the cw acetylene reference using 10 μm PBGF versus averaging time. Also included are the instabilities for the Rb/GPS and the cw acetylene reference based on 70 μm kagome HC-PCF. The length of the 10 μm PBGF was 2 m, and the internal fiber pressure was 410 mtorr. The optical pump power exiting the fiber was 100 mW and the SNR of the sub-Doppler dispersion feature was 37.

Despite the choice of HC-PCF to implement in a cw acetylene reference, testing of an all fiber device is necessary to ensure that the stability and accuracy are not degraded (due to reflections from the splice interfaces between the solid and hollow core fibers, for example). However, once these sealed cells have been characterized it would not be difficult to imagine how to incorporate them into a portable package so that they could be integrated into an existing fiber network. Using a standard 19" rackmount box just a few inches in height, one could securely place all of the fiber components so that this unit could be portable. The cw laser, photodetector, synthesizers, and stabilization electronics could all be housed in this same box. Besides basic electrical power requirements, an oscilloscope would be the only other necessary external component to monitor the error signal while locking the laser. This unit could provide stable, accurate near-IR light that could either be used for a direct heterodyne measurement with an unknown optical source or as a standalone reference (which would be useful for stabilizing a

frequency comb and thereby providing a broad spectrum of coherent sources, or testing telecommunication components such as wavelength division multiplexers).

CHAPTER 6 - Conclusion

Three different HC-PCFs of varying core sizes were investigated for their potential use in portable optical frequency references. These fibers were 10 μm and 20 μm PBGF and 70 μm HC-PCF, and their ends were inserted in vacuum chambers and then filled with acetylene ($^{12}C_2H_2$). Saturated absorption spectroscopy was performed on these fibers so that narrow sub-Doppler linewidths of the v_1+v_3 overtone transition could be observed [40, 41]. The fiber cores impose a limited interation time, or transit-time, between the molecules and the laser field. The observed linewidths are largely determined by this transit-time broadening, and scale as the inverse of the core diameter. The narrowest sub-Doppler features (8 MHz) to date were observed in the kagome HC-PCF and were reported in Ref. [41].

FM spectroscopy, a modified version of saturated absorption spectroscopy, was then implemented so that the frequency of a cw laser could be stabilized to an acetylene transition. FM spectroscopy can be implemented with large RF frequencies where the technical noise is low, and boasts the ability to generate dispersion curves. These dispersion curves have a zero-crossing at the absorption line center, and are easy to stabilize using standard servo electronics.

Kagome HC-PCF was chosen as the basis for the cw optical reference because it exhibits the narrowest linewidths in the considered fibers. For full characterization, a heterodyne beat between the cw reference and an optical frequency comb stabilized to a Rb/GPS clock was conducted. The absolute frequency of the reference was found to within 100 kHz using a Vernier scale method [60] where a free-space frequency comb's repetition rate was altered during stabilization. Because free-space cw references can achieve ~1 kHz accuracies with ~1 MHz linewidths, ~10 kHz accuracies were expected for these ~10 MHz wide lines. The source of the observed inaccuracy was investigated, and it was found that frequency shifts larger than 100 kHz were caused by changing the alignment into the kagome fiber and the fiber leading to the photodetector. These effects were not intensity related, and are most likely caused in part by the multimode nature of the kagome fiber. Because the pump and probe beam are most likely coupled into slightly different sets of modes, changing the coupling can easily make either beam couple into different sets of modes which have different angles of propagation down the length of the fiber. Work in Ref. [37] has shown that when the pump and probe beams are passed

through a gas sample at an angle to one another, shifts can result depending on where the crossing point occurs. Even with these shifts present, careful alignment allowed this error to be transformed into a statistical error (1 σ) of ±5.4 kHz. This error had other uncertainties added in quadrature relating to pressure and power broadening effects, bringing the total error to ±9.3 kHz. This is a significant result because it not only achieves the level of our estimation of the optimal accuracy of this fiber system, but also improves the potential portable accuracy by four orders of magnitude (from 100 MHz to 10 kHz).

Stability of the cw reference was also investigated, where fractional frequency instabilities of 1.2×10^{-11} at 1 s, 5.9×10^{-12} at 10 s, 5.4×10^{-12} at 100 s, and 5.3×10^{-12} at 1000 s averaging times were observed. The measurements made at 1 and 10 s were limited by the Rb/GPS reference and set an upper limit to the fractional instability. The data show a near constant value at 100 and 1000 s and is due to the cw reference's dependence on the room's air conditioning cycles (the root cause of which is still being investigated). The fractional instability is also less than an order of magnitude higher than that of free-space experiments [14, 15, 22].

Techniques were also investigated to try and reduce the observed linewidth in kagome HC-PCF using slow molecule selection. Linewidth reduction by a factor of two was observed, though this necessitated low optical pump powers and pressures which both contribute to an overall degraded SNR. Placing the fiber in cold temperature baths was then investigated to see if reducing the average thermal velocity led to further linewidth reduction or increased SNR. Only the increased SNR was observed (the lower temperature increases the number of molecules available for saturation), though without linewidth reduction. This is most likely explained by estimating that the fastest molecules collide with the fiber core walls before absorbing a photon (on average), and while reducing the temperature does change the average thermal velocity, a similar spread in thermal distributions is observed.

Most of this work was conducted with the fiber ends inserted into vacuum chambers to measure its optimum potential for use in an optical frequency reference. Work was also conducted to fabricate a low pressure HC-PCF fiber cell with one of the ends spliced at an angle. This angle splice was investigated to reduce cavity interference effects caused by solid core fibers fused to either side of a HC-PCF with normal cleaves. This project was difficult as gas contamination during the splicing process was quite common. Efforts are ongoing to fabricate such a cell, as a kagome HC-PCF cell may exhibit lower uncertainty as a reference due to the

fusion of solid core fibers fixing the alignment into the cell, especially when vibrationally isolated. Packaging such a fiber cell into a portable unit useful for commercial applications would be relatively straightforward, where a portable frequency comb could be included and stabilized to the cw acetylene reference to provide a broad spectrum optical reference in the near-IR.

References

1. "John Harrison," (2010), http://en.wikipedia.org/wiki/John_Harrison.

2. D. Sobel, *Longitude: The True Story of a Lone Genius Who Solved the Greatest Scientific Problem of His Time* (Walker & Company, 2007).

3. A. A. Michelson, American Journal of Science **38**, 225 (1889).

4. "Telecommunication," (2010), http://en.wikipedia.org/wiki/Telecommunication.

5. "The Birth of Fiber Optics," (2010), http://inventors.about.com/library/weekly/aa980407.htm.

6. J. Hecht, *City of Light: The Story of Fiber Optics* (Oxford University Press, USA, 2004).

7. O. E. Delange, "Wide-band optical communication systems .2. Frequency-division multiplexing," Proceedings of the Institute of Electrical and Electronics Engineers **58**, 1683-& (1970).

8. S. Sugimoto, K. Minemura, K. Kobayashi, M. Seki, M. Shikada, A. Ueki, T. Yanase, and T. Miki, "High-speed digital-signal transmission experiments by optical wavelength-division multiplexing," Electron. Lett. **13**, 680-682 (1977).

9. T. Miki, and H. Ishio, "Viabilities of wavelength-division-multiplexing transmission-systems over an optical fiber cable," IEEE Trans. Commun. **26**, 1082-1087 (1978).

10. "Wavelength Division Multiplexing," (2010), http://en.wikipedia.org/wiki/Wavelength-division_multiplexing.

11. "Bureau International des Poids et Mesures Recommendation CCL 2c," (2003).

12. W. C. Swann, and S. L. Gilbert, "Pressure-induced shift and broadening of 1510-1540-nm acetylene wavelength calibration lines," Journal of the Optical Society of America B-Optical Physics **17**, 1263-1270 (2000).

13. C. S. Edwards, G. P. Barwood, H. S. Margolis, P. Gill, and W. R. C. Rowley, "High-precision frequency measurements of the v(1) + v(3) combination band of (C2H2)-C-12 in the 1.5 mu m region," J. Mol. Spectrosc. **234**, 143-148 (2005).

14. A. A. Madej, A. J. Alcock, A. Czajkowski, J. E. Bernard, and S. Chepurov, "Accurate absolute reference frequencies from 1511 to 1545 nm of the v(1)+v(3) band of (C2H2)-C-12

determined with laser frequency comb interval measurements," Journal of the Optical Society of America B-Optical Physics **23**, 2200-2208 (2006).

15. H. S. Moon, W. K. Lee, and H. S. Suh, "Absolute-frequency measurement of an acetylene-stabilized laser locked to the P(16) transition of (C2H2)-C-13 using an optical-frequency comb," IEEE Transactions on Instrumentation and Measurement **56**, 509-512 (2007).

16. M. de Labachelerie, K. Nakagawa, and M. Ohtsu, "Ultranarrow (C2H2)-C-13 Saturated-Absorption Lines at 1.5 Mu-M," Optics Letters **19**, 840-842 (1994).

17. K. Nakagawa, M. deLabachelerie, Y. Awaji, and M. Kourogi, "Accurate optical frequency atlas of the 1.5-mu m bands of acetylene," Journal of the Optical Society of America B-Optical Physics **13**, 2708-2714 (1996).

18. R. W. P. Drever, J. L. Hall, F. V. Kowalski, J. Hough, G. M. Ford, A. J. Munley, and H. Ward, "Laser phase and frequency stabilization using an optical-resonator," Applied Physics B-Photophysics and Laser Chemistry **31**, 97-105 (1983).

19. M. Kourogi, K. Nakagawa, and M. Ohtsu, "Wide-span optical frequency comb generator for accurate optical frequency difference measurement," IEEE J. Quantum Electron. **29**, 2693-2701 (1993).

20. A. Czajkowski, A. A. Madej, and P. Dube, "Development and study of a 1.5 mu m optical frequency standard referenced to the P(16) saturated absorption line in the (v(1)+v(3)) overtone band of (C2H2)-C-13," Opt. Commun. **234**, 259-268 (2004).

21. C. S. Edwards, H. S. Margolis, G. P. Barwood, S. N. Lea, P. Gill, and W. R. C. Rowley, "High-accuracy frequency atlas of (C2H2)-C-13 in the 1.5 mu m region," Appl. Phys. B-Lasers Opt. **80**, 977-983 (2005).

22. P. Balling, M. Fischer, P. Kubina, and R. Holzwarth, "Absolute frequency measurement of wavelength standard at 1542nm: acetylene stabilized DFB laser," Opt. Express **13**, 9196-9201 (2005).

23. W. Demtroder, *Laser Spectroscopy: Basic Concepts and Instrumentation* (Springer, 2003).

24. "Corning," (2010), www.corning.com.

25. E. A. J. Marcatili, and R. A. Schmeltzer, "Hollow metallic + dielectric waveguides for long distance optical transmission + lasers," Bell System Technical Journal **43**, 1783-+ (1964).

26. "NKT Photonics," http://www.nktphotonics.com/.

27. J. A. West, C. M. Smith, N. F. Borrelli, D. C. Allan, and K. W. Koch, "Surface modes in air-core photonic band-gap fibers," (Optical Soc Amer, 2004), pp. 1485-1496.
28. F. Couny, F. Benabid, and P. S. Light, "Large-pitch kagome-structured hollow-core photonic crystal fiber," Optics Letters **31**, 3574-3576 (2006).
29. A. Szoke, and A. Javan, "Effects of collisions on saturation behavior of 1.15 micron transition of Ne studied with He-Ne laser," Physical Review **145**, 137-& (1966).
30. R. L. Barger, and J. L. Hall, "Pressure shift and broadening of methane line at 3.39 microns studeied by laser-saturated molecular absorption," Physical Review Letters **22**, 4-& (1969).
31. T. W. Hänsch, and P. E. Toschek, "On pressure broadening in a He-Ne laser," IEEE J. Quantum Electron. **QE 5**, 61-& (1969).
32. C. Borde, "Saturated absorption spectroscopy of various molecules using lasers with carbonic gas and nitrogen protoxide," Comptes Rendus Hebdomadaires Des Seances De L Academie Des Sciences Serie B **271**, 371-& (1970).
33. T. W. Hänsch, I. S. Shahin, and A. L. Schawlow, "High-resolution saturation spectroscopy of sodium D lines with a pulsed tunable dye laser," Physical Review Letters **27**, 707-& (1971).
34. C. J. Borde, J. L. Hall, C. V. Kunasz, and D. G. Hummer, "Saturated absorption line shape - calculation of transit-time broadening by a perturbation approach," Phys. Rev. A **14**, 236-263 (1976).
35. J. L. Hall, and C. J. Borde, "Shift and broadening of saturated absorption resonances due to curvature of laser wave fronts," Appl. Phys. Lett. **29**, 788-790 (1976).
36. J. L. Hall, L. Hollberg, T. Baer, and H. G. Robinson, "Optical Heterodyne Saturation Spectroscopy," Appl. Phys. Lett. **39**, 680-682 (1981).
37. S. E. Park, H. S. Lee, T. Y. Kwon, and H. Cho, "Dispersion-like signals in velocity-selective saturated-absorption spectroscopy," Opt. Commun. **192**, 49-55 (2001).
38. L. F. Stokes, M. Chodorow, and H. J. Shaw, "All single-mode fiber resonator," Optics Letters **7**, 288-290 (1982).
39. J. Henningsen, J. Hald, and J. C. Petersen, "Saturated absorption in acetylene and hydrogen cyanide in hollow-core photonic bandgap fibers," Optics Express **13**, 10475-10482 (2005).

40. R. Thapa, K. Knabe, M. Faheem, A. Naweed, O. L. Weaver, and K. L. Corwin, "Saturated absorption spectroscopy of acetylene gas inside large-core photonic bandgap fiber," Optics Letters **31**, 2489-2491 (2006).

41. K. Knabe, S. Wu, J. Lim, K. Tillman, R. Thapa, A. Jones, B. R. Washburn, J. W. Nicholson, P. S. Light, F. C. Couny, N. Wheeler, F. Benabid, and K. L. Corwin, "10 kHz accuracy of an optical frequency reference based on $^{12}C_2H_2$-filled large-core kagome photonic crystal fibers," Optics Express **17**, 16017-16026 (2009).

42. R. Amezcua-Correa, F. Gerome, S. G. Leon-Saval, N. G. R. Broderick, T. A. Birks, and J. C. Knight, "Control of surface modes in low loss hollow-core photonic bandgap fibers," Optics Express **16**, 1142-1149 (2008).

43. G. Bjorklund, M. Levenson, W. Lenth, and C. Ortiz, "Frequency Modulation (FM) Spectroscopy," Applied Physics B **32**, 145-152 (1983).

44. J. V. Acrivos, "Application of sideband technique to wide-line NMR spectra," J. Chem. Phys. **36**, 1097-& (1962).

45. B. Smaller, "Precise determination of the magnetic moment of the deuteron," Physical Review **83**, 812-820 (1951).

46. NIST, "Time and Frequency from A to Z," http://tf.nist.gov/general/glossary.htm.

47. D. W. Allan, J. H. Shoaf, and D. Halford, "Statistics of time and frequency data analysis," in *Time and Frequency: Theory and Fundamentals*, B. E. Blair, ed. (U.S. Department of Commerce, 1974), pp. 153-190.

48. K. M. Evenson, J. S. Wells, F. R. Petersen, Danielso.Bl, and G. W. Day, "Accurate frequencies of molecular transitions used in laser stabilization - 3.39 micron transition in CH4 and 9.33 micron and 10.18 micron transitions in CO2," Appl. Phys. Lett. **22**, 192-195 (1973).

49. R. Teets, J. Eckstein, and T. W. Hänsch, "Coherent 2-photon excitation by multiple light-pulses," Physical Review Letters **38**, 760-764 (1977).

50. D. J. Jones, S. A. Diddams, J. K. Ranka, A. Stentz, R. S. Windeler, J. L. Hall, and S. T. Cundiff, "Carrier-envelope phase control of femtosecond mode-locked lasers and direct optical frequency synthesis," Science **288**, 635-639 (2000).

51. S. T. Cundiff, J. Ye, and J. L. Hall, "Optical frequency synthesis based on mode-locked lasers," Rev. Sci. Instrum. **72**, 3749-3771 (2001).

52. K. A. Tillman, R. Thapa, B. R. Washburn, and K. L. Corwin, "Significant Carrier Envelope Offset Frequency Linewidth Narrowing in a Prism-Based Cr:Forsterite Frequency Comb " in *Proceedings of CLEO CTuC5*(2009).

53. K. A. Tillman, R. Thapa, K. Knabe, S. Wu, J. K. Lim, B. R. Washburn, and K. L. Corwin, "Stabilization of a self-referenced, prism-based, Cr:forsterite laser frequency comb using an intracavity prism," Appl. Optics **48**, 6980-6989 (2009).

54. B. R. Washburn, S. A. Diddams, N. R. Newbury, J. W. Nicholson, M. F. Yan, and C. G. Jorgensen, "Phase-locked, erbium-fiber-laser-based frequency comb in the near infrared," Optics Letters **29**, 250-252 (2004).

55. J. Lim, K. Knabe, K. A. Tillman, W. Neely, Y. Wang, R. Amezcua-Correa, F. Couny, P. S. Light, F. Benabid, J. C. Knight, K. L. Corwin, J. W. Nicholson, and B. R. Washburn, "A phase-stabilized carbon nanotube fiber laser frequency comb," Optics Express **17**, 14115-14120 (2009).

56. Y. Wang, J. Lim, R. Amezcua-Correa, J. C. Knight, and B. R. Washburn, "Sub-33 fs Pulses from an All-Fiber Parabolic Amplifier Employing Hollow-Core Photonic Bandgap Fiber," in *Frontiers In Optics*(2008).

57. K. Knabe, J. Lim, K. Tillman, R. Thapa, F. Couny, P. S. Light, J. W. Nicholson, B. R. Washburn, F. Benabid, and K. L. Corwin, "Stability of an Acetylene Frequency Reference inside Kagome Structured Hollow-Core Photonic Crystal Fiber," in *Proceedings of CLEO CWB5* (2009).

58. T. Liu, Y. N. Zhao, V. Elman, A. Stejskal, and L. J. Wang, "Characterization of the absolute frequency stability of an individual reference cavity," Optics Letters **34**, 190-192 (2009).

59. A. Premoli, and P. Tavella, "A revisited 3-cornered hat method for estimating frequency standard instability " IEEE Transactions on Instrumentation and Measurement **42**, 7-13 (1993).

60. L. S. Ma, Z. Y. Bi, A. Bartels, K. Kim, L. Robertsson, M. Zucco, R. S. Windeler, G. Wilpers, C. Oates, L. Hollberg, and S. A. Diddams, "Frequency uncertainty for optically referenced femtosecond laser frequency combs," IEEE J. Quantum Electron. **43**, 139-146 (2007).

61. E. A. J. Marcatili, and R. A. Schmeltzer, "Hollow Metallic and Dielectric Wave-guides for Long Distance Optical Transmission and Lasers," The Bell System Technical Journal, 1783-1809 (1964).

62. F. Benabid, F. Couny, J. C. Knight, T. A. Birks, and P. S. Russell, "Compact, stable and efficient all-fibre gas cells using hollow-core photonic crystal fibres," Nature **434**, 488-491 (2005).

63. A. A. Madej, J. E. Bernard, A. J. Alcock, A. Czajkowski, and S. Chepurov, "Accurate absolute frequencies of the nu(1) + nu(3) band of (C2H2)-C-13 determined using an infrared mode-locked Cr : YAG laser frequency comb," Journal of the Optical Society of America B-Optical Physics **23**, 741-749 (2006).

64. S. T. Dawkins, J. J. McFerran, and A. N. Luiten, "Considerations on the measurement of the stability of oscillators with frequency counters," IEEE Transactions on Ultrasonics Ferroelectrics and Frequency Control **54**, 918-925 (2007).

65. L. Hollberg, C. W. Oates, G. Wilpers, C. W. Hoyt, Z. W. Barber, S. A. Diddams, W. H. Oskay, and J. C. Bergquist, "Optical frequency/wavelength references," J. Phys. B-At. Mol. Opt. Phys. **38**, S469-S495 (2005).

66. R. A. McFarlane, W. R. Bennett, and W. E. Lamb, "Single mode tuning dip in the power output of an He-Ne optical maser," Appl. Phys. Lett. **2**, 189-190 (1963).

67. J. Hald, J. C. Petersen, and J. Henningsen, "Saturated optical absorption by slow molecules in hollow-core photonic band-gap fibers," Physical Review Letters **98**, 213902-213901-213902-213904 (2007).

68. T. Tassaing, P. Lalanne, S. Rey, F. Cansell, and M. Besnard, "Spectroscopic Study of the Polystyrene//CO2/Ethanol System," Industrial & Engineering Chemistry Research **39**, 4470-4475 (2000).

69. "Air Liquide Gas Encyclopaedia," (2010), http://encyclopedia.airliquide.com/encyclopedia.asp.

70. F. Couny, P. S. Light, F. Benabid, and P. S. Russell, "Electromagnetically induced transparency and saturable absorption in all-fiber devices based on (C2H2)-C-12-filled hollow-core photonic crystal fiber," Opt. Commun. **263**, 28-31 (2006).

71. R. Thapa, K. Knabe, K. L. Corwin, and B. R. Washburn, "Arc fusion splicing of hollow-core photonic bandgap fibers for gas-filled fiber cells," Optics Express **14**, 9576-9583 (2006).

72. P. S. Light, F. Couny, and F. Benabid, "Low optical insertion-loss and vacuum-pressure all-fiber acetylene cell based on hollow-core photonic crystal fiber," Optics Letters **31**, 2538-2540 (2006).

73. F. Couny, F. Benabid, and P. S. Light, "Reduction of fresnel back-reflection at splice interface between hollow core PCF and single-mode fiber," IEEE Photonics Technology Letters **19**, 1020-1022 (2007).

74. S. T. Thornton, and J. B. Marion, *Classical Dynamics of Particles and Systems* (Thomson, Brooks, & Cole, 2004).

75. G. Herzberg, *Molecular Spectra and Molecular Structure: II. Infrared and Raman Spectra of Polyatomic Molecules* (D. Van Nostrand Company, New York, 1945).

76. E. Merzbacher, *Quantum Mechanics* (John Wiley & Sons, Inc., New York, 1998).

77. *Santec Operation Manual for TSL-210 Tunable LD Light Source* (1997).

Peer reviewed presentations and publications

Peer reviewed presentations

1. K. Knabe, J. Lim, K. Tillman, R. Thapa, F. Couny, P. S. Light, J. W. Nicholson, B. R. Washburn, F. Benabid, and K. L. Corwin, "Stability of an Acetylene Frequency Ref. inside Kagome Structured Hollow-Core Photonic Crystal Fiber," in *Proceedings of CLEO CWB5* (2009).
2. K. Knabe, A. Jones, K. L. Corwin, F. Couny, P. S. Light, and F. Benabid, "Saturated Absorption Spectroscopy of C2H2 inside a Hollow, Large-Core Kagome Photonic Crystal Fiber," in *Proceedings of CLEO JFA5*(2008).
3. K. L. Corwin, and K. Knabe, "International exchange to create portable optical frequency references in photonic bandgap fiber," in *NSF International Research and Education for Engineers 2008 Grantees Conference (Invited Talk)*(2008).
4. K. Knabe, R. Thapa, B. R. Washburn, and K. L. Corwin, "Reflected Pump Technique for Saturated Absorption Spectroscopy inside Photonic Bandgap Fibers," in *Proceedings of CLEO JThD46*(2007).
5. K. Knabe, R. Thapa, O. L. Weaver, B. R. Washburn, and K. L. Corwin, "Saturated Absorption Spectroscopy in Acetylene Filled Photonic Bandgap Fibers," in *Proceedings of Laser Science LWC5* (2006).

Peer reviewed publications

1. K. A. Tillman, R. Thapa, K. Knabe, S. Wu, J. Lim, B. R. Washburn, and K. L. Corwin, "Stabilization of a Self-referenced, Prism-based, Cr:forsterite Laser Frequency Comb Using an Intracavity Prism," Applied Optics **48**, 6980-6989 (2009).
2. J. K. Lim, K. Knabe, K. A. Tillman, W. Neely, Y. S. Wang, R. Amezcua-Correa, F. Couny, P. S. Light, F. Benabid, J. C. Knight, K. L. Corwin, J. W. Nicholson, and B. R. Washburn, "A phase-stabilized carbon nanotube fiber laser frequency comb," Opt. Express **17**, 14115-14120 (2009).

3. J. Lim, K. Knabe, Y. Wang, R. Amezcua-Correa, F. Couny, P. S. Light, F. Benabid, J. C. Knight, K. L. Corwin, J. W. Nicholson, and B. R. Washburn, "Phase-Stabilized 167 MHz Repetition Frequency Carbon Nanotube Fiber Laser Frequency Comb," in *Proceedings of CLEO CTuK2* (2009).

4. K. Knabe, S. Wu, J. Lim, K. Tillman, R. Thapa, A. Jones, B. R. Washburn, J. W. Nicholson, P. S. Light, F. C. Couny, N. Wheeler, F. Benabid, and K. L. Corwin, "10 kHz accuracy of an optical frequency reference based on $^{12}C_2H_2$-filled large-core kagome photonic crystal fibers," Opt. Express **17**, 16017-16026 (2009).

5. A. M. Jones, K. Knabe, J. Lim, R. Thapa, K. Tillman, F. Couny, P. S. Light, F. Benabid, B. R. Washburn, and K. L. Corwin, "Saturated Absorption Spectroscopy in Acetylene Filled Photonic Bandgap Fibers," in *Proceedings of Frontiers in Optics FWF7* (2008).

6. R. Thapa, K. Knabe, A. Nawheed, M. Faheem, B. R. Washburn, and K. L. Corwin, "Saturated Absorption Signals from Acetylene Gas Inside Photonic Bandgap Fiber," in *Proceedings of CLEO CMO5* (2006).

7. R. Thapa, K. Knabe, M. Faheem, A. Naweed, O. L. Weaver, and K. L. Corwin, "Saturated absorption spectroscopy of acetylene gas inside large-core photonic bandgap fiber," Optics Letters **31**, 2489-2491 (2006).

8. R. Thapa, K. Knabe, K. L. Corwin, and B. R. Washburn, "Arc fusion splicing of hollow-core photonic bandgap fibers for gas-filled fiber cells," Opt. Express **14**, 9576-9583 (2006).

9. J. Shakya, K. Knabe, K. H. Kim, J. Li, J. Y. Lin, and H. X. Jiang, "Polarization of III-nitride blue and ultraviolet light-emitting diodes," Appl. Phys. Lett. **86**, 3 (2005).

10. K. Knabe, J. Shakya, K. Kim, Z. Fan, J. Lin, and H. Jiang, "Polarization Properties of III-Nitride Blue and UV Light-Emitting Diodes," in *Proceedings of APS March Meeting U18.00005*(2005).

Appendix A - Calculating infrared-active transitions in the vibrational band of acetylene

Acetylene (C_2H_2) is a linear molecule of the form X_2Y_2 and can be seen in Figure A.1 . The constants and coordinates associated with each of the atoms have also been indicated.

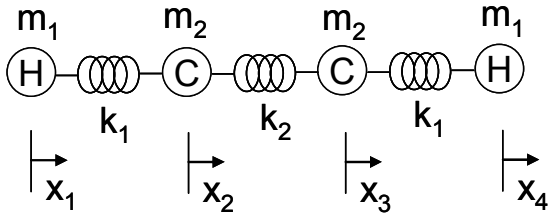

Figure A.1 A simple visual representation of the acetylene molecule as point masses and springs.

For this calculation, I have considered only motion parallel to the internuclear (IN) axis, also known as stretching motion. Motion perpendicular to the IN axis, or bending motion, could be incorporated without any fundamental difficulties; however the size of the calculations (especially for the anharmonicities) would become too cumbersome for this project.

This paper will detail the way to calculate the eigenfrequencies and normal modes of the acetylene molecule using a simple harmonic oscillator (SHO) approximation, and will then show how and why anharmonicities must be included in the potential to obtain the overtone spectrum (multiple simultaneous vibrational transitions). Acetylene (C2H2) is a linear molecule of the form X_2Y_2 and can be seen in Figure A.1. The constants and coordinates associated with each of the atoms have also been indicated.

Determination of Normal Modes

The solution of the normal modes of vibration and the eigenfrequencies of any molecule using the SHO approximation can be carried out classically [74]. The kinetic (T) and potential (U) energies of the system have the following form:

$$T = \frac{1}{2} m_1 \dot{x}_1^{\,2} + \frac{1}{2} m_2 \dot{x}_2^{\,2} + \frac{1}{2} m_2 \dot{x}_3^{\,2} + \frac{1}{2} m_1 \dot{x}_4^{\,2} \tag{A.1}$$

$$U = \frac{1}{2} k_1 (x_1 - x_2)^2 + \frac{1}{2} k_2 (x_2 - x_3)^2 + \frac{1}{2} k_1 (x_3 - x_4)^2 \tag{A.2}$$

However, for this calculation, it is much more convenient to express T and U in terms of second order tensors:

$$T = \frac{1}{2} \sum_{j,k} m_{jk} \dot{x}_j \dot{x}_k \tag{A.3}$$

$$U = \frac{1}{2} \sum_{j,k} A_{jk} x_j x_k \tag{A.4}$$

where A_{jk} is defined as

$$A_{jk} = \left. \frac{\partial^2 U}{\partial x_j \partial x_k} \right|_{equilibrium} . \tag{A.5}$$

The tensors of interest, m_{jk} and A_{jk}, have the following form:

$$m_{jk} = \begin{pmatrix} m_1 & 0 & 0 & 0 \\ 0 & m_2 & 0 & 0 \\ 0 & 0 & m_2 & 0 \\ 0 & 0 & 0 & m_1 \end{pmatrix} \tag{A.6}$$

$$A_{jk} = \begin{pmatrix} k_1 & -k_1 & 0 & 0 \\ -k_1 & k_1 + k_2 & -k_2 & 0 \\ 0 & -k_2 & k_1 + k_2 & -k_1 \\ 0 & 0 & -k_1 & k_1 \end{pmatrix} \tag{A.7}$$

Now, we consider Lagrange's equation,

$$\frac{\partial L}{\partial x_i} - \frac{d}{dt}\frac{\partial L}{\partial \dot{x}_i} = 0 \qquad \text{A.8}$$

and upon substitution ($L = T - U$) Equation A.8 becomes:

$$\frac{\partial U}{\partial x_i} + \frac{d}{dt}\frac{\partial T}{\partial \dot{x}_i} = 0\,. \qquad \text{A.9}$$

The Lagrangian now has the following tensor form:

$$\sum_j \left(A_{jk} x_j + m_{jk} \ddot{x}_j \right) = 0\,. \qquad \text{A.10}$$

We now make the assumption that our system is indeed oscillatory, and that solutions to the motion of the system should have the following form:

$$x_j(t) = a_j e^{i(\omega t - \delta)} \qquad \text{A.11}$$

where a_j and δ are the amplitude and phase of the motion determined by the initial conditions. Making this substitution into the tensor form of the Lagrangian, we find our familiar eigenvalue problem:

$$\sum_j \left(A_{jk} - \omega_r{}^2 m_{jk} \right) a_{jr} = 0 \qquad \text{A.12}$$

where ω_r denotes the eigenfrequencies of the system and a_{jr} are the eigenvectors (or $\vec{a}_r$). I took another step and multiplied the inverse of tensor m_{jk} from the left hand side to convert this problem into our more familiar version of the eigenvalue problem:

$$\sum_j \left(m_{jk}{}^{-1} A_{jk} - \omega_r{}^2 \delta_{jk} \right) a_{jr} = 0\,. \qquad \text{A.13}$$

The next step is to determine ω_r and a_{jr} by first solving

$$\left| m_{jk}^{-1} A_{jk} - \omega_r^2 \delta_{jk} \right| = 0 . \qquad \text{A.14}$$

and then substituting the individual ω_r's into the altered tensor form of the Lagrangian. However, this simple manipulation allowed me to use the "Eigensystem" command in Mathematica, which returns not only the eigenfrequencies, but their corresponding eigenvectors which are all listed in Table A.1. To obtain numbers for these quantities, the atomic masses of hydrogen and carbon were used as well as values for the force constants k_1 = 592 N/m and k_2 = 1590 N/m from Ref. [75].

Table A.1 Calculated eigenfrequencies and eigenvectors for C2H2 with NIST values for comparison

	ω_r (rad/s)	NIST ω_r	$\vec{a}_{r\,(x_1,x_2,x_3,x_4)}$
ω_1	6.346×10^{14}	6.360×10^{14}	(-1,0.14, -.14,1)
ω_2	3.731×10^{14}	3.721×10^{14}	(-1,-0.61, .61,1)
ω_3	6.192×10^{14}	6.200×10^{14}	(1,-0.084, -0.084,1)
ω_4	0	N/A	(1,1,1,1)

The agreement between calculation and experiment of the eigenfrequencies is very good. It should be noted that ω_4 isn't actually indicative of oscillatory motion (as all components of the eigenvector have the same sign), but rather of translational motion. Therefore we neglect this solution, as we are not interested in this type of motion.

Further, we should consider the eigenvectors to determine whether or not we are in a center of mass (COM) representation or not. The equation for the COM is

$$m_1(x_1 + x_4) + m_2(x_2 + x_3) = 0\,. \qquad \text{A.15}$$

Upon substituting the elements of the eigenvectors into this equation, it is found that the first three eigenvectors satisfy this condition.

Overtone Transitions

Approximating our potential as a SHO has allowed us to calculate the vibrational transition frequencies as well as determine which transitions are dipole-allowed. However, when higher order corrections are added to the potential, the normal modes get mixed and oscillatory motion at frequencies

$$\sum_{i,j}(\omega_i + \omega_j), \sum_{i,j,k}(\omega_i + \omega_j + \omega_k), \ldots \qquad \text{A.16}$$

result. Experimentally these higher order corrections, or anharmonicities, are much smaller than the harmonic terms, and generally result in lines that are weaker than the fundamental.

Staying in the basis of our normal coordinates, we can rewrite our Hamiltonian [75] as

$$H = \frac{1}{2}(\dot{\eta}_1^{\,2} + \dot{\eta}_2^{\,2} + \dot{\eta}_3^{\,2}) + \frac{1}{2}(\lambda_1\eta_1^{\,2} + \lambda_2\eta_2^{\,2} + \lambda_3\eta_3^{\,2})\,. \qquad \text{A.17}$$

The next order of correction that we can add to the potential would be a cubic term

$$V' = \sum_{i,j,k}\alpha_{ijk}\eta_i\eta_j\eta_k\,. \qquad \text{A.18}$$

With this, we can perform perturbation theory (since $\alpha_{ijk}\eta_i\eta_j\eta_k \ll \lambda_m\eta_m^2$) to obtain the wave functions to this new system and therefore calculate the matrix elements of the dipole operator. For convenience, we make a substitution of $\eta_i \propto (a_i + a_i^\dagger)$ into V' to obtain

$$V' = \sum_{i,j,k} \alpha'_{ijk} (a_i + a_i^\dagger)(a_j + a_j^\dagger)(a_k + a_k^\dagger) . \tag{A.19}$$

Perturbation theory allows us to calculate not only small adjustments to the wave functions of the system, but also the energies of transitions as well. Because of the nature of this calculation, and due to comparatively small value of the cubic potential coefficient α_{ijk}, we will not consider the energy corrections, but will only concern ourselves with the wave function correction $\psi^{(1)}_{n_1 n_2 n_3}$ (where $\left|\psi^{anharmonic}_{n_1 n_2 n_3}\right\rangle \approx \left|\psi^{(0)}_{n_1 n_2 n_3}\right\rangle + \left|\psi^{(1)}_{n_1 n_2 n_3}\right\rangle$ and $\left|\psi^{(0)}_{n_1 n_2 n_3}\right\rangle = \left|n_1 n_2 n_3\right\rangle$ is the solution to the SHO approximation). The first order correction can be directly calculated by [76]

$$\left|\psi^{(1)}_{n_1 n_2 n_3}\right\rangle = \sum_{\substack{m_1, m_2, m_3 \\ m_1 \neq n_1 \\ m_2 \neq n_2 \\ m_3 \neq n_3}} \left|m_1 m_2 m_3\right\rangle \frac{\left\langle m_1 m_2 m_3 \left| V' \right| n_1 n_2 n_3 \right\rangle}{E^{(0)}_{n_1 n_2 n_3} - E^{(0)}_{m_1 m_2 m_3}} . \tag{A.20}$$

While this appears to contain a large number of terms, representing the perturbation V' in terms of raising and lowering operators greatly simplifies the problem. First, let's consider the terms in V' where $i \neq j \neq k$. The first order correction then has the form

$$\left|\psi^{(1)}_{n_1 n_2 n_3}\right\rangle_{i \neq j \neq k} = \sum_{i \neq j \neq k} \sum_{\substack{m_1, m_2, m_3 \\ m_1 \neq n_1 \\ m_2 \neq n_2 \\ m_3 \neq n_3}} \alpha'_{ijk} \left|m_1 m_2 m_3\right\rangle \times \frac{\left\langle m_1 m_2 m_3 \left| (a_i + a_i^\dagger)(a_j + a_j^\dagger)(a_k + a_k^\dagger) \right| n_1 n_2 n_3 \right\rangle}{E^{(0)}_{n_1 n_2 n_3} - E^{(0)}_{m_1 m_2 m_3}} . \tag{A.21}$$

which reduces to

$$\left|\psi^{(1)}_{n_1 n_2 n_3}\right\rangle_{i \neq j \neq k} = \sum_{i \neq j \neq k} \frac{\alpha'_{ijk}}{E^{(0)}_{n_1 n_2 n_3} - E^{(0)}_{n_1 \pm 1, n_2 \pm 1, n_3 \pm 1}} \left| n_1 \pm 1, n_2 \pm 1, n_3 \pm 1 \right\rangle . \tag{A.22}$$

Similarly, this can be carried out for the cases when two indices ($i = j \neq k$) and all three indices are identical ($i = j = k$). It is more difficult to write these solutions in a concise form. For calculating which transitions are possible, the only relations we need are the list of SHO excited states that now make up the wave function correction, which are listed below.

$$\left|n_1 \pm 1, n_2 \pm 1, n_3 \pm 1\right\rangle, \left|n_1 \pm 2, n_2 \pm 1, n_3\right\rangle, \left|n_1 \pm 1, n_2, n_3\right\rangle, \left|n_1 \pm 3, n_2, n_3\right\rangle. \quad \text{A.23}$$

These are not all the states, rather a simple list of all the fundamentally possible changes in quantum numbers (while $\left|n_1 \pm 2, n_2 \pm 1, n_3\right\rangle$ was listed, $\left|n_1, n_2 \pm 2, n_3 \pm 1\right\rangle$ as well as any other permutation of the ± 1 and ± 2 terms are possible).

Because of the number of terms that have been added to the wave function, it's not practical to list every term when we recalculate the matrix elements of the dipole moment. However, looking at single term corrections in addition to the SHO wave function, we can qualitatively get out the possible IR transitions that were unavailable for transitions without the anharmonic potential. For example, let's consider that the anharmonic wave function has the following form (neglecting constants):

$$\left|\psi^{anharmonic}_{n_1 n_2 n_3}\right\rangle = \left|n_1 n_2 n_3\right\rangle + \left|n_1 \pm 1, n_2, n_3\right\rangle. \quad \text{A.24}$$

The dipole matrix element would then be

$$\begin{aligned}\left[\left|\vec{P}\right|\right]^{nm} &\propto \left\langle \psi^{anharmonic}_{n_1 n_2 n_3} \left| a_3 + a_3^{\dagger} \right| \psi^{anharmonic}_{m_1 m_2 m_3} \right\rangle \\ &\propto \left(\left\langle n_1 n_2 n_3 \right| + \left\langle n_1 \pm 1, n_2, n_3 \right|\right) a_3 + a_3^{\dagger} \left(\left| m_1 m_2 m_3 \right\rangle + \left| m_1 \pm 1, m_2, m_3 \right\rangle\right)\end{aligned}. \quad \text{A.25}$$

This results in four terms

$$
\begin{aligned}
t1 &= \left\langle n_1 n_2 n_3 \left| a_3 + a_3^{\dagger} \right| m_1 m_2 m_3 \right\rangle \\
t2 &= \left\langle n_1 n_2 n_3 \left| a_3 + a_3^{\dagger} \right| m_1 \pm 1, m_2, m_3 \right\rangle \\
t3 &= \left\langle n_1 \pm 1, n_2, n_3 \left| a_3 + a_3^{\dagger} \right| m_1 m_2 m_3 \right\rangle \\
t4 &= \left\langle n_1 \pm 1, n_2, n_3 \left| a_3 + a_3^{\dagger} \right| m_1 \pm 1, m_2, m_3 \right\rangle
\end{aligned}
\qquad \text{A.26}
$$

that give rise to the following selection rules

$$
\begin{aligned}
r1 &= \delta_{\Delta n_1 = 0} \delta_{\Delta n_2 = 0} \delta_{\Delta n_3 = \pm 1} \\
r2 &= \delta_{\Delta n_1 = \pm 1} \delta_{\Delta n_2 = 0} \delta_{\Delta n_3 = \pm 1} \\
r3 &= \delta_{\Delta n_1 = \pm 2} \delta_{\Delta n_2 = 0} \delta_{\Delta n_3 = \pm 1}
\end{aligned}
\qquad \text{A.27}
$$

(term $t1$ and $t4$ lead to rule $r1$; $t2$ and $t3$ lead to $r2$, and $t4$ leads to $r3$). Therefore, by including only one of the excited unperturbed eigenstate corrections, we have observed not only the IR active transition ω_3, but $\omega_1 + \omega_3$ and $2\omega_1 + \omega_3$ as well.

Appendix B - Experimental cw lasers and photodetectors

The cw lasers and photodetectors used in this work to make an optical frequency reference are described here along with their technical specifications.

Extended-cavity diode laser

The first laser available in the laboratory was the Santec TSL-210 extended cavity diode laser (ECDL). The basic setup is taken from the operations manual [77] and is shown in Figure B.1. The output of a relatively broad spectrum laser diode (LD) is directed onto a grating to narrow the linewidth, and retroreflected with an appropriately placed mirror. The grating is mounted on a rotational stage controlled by a PZT so that the resonant wavelength can be tuned from 1505 -1585 nm. Tuning is also controlled by changing the current to the laser diode, though this range is on the order of 10 GHz. Typical output powers for this laser are between 5 and 7 mW (depending on the wavelength of the output).

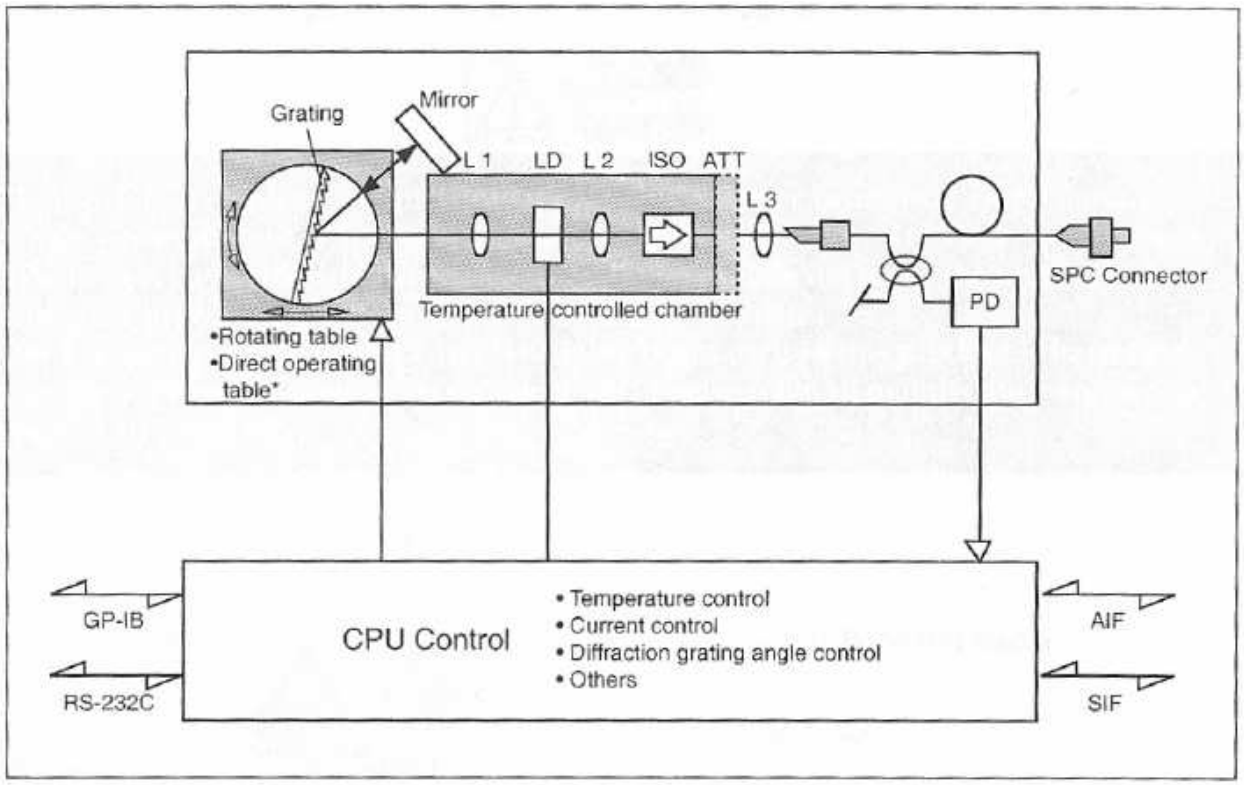

Figure B.1 Schematic of ECDL taken from Ref. [77].

The main feedback mechanism available for frequency stabilization of this laser is the current to the laser diode. A note about this, however, is that the output power is a function of the input current, so it is possible to write intensity noise on the laser output if large changes to the current are experienced. Also, when the ECDL is run at low output powers, the output power as a function of laser diode current is more severe than at high powers.

Narrow linewidth fiber laser

Narrow linewidth cw fiber lasers were purchased from Orbits Lightwave for use the laser frequency stabilization experiment. The entire cavity is composed of fiber where a section of this is specially doped gain fiber. A laser diode is used to optically pump the fiber cavity. Also, a high voltage PZT is attached to a section of the fiber to change the overall cavity length. This allows scanning of the laser frequency over a range greater than 10 GHz. Hysteresis effects are observed when applying large changes in voltage and are shown in Figure B.2. Laser output can be manually tuned between 7 and 29 mW by changing the current to the pump diode, though this does have an effect on the center frequency of the laser.

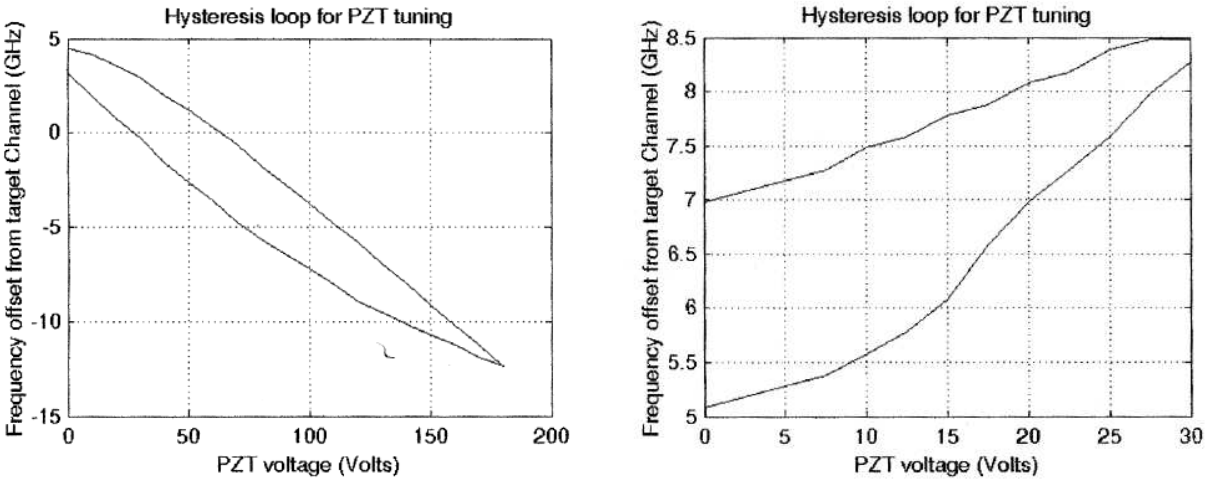

Figure B.2 Optical frequency offset versus PZT voltage for the Orbits Lightwave fiber lasers. Hysteresis effects are considerable when scanning over large voltage ranges.

Photodetectors

Two photodetectors from New Focus were used at various times in this experiment. They are model 1811 125 MHz photodetector and the model 1611 1 GHz photodetector. The

different detectors are generally referred to by their speed, as this indicates their response bandwidth. Their specifications are listed in the following table.

Table B.1 Technical specifications for the 1611 and 1811 high speed photodetectors from New Focus.

Specification	Units	Model 1811 (125 MHz)	Model 1611 (1 GHz)
Responsivity at 1500 nm	A/W	1.05	1.05
DC transimpedance gain	V/A	4×10^4	1×10^4
AC transimpedance gain	V/A	4×10^4	700
Noise equivalent power	$\mathrm{pW}/\sqrt{\mathrm{Hz}}$	2.5	20
3 dB response	MHz	125	1000

Appendix C - Fiber vacuum chamber design

Vacuum chambers were designed to allow the insertion of a fiber end and are shown from several perspectives in Figure C.1. Target pressures for the experiments in this work range from ~1 mtorr to several torr. This pressure level can readily be achieved using rubber gaskets, though 2.75" conflate flanges (which use an aluminum gasket and allow for lower pressures to be realized) were used when possible. All of the components used for this setup were either obtained from Kurt J. Lesker Corporation, Swagelok, or A&N Corporation. These chambers were machined (when necessary) and welded by Mike Wells (who is a vital part of the James R. MacDonald Laboratory staff). Optical access was necessary to couple light into the core of the fiber, so anti-refection coated wedged windows were obtained from CVI Melles Griot. A detailed view of the fiber holder is included in Figure C.2.

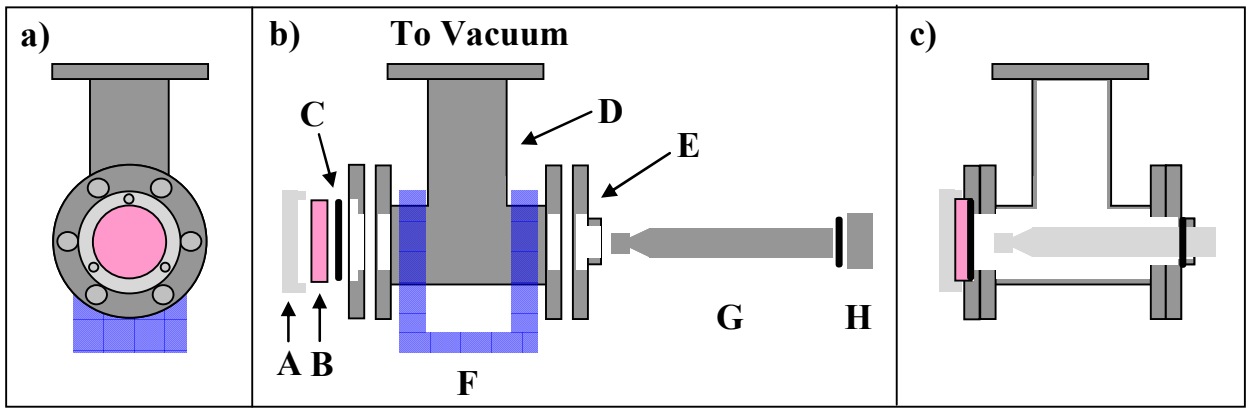

Figure C.1 Fiber vacuum chamber and holder using 2.75" conflate flanges. a) View of chamber along radial axis. b) Side view of disassembled chamber. White regions indicate holes in flanges for either optical access or fiber holder. A – Teflon window holder, B – IR coated wedged window, C – O-ring, D – vacuum chamber with 2.75" conflat flanges, E – 2.75" conflate flange with compression fitting threads, F – vacuum chamber stand, G – fiber holder (more detail shown in Fig), H – Compression fitting with O-ring. c) Side view of assembled chamber showing fiber holder in vacuum.

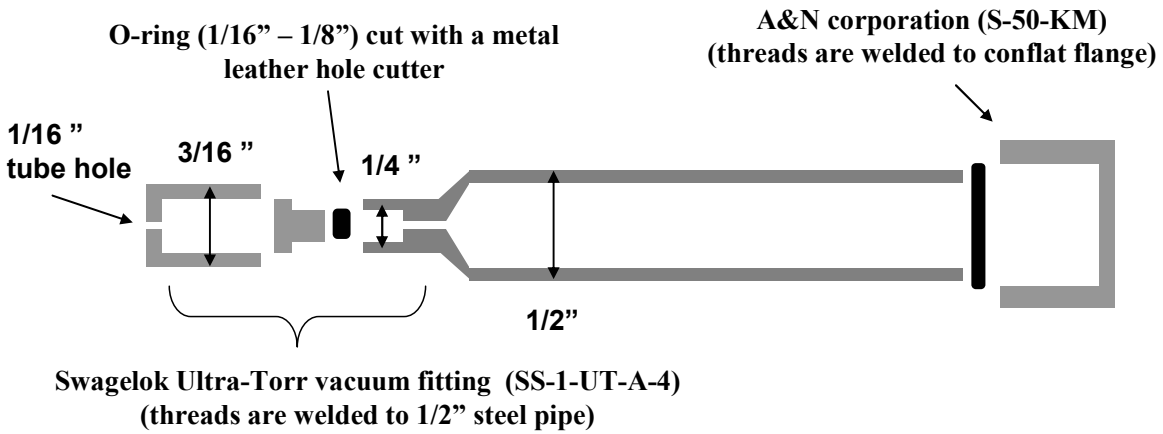

Figure C.2 Fiber holder schematic. Several key dimensions are listed along with the part numbers of the threaded components.